UNIVERSITY OF KWAZULU-NATAL™

INYUVESI YAKWAZULU-NATALI

MULTI-POINT STATIC DEXTEROUS POSTURE MANIPULATION FOR THE STIFFNESS IDENTIFICATION OF SERIAL KINEMATIC END-EFFECTORS

Submitted By:
Mr. Akshay Pradeep Singh (BScEng, UKZN) – 213535641

Supervisor:
Prof. Glen Bright

Co-Supervisor
Dr. Jared Padayachee

December 2020

Submitted in fulfilment of the academic requirements for the degree of Master of Science in Engineering at the School of Mechanical Engineering, University of KwaZulu-Natal

DECLARATIONS

DECLARATION 1 – SUBMISSION

As the candidate's Supervisor and Co-Supervisor, we agree with the submission of this dissertation.

[redacted]

07April 2021

Signed: ___________________________ Date: ___________________________

Professor Glen Bright

Signed: ___________________________ Date: ___________________________

Doctor Jared Padayachee

DECLARATION 2 – PLAGIARISM

I, Akshay Pradeep Singh, declare that:

1. The research reported in this dissertation, except otherwise indicated, is my original work
2. This dissertation has not been submitted for any other degree or examination at any other university.
3. This dissertation does not contain other persons‟ data, pictures, graphs or other information unless specifically acknowledged as being sourced from other persons.
4. This dissertation does not contain other persons‟ writing unless specifically acknowledged as being sourced from other researchers. Where other written sources have been quoted then:
    a. their words have been rewritten, but the general information attributed to them has been referenced;
    b. where their exact words have been used, their writing has been placed inside quotation marks and referenced.
5. Where I have reproduced a publication of which I am an author, co-author, or editor, I have indicated in detail which part of the publication was written by myself alone and have fully referenced such publications.
6. This dissertation does not contain text, graphics, or tables copied and pasted from the Internet unless specifically acknowledged, and the source being detailed in the dissertation and the References sections.

04 December 2020

Signed: [redacted] Date: ____________________

Declaration 3 – Publications

This section details the contribution to peer-reviewed publications that include the research presented in this dissertation. The undersigned agrees that the following submissions were published and submitted as described and that the content therein is contained in this research.

Publication 1 (Published): SAUPEC/RobMech/PRASA 2018

Singh, A.P. Bright, G. & Padayachee, J., "Joint Stiffness and Link Deflection Identification of Serial Robotic Manipulators and End effectors", SAUPEC/ROBMECH/PRASA 2019 Conference

Published October 2018, 6 Pages, 2018.

The paper was accepted in December 2018 in Central University of Technology, Free State, Bloemfontein, South Africa.

Main Author: Akshay Pradeep Singh

Co-Authors: Prof. G. Bright and Dr. J. Padayachee

Peer-Reviewed: 2

Publication 2 (Published): Africon

Singh, A.P. Padayachee, J. & Bright, G., "A Multi-Variable Approach: Identifying the Dexterous Zones and Stiffness of Serial Manipulators by Analysing the Function and Dexterous Workspaces", ISINCO 2019 Conference

Published August 2019, 7 Pages, 2019.

The paper was accepted in August 2019 in Accra, Ghana, IEEE AFRICON 2019

Main Author: Akshay Pradeep Singh

Co-Authors: Prof. G. Bright and Dr. J. Padayachee

Peer-Reviewed: 2

Publication 3 (Submitted): Elsevier

Singh, A.P. Bright, G. & Padayachee, J., "An Experimental Approach to Improving the Joint Stiffness of Industrial Robots Through Dexterous Posture Identification, Mechanisms and Machine Theory 2020 Journal

Submitted August 2020, 20 Pages, 2020.

Main Author: Akshay Pradeep Singh

Co-Authors: Prof. G. Bright and Dr. J. Padayachee

Peer-Reviewed: 2

Signed: [redacted] Date: 04 December 2020

ACKNOWLEDGEMENTS

I thank my beloved Shree Sathya Sai Baba for his guidance, wisdom, strength, and knowledge, and for granting me the opportunity to obtain my master's in Mechanical Engineering. I thank my late father, Pradeep Singh, for his strength, guidance, and everlasting love. I would not have made it this far if it was not for your blessings, sacrifices, and belief in me. A special thanks goes to my beloved mother and sisters for all their help, support, guidance, patience, and sacrifices that they made for me. A special thanks to my girlfriend, Naisha Ramlal, for all her support, help, guidance, and continuous motivation throughout my research. Thank you for your patience and understanding.

I would like to express appreciation to my supervisor, Professor Glen Bright, for all his support and guidance. I thank you for your wise counsel and professional guidance. I am immensely grateful for the assistance given by my co-supervisor, Doctor Jared Padayachee. Thank you for all your expert assistance, constant willingness to answer all my questions, as well as invaluable insights and advice. I am also thankful for your constant encouragement, for believing in me, and for always going the extra mile and supporting my decisions.

I thank the Mechanical Engineering workshop staff for all the assistance provided during my research.

I acknowledge my MR2G postgraduate colleagues and friends for their invaluable support, guidance, direction, and for motivating me during my research.

I would like to offer my special thanks to Energy and Combustion Services, especially my line managers, Doctor Mark Rawlins and Simmie Reddy. I thank you both for your guidance and for developing my skills throughout my research. I would also like to thank Energy and Combustion Services for the financial aid received.

ABSTRACT

The low stiffness inherent in serial robots hinders its application to perform advanced operations due to its reduced accuracy imparted through deformations within the links and joints. The high repeatability, extended workspace, and speed of serial manipulators make them appealing to perform precision operations as opposed to its alternative, the CNC machine. However, due to the serial arrangement of the linkages of the system, they lack the accuracy to meet present-day demands.

To address the low stiffness problem, this research provided a low-cost dexterous posture identification method. The study investigated the joint stiffness of a Fanuc M10-iA 6 Degree of Freedom (DOF) serial manipulator. The investigation involved a multivariable analysis that focused on the robot’s workspace, kinematic singularity, and dexterity to locate high stiffness areas and postures. The joint stiffness modelling applied the Virtual Joint Method (VJM), which replaced the complicated mechanical robot joints with one-dimensional (1-D) springs.

The effects of stress and deflection are linearly related; the highest stress in a robot’s structure is distributed to the higher load-bearing elements such as the robot joints, end-effector, and tool. Therefore, by locating optimal postures, the induced stresses can be better regulated throughout the robot’s structure, thereby reducing resonant vibrations of the system and improving process accuracy and repeatability. These aspects are quantifiably pitched in terms of the magnitude differences in the end-effector deflection.

The unique combination of the dexterity and the stiffness analyses aimed to provide roboticists and manufacturers with an easy and systematic solution to improve the stiffness, accuracy, and repeatability of their serial robots. A simple, user-friendly and cost-effective alternative to deflection measurements using accelerometers is provided, which offers an alternative to laser tracking devices that are commonly used for studies of this nature.

The first investigation focused on identifying the overall workspace of the Fanuc M-10iA robot. The reachable workspace was investigated to understand the functionality and potential of the Fanuc robot. Most robotic studies stem from analysing the workspace since the workspace is a governing factor of the manipulator and end-effector placement, and its operations, in a manufacturing setting.

The second investigation looked at identifying non-reachable areas and points surrounding the robot. This analysis, along with the workspace examination, provided a conclusive testing platform to test the dexterity and stiffness methodologies. Although the research focused on fixing the end-effector at a

point (static case), the testing platform was structured precisely to cater for all robotic manufacturing tasks that are subjected to high applied forces and vibrations. Such tasks include, but are not limited to, drilling, tapping, fastening, or welding, and some dynamic and hybrid manufacturing operations.

The third investigation was the application of a dexterous study that applied an Inverse Kinematic (IK) method to localise multiple robot configurations about a user-defined point in space. This process was necessary since the study is based on a multi-point dexterous posture identification technique to improve the stiffness of Serial Kinematic Machines (SKMs). The stiffness at various points and configurations were tested, which provided a series of stiff and non-stiff areas and postures within the robot's workspace.

MATLAB®, a technical computing software, was used to model the workspace and singularity of the robot. The dexterity and stiffness analyses were numerically evaluated using Wolfram Mathematica.

The multivariable analyses served to improve the accuracy of serial robots and promote their functionality towards high force application manufacturing tasks. Apart from the improved stiffness performance offered, the future benefit of the method could advance the longevity of the robot as well as minimise the regular robot maintenance that is often required due to excessive loading, stress, and strain on the robot motors, joints, and links.

"It always seems impossible until it's done"

~ Nelson Mandela ~

To my Father – Pradeep Singh

TABLE OF CONTENTS

LIST OF ACRONYMS AND ABBREVIATIONS

AI:	Artificial Intelligence
ANN:	Artificial Neural Network
ANSI/RIA:	American National Standards for Industrial Robots and Robot Systems
BNC:	Bayonet Neill-Counselman
CAD:	Computer-Aided Design
CAGR:	Compound Annual Growth Rate
CCT:	Conservative Congruency Transformation
cDAQ:	compactDAQ
CNC:	Computer Numerically Controlled
DAQ:	Data Acquisition
DC:	Direct Current
D-H:	Denevit-Hartenberg
DOF:	Degree of Freedom
FEA:	Finite Element Analysis
FIR:	Finite Impulse Response
GDP:	Gross Domestic Product
GUI:	Graphical User Interface
HTM:	Homogenous Transformation Matrix
ICP:	Integrated Circuit Piezoelectric
IEPE:	Integrated Electronics Piezo-Electric
IFR:	International Foundation of Robotics
IK:	Inverse Kinematic
ISO:	International Organisation for Standardisation

MC:	Manufacturing Circle
MEMS:	Micro-Electro-Mechanical Systems
MSA:	Matrix Structural Analysis
NI:	National Instruments
1-D:	One-Dimensional
PCB:	Printed Circuit Board
PKM:	Parallel Kinematic Machine
SKM:	Serial Kinematic Machine
SLJ:	Second-to-Last-Joint
6-D:	Six-Dimensional
3-D:	Three-Dimensional
2-D:	Two-Dimensional
USD:	United States Dollar
VI:	Virtual Instrumentation
VJM:	Virtual Joint Method

NOMENCLATURE

$\boldsymbol{A}$	Forces in joint space based on the forces applied in end-effector space
$\boldsymbol{A_c}$	Cross-sectional area
$\boldsymbol{B}$	A Matrices
$\boldsymbol{c}$	δt Matrices
$\mathbf{C_{ij}}$	Matrix of cofactors (adjugated matrix)
$\boldsymbol{dq}$	Vector of end effector velocities
$\boldsymbol{dx}$	Vector of end effector velocities
$\boldsymbol{E}$	Modulus of elasticity
$\boldsymbol{E_{material}}$	Modulus of elasticity of the material
$\boldsymbol{F_x}$	Vector of external loading applied to end effector in the x-direction
$\boldsymbol{F_y}$	Vector of external loading applied to end effector in the y-direction
$\boldsymbol{F_z}$	Vector of external loading applied to end effector in the z-direction
$\boldsymbol{g}$	Acceleration due to gravity
$\boldsymbol{h_{SLJ}}$	Height of second-to-last-joint
$\boldsymbol{I}$	Moment of inertia
$\boldsymbol{J}(\boldsymbol{q})$	Jacobian matrix
$\boldsymbol{J}(\boldsymbol{\theta})$	Jacobian
$\mathbf{J_A}$	Subset matrix A of the Jacobian matrix
$\mathbf{J_B}$	Subset matrix B of the Jacobian matrix
$\mathbf{J_v}$	The Jacobian linear velocity component
$\boldsymbol{J_\omega}$	The Jacobian angular velocity component
$\mathbf{J}^{\boldsymbol{T}}$	Transpose Jacobian matrix

$\mathbf{J}^{-T}$	Inverse transpose Jacobian matrix
$\lvert\mathbf{J}(\mathbf{q})\rvert$	Determinant of Jacobian matrix
$\lvert\mathbf{J}(\mathbf{q})\rvert^{-1}$	Inverse Determinant of Jacobian matrix
$\lvert\mathbf{J_A}\rvert$	The determinant of subset Jacobian matrix A
$\lvert\mathbf{J_B}\rvert$	The determinant of subset Jacobian matrix B
$\boldsymbol{K_\theta}$	Joint stiffness matrix
$\boldsymbol{K_X}$	Complementary stiffness matrix
L	Length of beam
$\boldsymbol{l_3}$	Robot link 3
$\boldsymbol{l_4}$	Robot link 4
$\boldsymbol{l_5}$	Robot link 5
$\boldsymbol{L_{wrist}}$	Length of the wrist configuration
$\boldsymbol{m_{motor}}$	Weight of the motor
$\boldsymbol{M_x}$	Vector of external moments applied to end-effector in the x-direction
$\boldsymbol{M_y}$	Vector of external moments applied to end-effector in the y-direction
$\boldsymbol{M_z}$	Vector of external moments applied to end-effector in the z-direction
$\boldsymbol{n}$	Number
$\mathbf{p_n}$	End effector translational position
$\mathbf{p_n}'$	Deflected end-effector translational position
$\boldsymbol{p_x}$	End-effector x-coordinate
$\boldsymbol{p_y}$	End-effector y-coordinate
$\boldsymbol{p_z}$	End-effector z-coordinate

$\dot{\mathbf{P}}_{\mathbf{i}}^{\mathbf{i-1}}$	Joint velocity vector for translational (prismatic) joints
$\dot{\boldsymbol{q}}$	Joint velocity vector
$\dot{\mathbf{q}}_{\mathbf{i}}^{\mathbf{i-1}}$	i^{th} Joint velocity vector
$\boldsymbol{r_{ij}}$	Rotation matrix
$\boldsymbol{R_n}$	End-effector rotational position
$\boldsymbol{R_n}'$	Deflected end-effector rotational position
$\boldsymbol{t}$	Dimension of task space
$^{0}\boldsymbol{T_6}$	Homogenous Transformation matrix
$^{0}\boldsymbol{T_6}'$	Deflected Homogenous Transformation matrix
$\mathbf{V}$	Velocity vector
$\boldsymbol{W}$	Weight of the payload
$\boldsymbol{w}$	Measure of manipulability
$\boldsymbol{w_{link}}$	Weight of the links
$\boldsymbol{x_2}$	x-coordinate of second robot joint
$\boldsymbol{y_2}$	y-coordinate of second robot joint
$\boldsymbol{z_2}$	z-coordinate of second robot joint
$\mathbf{0}$	Zeros matrix
$\mathbf{0}_{\boldsymbol{n}}^{\boldsymbol{T}}$	Transpose zero matrix

Greek Alphabet

$\boldsymbol{\alpha}$	Alpha angles
$\boldsymbol{\alpha'}$	Nominal alpha angles
$\boldsymbol{\alpha_{max/min}}$	Maximum/Minimum alpha angles
$\boldsymbol{\beta}$	Beta angles
$\boldsymbol{\beta'}$	Nominal beta angles
$\boldsymbol{\beta_{max/min}}$	Maximum/Minimum beta angles
$\Delta \boldsymbol{Y}_{(L_2, L_3)}$	End-effector deflection due to bending of link one and link two
$\Delta \boldsymbol{Y_{twist}}$	End-effector twist
$\boldsymbol{\delta_{Total}}$	Total deflection
$\boldsymbol{\delta}$	Angle formed between link five and the nominal distance ρ
$\boldsymbol{\delta\theta}$	Deflection in the virtual joint coordinate θ caused by loading
$\boldsymbol{\delta p}$	Translational displacement of end-effector
$\boldsymbol{\delta R}$	Rotational displacement of end-effector
$\boldsymbol{\delta t}$	End-effector displacement in Cartesian space (both positional and orientational)
$\boldsymbol{\theta}$	Angle of twist
$\dot{\boldsymbol{\theta}}_{\mathbf{i}}^{\mathbf{i-1}}$	Joint velocity vector for rotational (revolute) joints
$\boldsymbol{\rho_{material}}$	Density of material
$\boldsymbol{\rho}$	Distance between end-effector and second robot joint
$\boldsymbol{\sigma}$	Angle formed between the nominal position line ρ and link three and 4
$\boldsymbol{\tau}$	Vector of reactions in the elastic joints
$\boldsymbol{\tau_\theta}$	Linear Elasticity using Hooke’s Law
$\boldsymbol{\omega}$	Wrench force
$\boldsymbol{\gamma}$	Gamma angles

LIST OF FIGURES

LIST OF TABLES

1. INTRODUCTION

1.1 ROBOTIC AND MANUFACTURING CHALLENGES

During the past decade, industrial robots in modern production and machining have surprised the industrial world. Traditionally, Serial Kinematic Machines (SKMs) were involved in basic manufacturing operations that did not require continuous, direct contact with the workpiece. These routine operations involved general pick-and-place, material part handling, and spray painting. Modern-day requirements contend for higher flexibility in terms of configuration possibilities, larger workspaces, and speed.

The SKM features a firm architecture containing graded steel arms and joints, and multiple Degrees of Freedom (DOF). A disadvantage is the compromised structural-mechanical stiffness of the arms due to the system's interlinkage profile and weight. The error propagation through each joint generates uncontrollable end-effector forces, limiting its application for complex manufacturing operations in the industry.

Stiffness referenced to kinematic machines is the accuracy required to satisfy the anticipated force and position commands [1, 2]. According to Carbone [3] and Bu, Liao, Tian and Zhang [4], mechanical stiffness has been the most critical performance indicator of robotic systems. The architectural design of the SKM is ruled by its ability to manipulate its tool precisely, and in doing so, it requires high stiffness to limit positioning errors due to external loadings on the end-effector during complex workpiece processing [5].

According to Olofsson [6], the International Federation of Robotics (IFR) recently declared that industrial robots performing precision operations worldwide account for less than one percent of the total operational robots in manufacturing facilities. These applications included welding, milling, and grinding, which demanded direct and continuous contact with the workpiece [7]. Although manufacturing accounted for most industrial robots, especially the automotive and electronics industries, SKMs were also applied in the medical and pharmaceutical departments [8]. A noteworthy study by McKinsey and Company [9] sought industries that are investing in low-cost production while maintaining production flexibility and improved capabilities of robots. Their analysis of market predictions showed that automotive industries contribute the highest investments in automation and robotics. This finding is of particular significance to the current study. The results of their analysis are graphically illustrated in Figure 1-1 below.

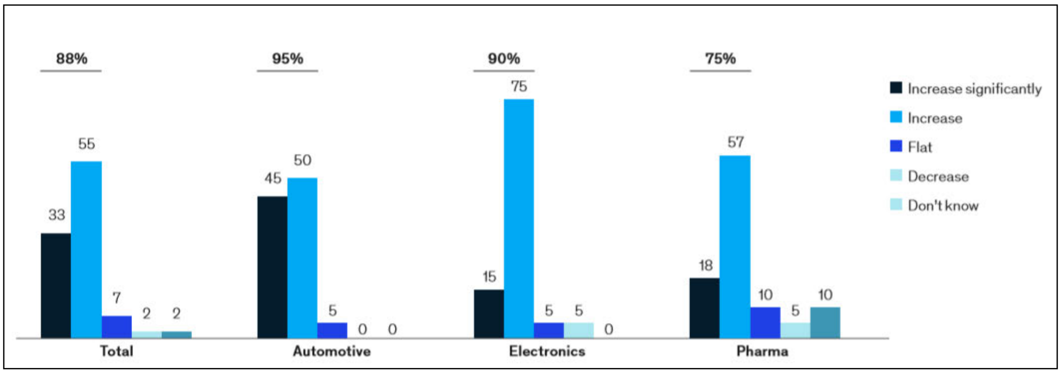

Figure 1-1: Investment Outlook for Automation and Robotics Industries [9]

Furthermore, the above-mentioned study also confirmed the rapid investments being made to reduce production costs and improve quality in line with the IFRs council to advance automation and robotics. Figure 1-2 presents some of the key drivers that respondents are investing in to improve the adoption of automation and robotics. Based on these findings, this research contributes to the cost and quality demands by presenting a low-cost experimental procedure to identify the stiffness of SKMs through a dexterous posture identification method. This saves small manufacturing firms that do not possess high-end, expensive displacement measurement systems and sensors. The quality aspect is proven by identifying (dexterous) postures, testing the stiffness using the VJM, and identifying joint coordinate ranges that comprise stiff posture for precision manufacturing tasks.

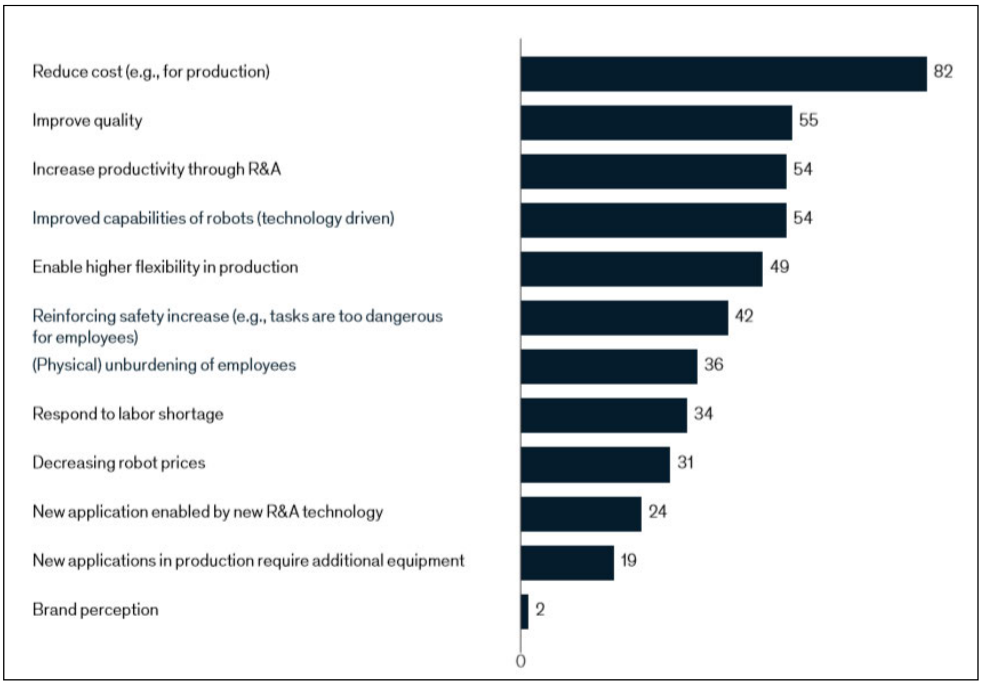

Figure 1-2: Main Drivers Prompting Investments in Automation and Robotics Solutions [9]

Computer Numerically Controlled (CNC) machines and Parallel Kinematic Machines (PKM) have and are meeting the accuracy and precision demands of contemporary manufacturing. In a manufacturing sense, precision is the ability of a tooling machine to repeatedly return to its original position. The CNC was designed and built for precisely this purpose. However, both machines have drawbacks: 1) they are unable to handle complex geometrical components due to restricted workspace, and 2) they lack the flexibility to reach difficult machining areas.

The continuous demands on flexibility and high efficiency in global production markets created a desire to acquire automated and flexible tasks. The solution to the problem is SKMs. Although few, their drawbacks include: 1) limited stiffness, 2) positional accuracy, and 3) inability to perform specific tasks based on Computer-Aided Design (CAD) specifications with an acceptable result [6].

This dissertation explored a solution to combat the low apparent stiffness encumbering SKMs. The Virtual Joint Method (VJM) stiffness approach implements an Inverse Kinematic (IK) dexterous posture identification technique. The unique combination of methods provides a logical, feasible and practical approach to locate and improve the stiffness of SKMs during operations that involve high end-effector forces and vibrations. A low-cost alternative using accelerometers to measure the deflection and twist of the robot end-effector is addressed.

1.2 Motivation for Research

This section provides the motivations for conducting this research. First, emerging technologies and modern manufacturing demands have shifted the robotic machining paradigm from general pick-and-place operations to complex manufacturing processes such as material removal, intricate cutting, drilling, tapping, and others [10]. These intrinsic functionalities are possible with a single interlinked mechanical system which has been thoroughly explored by many scholars [11-14] in terms of their kinematic formulations and manufacturing capabilities. In contrast, CNC machines can only handle individual tasks that require several complicated and expensive tooling fixtures for different operations [15]. This is where this research fits in, to expand the use of SKMs in industry and supply machinists and roboticists with an approach to locate and identify optimal robot configurations for operations involving high end-effector forces and vibrations.

Second, another motivation for this study is the increased demand for industrial robots. This is evident in the 2009 – 2017 robot global sales figures, which increased from 60,000 to 381,000 annually at a 26% Compound Annual Growth Rate (CAGR) [16, 17], with the largest consumer being China [18, 19]. Future predictions have estimated the robotic market to be worth USD 82.5 billion by 2025 [20, 21], further affirming this study's need.

Third, closely related to the above, as the demand for robots increases, so does the need for advancement and development of robots in the industry. Manufacturing requirements contend for ease-of-use modelling approaches that do not require complex programming of the robot control system. Roboticists and manufacturers require quick and easy solutions to improve the efficiency of their robot operations, systems, and processes. Manufacturing objectives such as reducing costs, improving quality, increasing production flexibility, and throughput ensure that manufacturers consistently meet their customers' price, quality, and delivery requirements. This study specifically addressed this identified gap. Robot manufacturers are continually advancing their robots to keep up with manufacturing demands and improve their robot's intelligence (both software and artificially) to ensure precise motion control. To meet the current quality demands and increased global use, it is necessary to minimise, if not eliminate, robotic errors. This highlights the need for the improvement of robots and ongoing advancement in the industry.

Fourth, is the drive to reduce robotic errors and improve efficiency. Robotic errors are inherent in most applications due to the lack of stiffness constraining the links and joints. Mitigating these errors are complicated and can, most of the time, be resolved using software interventions. It is uncommon for robot users to alter the robot's mechanical components; this is usually infeasible and can ultimately lead to permanent damage. As a result, the variable factor governing robotic stiffness is posture identification. According to Xaud [22], Celikag *et al*. [23], and Mousavi *et al*. [24], the dynamic and static properties of SKMs are configuration dependent. The motivation to apply posture control unravelled a multivariable approach imperative for the robot stiffness analysis applied in this research. These variables are *robotic workspace, kinematic singularity*, and *dexterity*. They are discussed in greater detail in Chapter 2.

Fifth, is to provide a cost-effective alternative to the expensive sensory devices. The type of sensor attributes the trade-off between the unit price and production loss. Sensors have the potential to realise the profit and loss associated with every unit sold [25]. Manufacturing facilities, both big and small, are seeking compact, user-friendly, cheap, reliable, and robust sensors. The existing literature around robotic stiffness modelling incorporated expensive laser tracking and other high-end displacement sensors to measure the end-effector deflection. The research performed in this study supports manufacturers that are financially constrained by using a cost-effective sensor alternative, that is, Integrated Electronics Piezo-Electric (IEPE) accelerometers, to measure robotic displacement.

Sixth, and lastly, there is a declining focus around improving previously designed SKMs for complex manufacturing operations. Roboticists and manufacturers are not willing to replace their existing manufacturing processes, robots, and machines, but are rather seeking a universal method that can improve their customers' precision demands. For this reason, this study serves to provide a simple methodology for manufacturers to follow, with existing robotic arms while further contributing to the broader knowledge of SKMs and precision manufacturing. These motivations, in turn, informed the objectives of this study provided further below.

1.3 Scientific Contribution and Target Audience

The research study made the following contributions:

1. A multivariable analysis that focused on robotic workspace, kinematic singularities, and dexterity to improve robotic stiffness.
2. A unique combination of a dexterous IK approach with the VJM stiffness modelling approach.
3. The implementation of accelerometers as a low-cost displacement sensor.
4. A systematic and easy-to-follow robotic stiffness identification approach using the VJM.

Automation and robotics have gained traction in almost every conceivable industry. According to some manufacturers [26], robots are utilitarian, "built for purpose", and are high-performance machines show-casing advanced technology and demonstrating major performance breakthroughs. The automotive industry, such as Ferrari, Lamborghini, and other luxury car manufacturers, as well as major aerospace manufacturers, such as Boeing, and Lockheed Martin, are applying serial robots to perform common manufacturing operations, like drilling, fastening, inspection, and welding [26-28]. Serial robots are very appealing to these industry sectors. This study, therefore, provides an alternative approach to locate and identify stiff configurations to limit the strain placed on the joints of SKMs during high-force applications. This speaks to the aim of this study, which is provided next.

1.4 Aim, Objectives and Research Question

Aim:

This study aimed to evaluate and design a multi-point static dexterous posture identification technique that can locate and improve the stiffness of Serial Kinematic Machines and promote their functionality towards precision manufacturing tasks that involve high contact forces and vibrations.

Objectives:

The objectives of this study were to:

1) Research, establish and develop a dexterous posture identification method that can localise multiple configurations at a user-defined point.
2) Research, develop and simulate the workspace and singularities of the Fanuc M10-iA and understand their influence on the dexterity and stiffness analyses.
3) Research, establish and identify a suitable stiffness modelling approach.

4) Develop a systematic approach to the stiffness identification algorithm such that any roboticist can universally adopt it.
5) Research, identify and implement a cost-effective, reliable and robust displacement sensor.
6) Research, design, construct and implement a suitable testing ground to test the workspace, singularity, dexterity, and stiffness model.
7) Research, plan and execute a series of tests and methods of data collection and analysis to validate the effects of the dexterous posture identification technique on the stiffness modelling of the Fanuc M10-iA.

Research Question:

The research question formulated for this study was:

> "Can a multivariable approach involving a workspace, singularity and multi-point static dexterous posture identification solution locate and improve the mechanical stiffness of Serial Kinematic Machines?"

1.5 METHODOLOGICAL APPROACH

To achieve the study's aim and objectives, and answer the formulated research question, this study employed a literature review. For this review, recent studies published in books, journal articles, reports, and book chapters on the research topic were consulted to:

1) Extract pertinent information relating to optimal static point posture identification techniques.
2) Research and formulate workspace identification methods – analyse the maximum and minimum reachability of the manipulator.
3) Research and identify the singularity detection methods – analyse areas/zones/postures that are not reachable by the end-effector.
4) Research, develop, and formulate a clear relationship between dexterity and its impact on stiffness identification.
5) Research, review, and develop a list of various stiffness modelling techniques and select the optimal solution to model SKMs.
6) Research, design, and construct a suitable testing ground for stiffness identification.
7) Analyse deflection and stiffness data in a suitable software, and graphically represent the data.
8) Check and verify the reliability and repeatability of measured deflection and stiffness results.
9) Interpret and present an application of the current research and measured deflection and stiffness results in the industry.

10) Present the research findings in the form of an MSc. dissertation, conference papers, journal articles, and possibly even a book chapter in an edited volume.

1.6 DISSERTATION ROADMAP

Chapter 1: Introduces the study and provides a general background of the problem being researched. In addition to highlighting common manufacturing challenges, the chapter also explains the motivation for conducting the research, indicates the target audience, and states the methodology employed and the research question, aim, objectives, and scientific contribution of the study. This is followed by an outline of the chapters and a brief summary.

Chapter 2: Critically reviews the existing literature that focuses on the effects of the Fourth Industrial Revolution. Also reviewed are emerging trends in the CNC and robotic markets, and global and local efforts to shift the robotic paradigm. The chapter explores manufacturing and challenges asphyxiating robotic machining, while also discussing the potential of Parallel Kinematic Machines (PKMs). Furthermore, the literature review also focuses on robotic workspace, kinematic singularity, dexterity, and stiffness, followed by stiffness modelling approaches and related work on the VJM technique. This chapter addresses Objectives 1, 2 and 3.

Chapter 3: Presents the conceptual framework by considering the need to perform the research by analysing the three variables – *robotic workspace, kinematic singularity*, and *dexterity* – used to enhance serial robotic stiffness. This chapter partially addresses Objectives 1, 2 and 3.

Chapter 4: Provides the first analysis – identifying the *workspace* of the Fanuc M-10iA robot. The chapter provides the analytical formulation and simulation results. This chapter addresses Objective 2, and partially addresses Objective 4.

Chapter 5: Deals with the second analysis – the *kinematical singularities* of the Fanuc M-10iA robot. The chapter begins with an analytical formulation and simulation results. This chapter partially addresses Objective 2 and 6.

Chapter 6: Describes the third analysis – detecting the *dexterous workspace*. Herein, the mathematical formulation of the IK solution is discussed. This chapter addresses Objective 1.

Chapter 7: Focuses on the objective of the study – *stiffness modelling* and *identification*. This chapter comprises the VJM modelling formulation, identification, and mathematical approach. This chapter partially addresses Objective 3 and fully addresses Objective 4.

Chapter 8: Explains the experimental procedure and physical testing results. This chapter addresses Objectives 1, 2, 3, 4, 5, 6 and 7.

Chapter 9: Summarises the experimental procedure and results.

Chapter 10: Provides a summation of the main findings discussed in terms of the research objectives and indicates the limitations and contributions of the study. It also provides recommendations for improving robotic stiffness in manufacturing and future research, and a brief conclusion wrapping up the study.

1.7 Chapter Summary

This chapter set out to explore the various challenges experienced with machining in manufacturing and explained the importance and necessity of this study. It also described the key elements of the research process – motivation, background, research question, aim, objectives, methodology, and contribution of the study – and outlined the forthcoming chapters.

The next chapter presents the literature review of the study.

2. LITERATURE REVIEW

2.1 INTRODUCTION

This chapter presents the literature review of this study. The first section focuses on robotic and manufacturing in Industry 4.0 (section 2.2), followed by a reflection on current trends in the CNC and robotic markets (section 2.3). The potential of Parallel Kinematic Machines (section 2.4) and robotic challenges (section 2.5) are outlined next. Attention then shifts to the variables analysed in this research, namely, robotic workspace (section 2.6); kinematic singularity (section 2.7); dexterity (section 2.8); and robotic stiffness (section 2.9). The chapter then relates each of the analyses together (section 2.10), indicating their contribution towards robotic stiffness modelling. This is followed by some concluding remarks to close the chapter (section 2.11).

2.2 ROBOTIC AND MANUFACTURING IN INDUSTRY 4.0

Industrial manipulators form a crucial part of the modern manufacturing era. The number of flexible industrial robots that have been established by chief players through incorporating Industry 4.0 technologies in Europe alone has doubled since 2004 [29]. The forefront of Industry 4.0, also referred to as "The Fourth Industrial Revolution", lies with autonomous manufacturing methods that are power-driven by robots as they manage various tasks intelligently while focusing on flexibility, safety, collaboration, and versatility. Robots are evolving without having to work in isolation. HRI has increased and allowed for higher productivity and increased economic contribution since it has realised more industry applications. Major robot developers are revolutionising their robotic designs to incorporate the latest technological innovations to accelerate the industrial revolution.

The new and rising trend in the industrial value creation chain has an innovative manufacturing solution, as depicted in Figure 2-1. In the field of state-of-the-art technologies, the use of high efficiency, productivity, accuracy, and transparency have become the central focus of attention [30]. Germany, the power-driver behind Industry 4.0, has developed data-driven supply chains that speed up their manufacturing processes by an estimated 120% in terms of delivering orders and by 70% to shift products to the market [31]. Through integrated product development with digital and physical production, there has been an improvement in product quality. Feedback from sensors monitored and tracked each part produced, rather than sampling methods to detect the error. These error-correcting machines adjusted production processes in real-time. The feedback was collected and scrutinised using "big data" methods to identify and correct continuing problems.

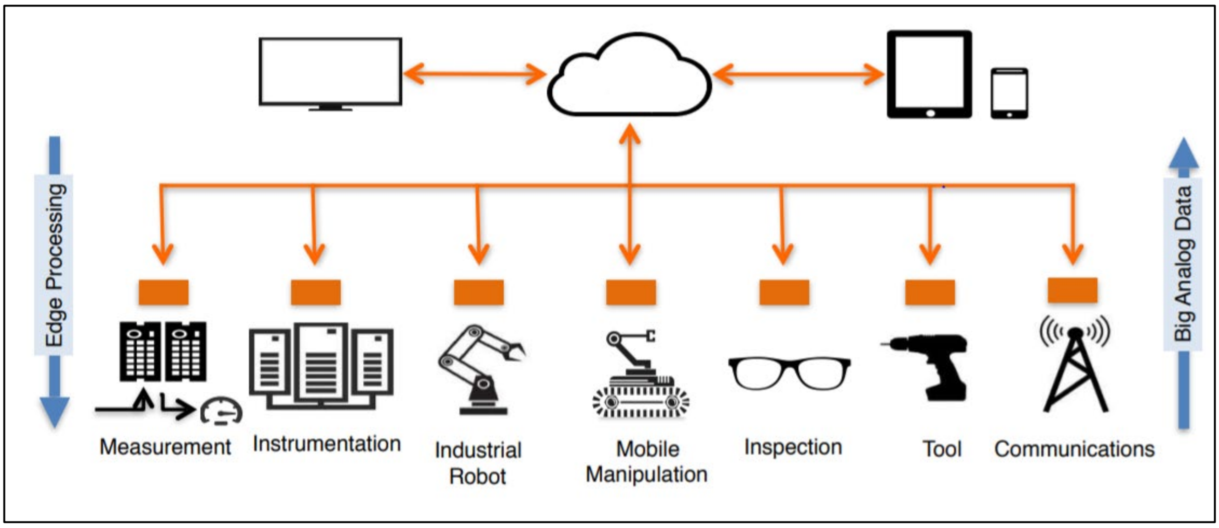

Figure 2-1: Industry 4.0 – On the Manufacturing Floor [32]

The constant demand for quality was pivotal in reducing costs and increasing competitiveness [33]. The present research dealt with a low-cost approach to measuring the deflection of a robot end-effector and identify areas within the reachable workspace that possess higher stiffness and stiff postures. In this light, the current contribution can improve operations that involve high end-effector forces and vibrations and promote SKMs into an industry 4.0 applicable robotic system.

2.3 CNC, Robotic and Manufacturing Trends

Relevant to the topic under discussion, this section reflects on global trends in the CNC and robotic markets (sub-section 2.3.1) as well as manufacturing trends in South Africa (sub-section 2.3.2).

2.3.1 Global Trends in the CNC and Robotic Market

The global CNC machine tools market was predicted to grow at a CAGR of 9% between 2017 and 2021 [34]. CNC machine applications target the aerospace, automotive, metal fabrication, shipbuilding, and electronics sectors. The erupting popularity and commercialisation of advanced CNC machines have prompted manufacturers to realise new milling tools that are more versatile and efficient.

The 5-axis CNC machine is world-renowned and has impacted metal processing industries by improving efficiency, minimising cycle time, and reducing material wastage. The growing demand in the automotive, aerospace, electronics, and metal fabrication industries have encouraged manufacturers to apply innovative and technological incorporations. The dawn of the novel 6-axis CNC machines has redefined machining technologies and operations. The machines' capability to turn both ends of the fixtures and process the raw material into finished goods without adding multiple fixtures and other machining activities has increased their manufacturing popularity [34].

Manufacturers are trying to adopt an interconnected system that streamlines CNC machines with other machines and procedures. It is common in the industry for CNC machines and manufacturing robots to work closely in the production line due to the former's high strength in processing raw materials and the latter's ability to move and pack the produced goods in an orderly, repeatable fashion. There has been much effort and collaboration between machine buildings, CNC developers, and robot manufacturers to develop a unique and simple programming language that can be integrated seamlessly between CNC machines and robots. This quality improvement aspect of this research can help SKMs complete intricate machining at hard-to-reach areas that would otherwise be difficult for a CNC machine to reach.

Some collaborators have invested in this idea, such as Siemens and KUKA, who have developed a novel interface that allows CNC operators to control both CNC machines and robots simultaneously from a single control panel [35]. Rather than replacing CNC machines, SKMs can assist for part handling and pre-processing of the part, and reduce the manual labour involved in the operation of general-based CNCs [36]. Figure 2-2a graphically shows a 5-axis CNC machining centre, which can be used to machine multiple and complicated workpieces in single setups [37]. Figure 2-2b shows the novel 6-axis CNC machine, which offers superior flexibility and capability as opposed to the 5-axis CNC [38]. Finally, Figure 2-2c displays a 6-axis CNC robot, based on a non-cutting CNC machine [39].

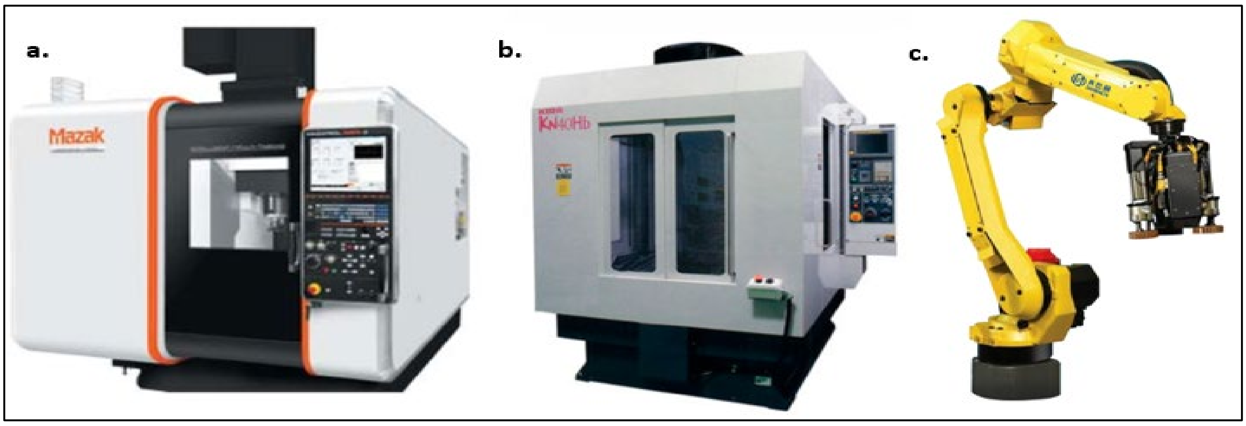

Figure 2-2: a) 5-Axis-Machining Centre, b) 6-Axis CNC Milling Machine, and c) CNC Robotic Arm [39]

On the contrary, according to Kumar from Grand View Research Incorporations [40], by the year 2020, the global industrial robotics market is expected to surpass USD 40 billion. The growing demand from automotive industries, coupled with the increasing labour costs, has stimulated industrial robots' deployment in manufacturing. The increased importance of product quality to guarantee survival in the competitive manufacturing world was the primary driving force in the robotics market. Thus, localising optimal points, areas, and postures can improve the stiffness of SKMs by evenly distributing the stress on the joints of the robot, ensuring that there is an improvement in the quality and precision requirements for contemporary manufacturing. This research will provide roboticists with optimal areas and postures that possess high joint stiffnesses that relate to the Fanuc M10-iA robot and possibly to other robots of similar architecture and design.

2.3.2 Manufacturing Trends in South Africa

According to South Africa's Gross Domestic Product (GDP), the manufacturing sector's contribution has been at a steady decline over the past few decades [41]. Industry lobby organisation's such as the Manufacturing Circle (MC) envisaged that the situation would continue to decline unless affirmative action was made to improve the sector's competitiveness. Additionally, a leading financial institute report stated that the economy would deindustrialise within the following decade if there were no improvement in growth and if the high unemployment rates continued [41].

Furthermore, the persistent increase in import competition and unpredictability of the rand exchange rate is exacerbating the effects placed on South African manufacturing industries [42]. Illustrated in Figure 2-3, in 2018, the manufacturing industry was the fourth largest contributor to South Africa's GDP, while almost 36 years ago, it was approximately 20% of the national GDP [43, 44].

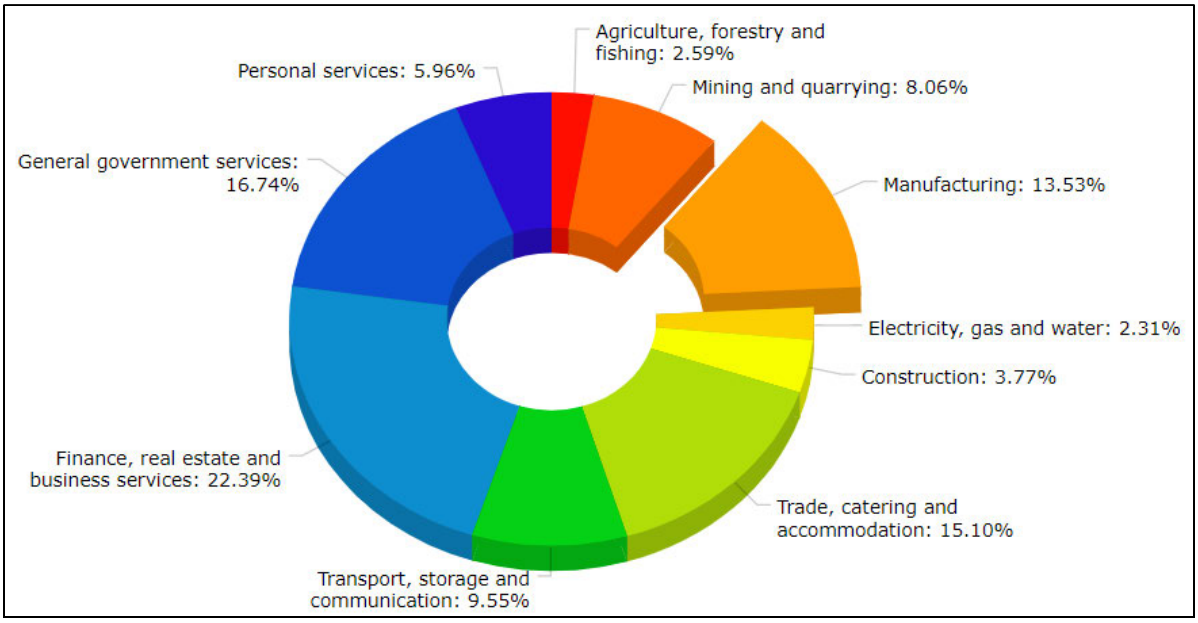

Figure 2-3: Relative Contribution of Industries to South Africa's 2019 GDP [43]

To elucidate the discussion further, South Africa's automotive sector has been one of the most significant annual contributors to the national GDP, contributing nearly 7% [45]. In light of this trend, the government needs to improve innovative processes to sustain the automotive and large industries to strengthen the country's declining competitiveness [10].

In that, despite South Africa's diverse manufacturing sector, the production scale is nevertheless declining [41]. Presently, the majority of manufacturers in South Africa rely on supply chains from Asia [46]. According to Rodrik [47], between the years 1980 and 2004, South Africa's manufacturing segment's profitability reduced by 30%. It can be expostulated that the moderately lower profit margins within the local manufacturing sector are the reason behind the struggle in attracting foreign direct investment. Rodrik [47] contends that the manufacturing sector's inability to generate jobs was the primary reason for South Africa's insufficient growth and high unemployment rate. In short, Rodrik ascribed the high unemployment rate was due to the declining price of manufacturing goods.

In this context, the application of this research can assist roboticists by providing an easy, systematic, and cost-effective approach to improve high-force applications with SKMs. In this regard, this addresses Objective 4 of this study which seeks to *develop a systematic approach to the stiffness identification algorithm such that any roboticist can universally adopt it.*

As previously stated, SKMs provide the required workspace, speed, and flexibility for manufacturing, and assembly lines and innovative solutions can lead to cost-effective robotic solutions to address the needs of the South African manufacturing markets. South Africa could realise much economic potential by focusing on improving the use of SKMs in the manufacturing sector and increase mass production, to improve the country's economic state and competitive advantage [48].

Having discussed the CNC, robotic, and manufacturing trends in South Africa in the section above, attention now shifts to the potential of parallel kinematic machines below.

2.4 The Potential of Parallel Kinematic Machines

To meet high stiffness and accuracy requirements, robot manufacturers have designed conventional machine tools with immense structures. This imposed limitations on the machine's dynamic characteristics and flexibility. In recent years, the development of the PKM has spawned the market to overcome these limitations. PKMs are generally composed of light moving masses that are rigidly connected with high stiffness to weight ratios [49]. Apart from the PKMs reduced workspace volume compared to conventional machine tools such as SKMs, they provide superior accuracy and high-speed machining ability [50, 51]. According to Dharmalingum [52], various PKM configurations exist in the literature, from fixed-length legs that offer lesser DOF, and are more suited to machine tool applications due to their high stiffness and telescopic legs that are less stiff with smaller workspaces. For example, the 3-PRRR parallel manipulator was equipped with only prismatic and revolute joints to attain purely translational motion on a moving platform [53]. Similarly, the Orthoglide – a 3-DOF translational parallel manipulator – was implemented for machine tool tasks [54].

Modern advancements in machining included the hybrid 5-axis milling machines that were based on PKM and SKM designs. This review, however, revealed a paucity of research on the use of PKMs for metal-cutting operations [55, 56]. Furthermore, according to Terrier, Dugas, and Hascoet [57], the stiffness and dynamic characteristics of PKMs differed from conventional machine tools based on SKMs. Consequently, machining parameters such as feed rate, cutting speed, and depth of cut were proposed for conventional milling machines, and may not apply to PKM-based machine tools. Therefore, to establish the suitability of parallel kinematics for industrial tasks, further research is required in this area, particularly regarding their performance for several cutting parameters and optimisation. Figure 2-4a, and Figure 2-4b presents the difference in mechanical structures and design between SKMs and PKMs, respectively.

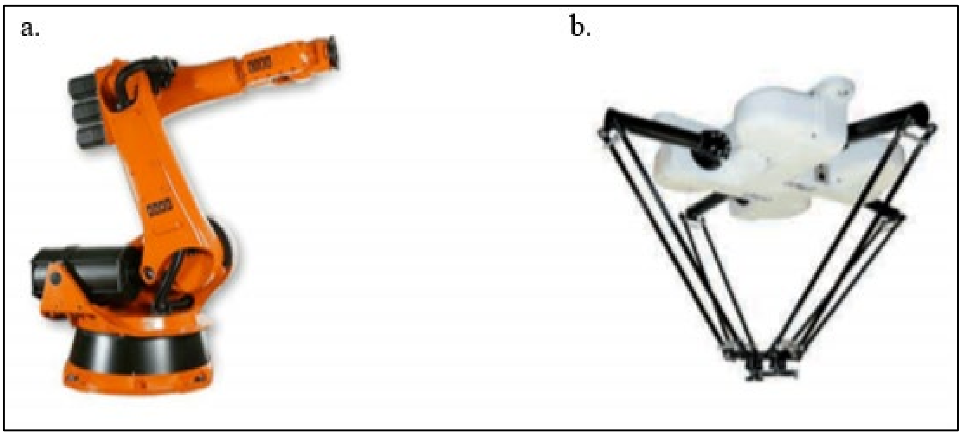

Figure 2-4: a) A Serial Industrial Kuku Robot and b) Adept Parallel Industrial Robot [58]

A performance comparison between both industrial machines illustrated in Figure 2-4 above is shown in Table 2-1 below. Based on the performance factors highlighted below, the PKM offers more capability compared to SKMs. Both machines are specific to their manufacturing applications and availability of floor space. However, in relation to the aims and objectives of this study, this research seeks to improve the SKMs ability and fill the research and manufacturing gap on the following performance factors that are indicated in Table 2.1, namely: 1) Load distribution among actuators/joints; 2) improved stability and arm rigidity; 3) smaller positioning errors; 4) higher stiffness; and lastly, 5) higher repeatability. This outcome could hopefully make SKMs a more capable machine to meet the demands of contemporary manufacturing operations.

Table 2-1: Comparison between SKMs and PKMs

Serial Kinematic Machines (SKM)	Performance Factor	Parallel Kinematic Machines (PKM)
✗	Reduced energy consumption	✓
✓	Greater workspace to footprint ratio	✗
✓	Geometry independent performance	✗
✗	Lower sensitivity to environmental conditions	✓
✗	Lower manufacturing cost	✓
✗	Load distribution among actuators/joints	✓
✓	Simpler Control	✗
✓	Simple forward kinematics	✗
✗	Simple inverse kinematics	✓
✗	Greater speed and acceleration	✓
✗	Improved stability and arm rigidity	✓
✗	Smaller positioning errors	✓
✗	Higher stiffness	✓
✓	Dynamic behaviour resistant to payload variations	✗
✓	Predictable dynamics	✗
✗	Higher repeatability	✓

Having discussed the advantages of PKMs above, the following section explores some of the robot machining challenges.

2.5 CHALLENGES INVOLVED IN ROBOT MACHINING

The complexity of generating a robot's motion plan for high-force manufacturing operations is a problem for workpieces that contain complex geometries. Many concerns related to robot programming have considered online programming methods. Conventionally, these methods have been processed by skilled workers who guided the robot through specific path plans using a teach pendant. This technique was referred to as the "jog-and-teach method". The approach made it hard to adapt to machining operations, especially deburring operations, since it involved several teaching points and required high position accuracy. In addition, the operator was required to be present near the robot and guide its motion, which was a tedious and time-consuming process. The latter's solution was offline programming methods that could retrieve the robot's task from CAD data [59]. This method provided more flexibility and accuracy and was feasible for large batch sizes. However, due to the dependency on the modelling aspect of the robot and workpiece, additional calibration was essential to meet the process accuracy requirements [60].

There are three problems preventing manufacturers from using SKM as an alternative to conventional CNC machines. The first being the robot deflection produced due to the interaction force between the tool and workpiece. This negatively impacted machining with robots, especially during milling operations, as high cutting forces were experienced. The stiffness presented in most articulated robots is usually below 1 N/µm, while CNC machines experience much higher than 50 N/µm. As a result, force-induced deformation contributed to the inaccuracies of finished surfaces. A robot program that did not account for contact force and deformation became flawed during high precision tasks [61].

The second problem is the low stiffness, which presents a disadvantage for the machining of casting specific parts with complex geometries. The machining forces fluctuated drastically and imposed uneven robot deformations [61].

The third problem was the effects of vibration, commonly referred to as "chattering", which occurred during the machining process. The impacts of chatter affect the quality of the machined part and the tool and spindle lifespan. The vibration phenomena usually occurred when non-optimal machining poses were applied during the manufacturing task. Chattering became a serious issue in robotic machining coupled with the robotic system's low stiffness [62-64].

Today, the complication of robot programming presents a hurdle for adopting SKMs on the manufacturing floor. In that, both online and offline programming techniques are still unaffordable, challenging, and time-consuming.

The two parameters that govern the accuracy of serial robots during machining applications are *geometrical* and *compliance errors*. The former refers to manufacturing tolerances, which leads to geometrical parameter deviation of the nominal values, while the latter deals with end-effector deflections caused by the cutting torques and forces (compliance errors). This section concludes with a brief description of the methodology utilised in this study. This is described next.

The methodology followed in this research comprised four principal components. First, an analysis of the Fanuc M10-iA workspace was conducted to identify the end-effector's reachable points. Secondly, a kinematical singularity analysis was investigated to identify the unreachable points and spaces. Thirdly, a dexterity analysis using an IK approach was performed to identify permissible joint ranges in terms of Euler angles $(\alpha, \beta \ and \ \gamma)$ at various points within the SKMs workspace. Lastly, stiffness modelling was performed using the VJM. The principle behind the dexterity analysis was to identify optimal postures that possess greater stiffnesses, and to simplify the stiffness formulation.

The sections below provide a detailed overview of the robotic workspace (section 2.6), the kinematic singularity (section 2.7), dexterity (section 2.8), and stiffness (section 2.9). These are discussed below under their respective headings.

2.6 Robot Workspace

The first principal component of the methodology applied in this study is *robotic workspace*. This component will be discussed in more detail in this section. The precise computation of a manipulator's workspace and the boundary has received much attention due to its impact on manipulator design, placement in an environment, manipulator dexterity, and operational efficiency [65]. The most common method to determine the workspace uses the kinematic model from the (D-H) representation for SKMs. The technique is purely analytical and identifies the singular behaviour of the manipulator [66].

Manipulator workspace is defined as the total number of positions that a point, in our case, the manipulator's end-effector, can reach. The *workspace boundary* can be described as a curve (in-plane) or surface (in-space) that defines the end-effector's degree of reachability. Furthermore, the *workspace boundary determination* is an intermediate but critical step in the synthesis and design of manipulators. Hence, the determination method had to be accurate, robust, and fast [67]. To identify various characteristics of the workspace, it was imperative that the boundary was well-defined. This provided a transparent platform for existing manipulators or designing a new manipulator to be compared [67]. Most literature focused on robot kinematics to develop a set of poses that the robot's end-effector can assume throughout various configurations. The general shapes of a robot's workspace varied depending on its kinematic structure, and due to its complicated nature, it usually was in the form of a two-dimensional (2-D) or three-dimensional (3-D) spherical or cylindrical shape.

In general, a manipulator's workspace is subjected to the following constraints [68]: minimum and maximum link lengths, or stroke length if dealing with prismatic joints; limited ranges of revolute and spherical joints; and collision avoidance of links and or end-effectors. The essential characteristics of the manipulator positional workspace can be based on three principles, namely: Firstly, its shape and volume. For the serial type manipulators, the shape is an uninterrupted revolution obtained when joint one is revolute, as seen in Figure 2-5a, and of parallelepiped shape when the joint one is prismatic, as seen in Figure 2-5b. The shape is described as a solid bounded by convex/concave surfaces for parallel architectures, as seen in Figure 2-5c. Secondly, the robot's distance can reach, including its range, which can help identify the limits of the workspace to develop a robot work cell layout, or develop plans for task placement, based on the robot's configuration. Lastly, the profile and extension of voids, which are areas within the workspace that the manipulator cannot reach, will be further discussed in Chapters 4 and 5.

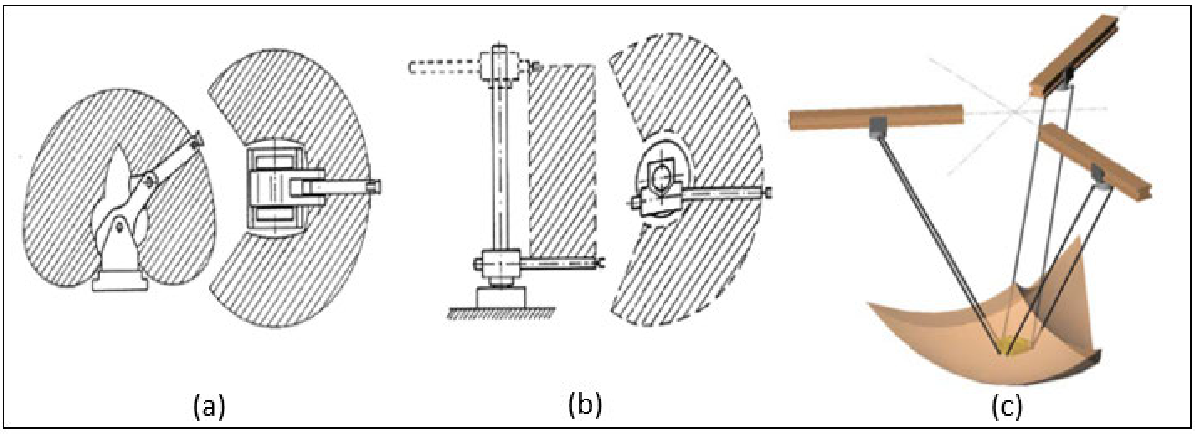

Figure 2-5: Workspace for a a) Serial Revolute Joint, b) Serial Prismatic Joint, and c) Parallel Manipulators

Efficient workspace identification methods are deterministic on the type of robot and are tailored to suit specific manipulator designs and configurations. The inclusion of joint limits regarding manipulator workspace has been identified and presented by Zaplana and Basanez [69]. Other similar works investigating joint limits in manipulator workspaces have been conducted by Peidró, Reinoso and Gil [70], Jha, Chablat and Baron [71], and Dong, Du and Chirikjian [72]. As emphasised, the selection of a workspace identification technique is based on the robot architecture and joint configuration, as a result, these studies supplied various methods to apply the forward kinematic solution, with the inclusion of the robot's joint coordinates for this research. This was important for this research, as the workspace development should ideally provide a cloud of reachable points to test the stiffness methodology presented in Chapter 8.

Additionally, some key developments in robotic workspace development were performed Iqbal *et al.* [73]. Their research focused on developing a kinematic solution to model a 6-DOF ED7220C SKM and further investigate the robot's workspace, using Robotics Toolbox for MATLAB®. This toolbox is pre-built with various functions and algorithms to analyse, calculate and visualise the kinematics of robotic architectures, like that of the Fanuc M10-iA robot used in this study.

Additionally, the Monte Carlo method is a numerical technique used to solve mathematical problems by random sampling. This technique is popular in workspace evaluation since it does not involve inverse Jacobian calculations [74]. Such a technique was studied by Cao [74], who determined a 2-D workspace of a 3-axis spatial robot manipulator using the Monte Carlo method. This method used a point-cloud non-uniform density technique by generating 6,000 random numbers with uniform distribution. It is important to mention that the technique's efficiency was improved when the density distribution of the Monte Carlo points was used [75]. The workspace topology using the Monte Carlo method was a point cloud based in 2-D and 3-D, such topologies are similar to that of the Fanuc M10-iA robot, and other robot brands with similar kinematic structures, which is usually specified under the manufacturer guidelines and robot manuals.

Further analysis of serial manipulator workspaces has been undertaken by Abdel Malek and Yeh [76], Abdel Malek and Yeh [77], Abdel Malek *et al.* [78], Abdel Malek *et al*. [79], Abdel Malek *et al*. [80], and Abdel Malek and Yeh [81]. Moreover, the relationship that exists between manipulator performance and kinematic geometry was established by Kumar and Waldron [82] in their innovative research. This study draws on the insights of these various studies.

Various methods can be used to describe the workspace or boundary of a manipulator. The technique is dependent on the manipulator's architecture. Conventional methods that exist in the literature include [83] *analytical* and *numerical* methods. The *analytical method* was used to condense the system of elements required to analyse and plot the functional workspace. Each variable, such as the joint angles, were modified, and the output results were inferred. This approach allowed for each joint angle to be analysed in insolation. In theory, the analytical approach requires plentiful information to arrive at a final solution and necessitates a visual representation of what the user performs at each step. The analytical investigation aimed to output a visible profile of the functional workspace using the Denevit-Hartenberg (D-H) parameters and joint limits. The approach extended itself to automation for many robot configurations, reconfigurations, and other alternate scenarios [83].

On the other hand, *numerical methods* were commonly used to identify manipulator workspaces by solving formulations that could not be expressed in a closed-form solution [84]. Three commonly employed strategies were used to analyse a manipulator's workspace, namely: continuation methods; branch-and-bound algorithms; and discretisation methods [83]. These are described in more detail below.

Continuation methods begin with a system of known solutions which incrementally transform the systems into its required solution state while tracing all possible solution paths along the way [85]. *Branch-and-bound algorithms* are global optimisation methods used for non-convex problems. They can be used to solve complex equations and or inequalities within a specific numerical space [49]. *Discretisation methods* are compelling numerical methods comprised of a grid of nodes that are a discrete subdivision of the operational space. Therefore, each node is required to satisfy specific requirements to be a part of the workspace. The established platform of these nodes provide a discrete representation of the manipulator's workspace [83].

Numerical principles to understand the workspace of a standard multi-degree of freedom manipulator was developed by Haug and colleagues [86]. It was based on the study of row-rank deficiency of the Jacobian matrix. In this research, an analytical approach to the workspace problem was used. The method used the D-H approach, and the singularity analysis also stemmed from the same formulation. Both the workspace and singularity analyses are further detailed in Chapters 4 and 5, respectively.

In a manufacturing environment, when hundreds of such manipulators are needed to accomplish an objective, manipulator workspace is essential in determining where the manipulator is located, how fast it completes its task, and at what cost. Formulations for avoiding collisions of manipulator's arms with the environment also rely on workspace analysis. The workspace is indefinitely one of the elemental analyses in robotics, and for this reason, the understanding of the Fanuc's workspace was crucial for this study. Apart from shedding light on the workspace, it was important to elucidate the physically reachable points by the end-effector. The deduction that singular values or singular configurations are attained at the workspace boundary was developed by Litvin [87]. The concept of "singular configurations" restricts the movement and reduces a manipulator's capability to perform a task within the robot's workspace. This probed for the singularity analysis of the Fanuc M10-iA in Chapter 5.

The second principal component of the methodology applied in this study is *robotic kinematic singularity*. This component will be discussed in more detail next.

2.7 ROBOT KINEMATIC SINGULARITY

The American National Standard [88] defines "kinematic singularity for Industrial Robots and Robot Systems – Safety Requirements (ANSI/RIA R15.06-1999)" as "a condition caused by the collinear alignment of two or more robot axes resulting in unpredictable robot motion and velocities". A robot's performance is compromised at or near a single region. Understanding the functionality and accessible workspace of a manipulator, negated by any singularities, ensures optimal performance in an industrial setting [88]. Aggarwal *et al.* [89] proposed that kinematic singularities result through a loss of DOF of the end-effector. During such an occurrence, two or more robotic arm joints do not independently control the end-effector's orientation and position.

To further understand kinematic singularity, it is essential to investigate the *velocity components* and the *Jacobian matrix*. Numerically, the forward kinematic equations define the relationship between the manipulator's Cartesian space regarding its position and orientation and joint space position. The velocity functions are expressed by the Jacobian matrix of this function [90]. The Jacobian matrix plays a vital role in the analysis and control of a manipulator's motion. Its application ranges from converting forces and torques of the end-effector, robot's joints to trajectory planning, and execution. Another aspect of the Jacobian matrix, in specific, is its determinant, which can provide the singular configurations of the robot [91].

In more recent scholarly work, Almarkhi and Maciejewski [92] presented a technique to detect singularities of any rank and any kinematic structure. The method proposed involved computing the gradient of singular values of the Jacobian matrix. The algorithm could handle two or more singular values that converge with their singular vectors being ill-defined. Another algorithm was also developed to determine the singular directions' physical interpretation using a high dimensional singular subspace of high-rank singularities. Their study was applied to a 4- and 6-DOF robot. Similarly, the singularity study of the Fanuc M10-iA seeks to analyse various singularity types, both within the workspace envelope and at the boundary, which involves the study of subsets of the Jacobian matrix, which is discussed in the upcoming sections.

Aggarwal [89] highlighted the importance of the singularity identification technique as follows, which further motivated the investigation into kinematic singularity in this research:

- Information regarding singularities allows for the functional workspace of the end-effector to be easily determined.
- Boundary singularities (singular configurations) help to identify the boundary of the robot's workspace.
- Singularities represent a design tool for identifying the mechanical structure and joint limits of the robot.
- Singularities help determine the unattainable configuration for specific directions of motion.
- The control algorithms fail at or near singular configuration, which results in the hindrance of joint velocities and acceleration for the smooth function of the robot.

A robot with n joints, with a $6 \times n$ Jacobian $J(q)$ matrix, describes the mapping between the vector of joint velocities and the vector of end-effector velocities.

$$dx = J(q)\, dq \qquad [2\text{-}1]$$

A specific set of joint coordinates that decreases the Jacobian matrix's rank was referred to as a "singular configuration". The importance of emphasising this topic, especially in this research, was because [90]:

- Singularities prevent the motion of specific configurations.
- At singularities, large joint velocities may result from small end-effector velocities.

- At singularities, large joint torques may result from small end-effector forces and torques.
- Singularities could represent boundaries within the manipulator's workspace.

A unique solution to the IK problem is not possible near or at a singularity. Consequently, such cases may lead to infinitely many solutions or no solution at all. Since the dexterous posture identification relied on an IK approach, the need for performing a singularity analysis is further justified.

Yoshikawa [93] presented a scalar value called "measure of manipulability" given by equation [2-2]:

$$w = \sqrt{\det(J(\theta)\, J^T(\theta))} \qquad [2\text{-}2]$$

This equation provided a measure for a given manipulator configuration. Oetomo and Ang [94] used this measure to differentiate various behaviours of their control algorithm. Additionally, the authors engaged in the various methods used to identify and handle singularities by defining two main approaches.

The first was a uniform control approach which was implemented throughout the workspace, developing a continuous function that incorporated a small variation to the task space description or through direct mapping to the robot's joint space. The method provided a controlled strategy whereby the end-effector avoids all singular configurations. The second approach was to partition the robot workspace with a different control strategy being applied to the region surrounding the singularities.

As the robot approached a singular configuration, its motion and force along that direction were uncontrollable. However, if a motion along that singular direction was required, a null space motion, which resembled minimising a possible function corresponding to the task goal, was needed. Oetomo and Ang [94-96] divided singularities into two categories according to the null space's effect. These two singularity types were computed for the Fanuc M10-iA robot in this research. The two types of singularities are:

- **Type 1 singularities:** When the null space motion produces an end-effector motion in a singular direction and results in the end-effector voiding the singular region via this direction. This can be graphically depicted in Figure 2-6.

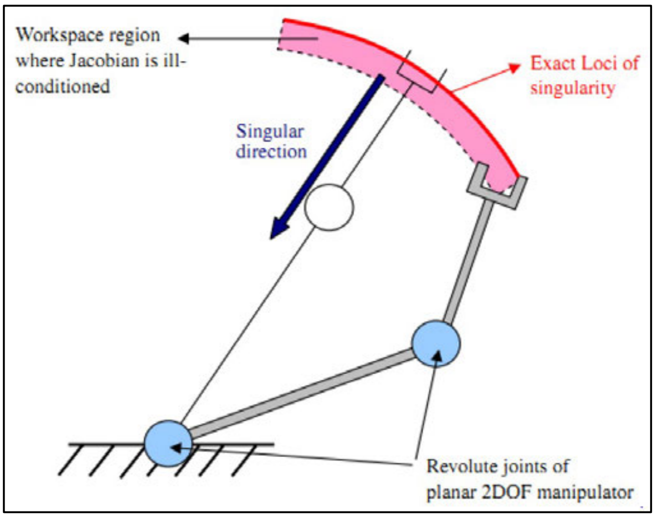

Figure 2-6: Type 1 Singularity [94]

- **Type 2 singularities:** When the null space motion only affects the internal joint motion and adjusts the singular direction without affecting the end-effector forces. This is graphically represented in Figure 2-7.

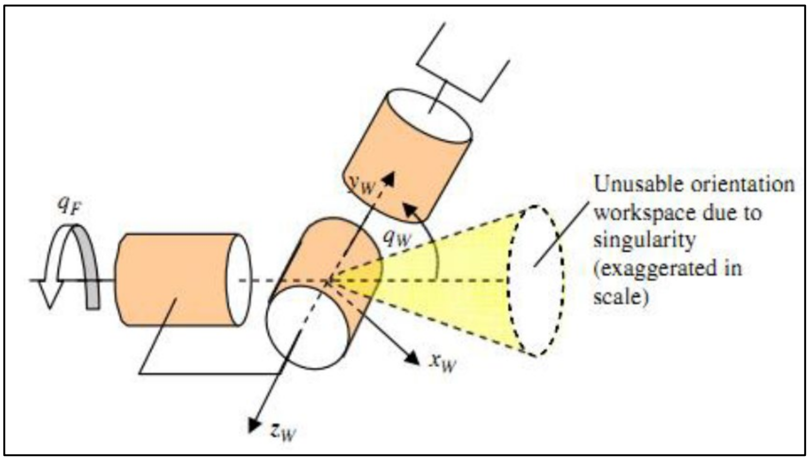

Figure 2-7: Type 2 Singularity[94]

The identification of singularities and the workspace analysis in this research allowed for a suitable testing platform to be developed. The idea was to measure the stiffness at multiple equidistant points and postures from the robot's base and compare the stiffnesses, starting with points surrounding the base, and moving outwards towards the workspace boundary. Additionally, these analyses were important during the dexterous analysis since not every point is reachable, or some points might be constrained in terms of configuration possibilities.

The third principal component of the methodology applied in this study is *robotic dexterity*. This component will be discussed in more detail next.

2.8 ROBOTIC DEXTERITY

Dexterity, depending on its application, is well defined within the field of robotics. The industry has defined "robotic dexterity" as the robot's ability to perform a diverse range of assembly operations without having to custom design specific fixtures or tool changes [97]. In a technical sense, Angeles *et al.* [98] defined "dexterity" as the ability to manoeuvre and apply various forces and torques in arbitrary directions effortlessly. Therefore, the concept was linked to the knowledge of *kinetostatics*, which is the study of the interaction between viable twists and constraint wrenches in multi-body mechanical systems under static conservative conditions. Robotic dexterity was formally considered *manipulative dexterity*, which was analogous to *human hand dexterity*. A number of studies [103, 104] indicated that hand dexterity was insufficient to perform flexible manufacturing operations. Instead, an in-depth analysis of the robot's global dexterity was preferred. However, although some definitions categorise manipulative dexterity under global dexterity, it still had relevance towards human hand dexterity. Manipulative dexterity has been thoroughly investigated by Bullock *et al.* [99], who cited various authors suitable and relevant definitions. These are noted below:

- "(The) capability of changing the position and orientation of the manipulated object from a given reference configuration to a different one, arbitrarily chosen within the hand workspace" (Bicchi [100], cited in Bullock *et al.*),
- "(The) process of manipulating an object from one grasp configuration to another" (Li [101], cited in Bullock *et al.*),
- "(When) multiple manipulators, or fingers, cooperate to grasp and manipulate objects" (Okamura [102], cited in Bullock *et al.*),
- "(The) kinematic extent over which a manipulator can reach all orientations" (Klein and Blaho [103], cited in Bullock *et al.*),
- "Skill in use of hands" (Sturges [104], cited in Bullock *et al.*)

The literature often categorises a manipulator's dexterity according to the number of DOF or their range of motion. The importance of manipulating objects with optimal dexterity accentuates its similarity to human hand dexterity and its requirement for manual and fine motor dexterity. It was evident from the above definition that a robot's dexterity is not only motion dependent, but also depends on its sensing and control capabilities [102]. A comprehensive assessment of the robot's dexterity is required to assess a manipulator's overall performance fully. Accordingly, there were two benchmarking stages to assess dexterity, namely, *componen*t and *system-level* benchmarking. Several dexterity assessments and approaches have been performed on different robotic component systems [102].

In their study, Kumar and Waldron [82] defined "dexterous workspace" as the ability of a reference point on the manipulator's hand to reach every point within a specific volume in any anticipated orientation. Additionally, the authors defined a numerically bounded dexterity index, which was dimensionless and represented the manipulator's capability to realise different orientations at a specific point, a similar concept to the IK approach used to solve the dexterity problem discussed in Chapter 6.

Furthermore, Guo *et al.* [105] developed a posture optimisation to improve the stiffness of a robot for machining operations. The method was based on applying a performance index at various postures and analysing the association between the translational deflection of the robot's end-effector and the applied force. The performance index, being frame invariant, was maximised to develop a posture optimisation model. This study is significant to the current research, since both studies share a common aim in improving stiffnesses in industrial robots; however, in the current research, instead of optimising the stiffness, a dexterous posture identification technique is proposed to assist in locating stiff areas and configurations for tasks that involve high applied forces and vibrations.

A 6-DOF wheeled robot designed for pick-and-place operation to assist nurses in medical settings was developed by Mondragon [106]. To develop a capable machine to meet these requirements, for pick-and-place operations, the following analyses were investigated: an inverse kinematic problem, collision avoidance, workspace, singularity and dexterity. The inverse kinematic solution to the dexterity problem was adopted from this study, and applied to the current research. The difference here was that the inverse kinematics was applied to statically locate multiple configurations at a point, rather than dynamically, along a path. This will be further investigated in Chapter 6.

This section provided a discussion of *robot dexterity* as understood within the field of robotics. Various scholarly definitions and methods were deliberated to help with this task. In light of the existing literature and works around dexterity, the concept proves beneficial when modelling and identifying the stiffness of SKMs. Provided that the robot has an optimal posture, the dexterity analysis not only simplifies the stiffness modelling, but also due its ability to improve robotic actuation, reduce backlash in the robot's joint, and promotes better distribution of stress within the robot structure. With these insights in mind, the following section focuses on *robotic stiffness* – the fourth principal component of the methodology applied in this study.

2.9 Robotic Stiffness

SKMs have grown popular in industrial facilities for tasks that require excellent repeatability but not necessarily high accuracy. These tasks include general pick-and-place, painting, and welding operations. Nevertheless, in modern times, they are currently being used for machining operations such as sanding, sawing, trimming, etcetera, and therefore require high precision and stiffness [107]. As a result, improved kinematic and elastostatic properties are essential to ensure success in these operations. It is also important to assess link and joint deflections for manipulators that are required to move accurately and fast [108].

According to Carbone [36] and Yoon [109], three factors define robotic stiffness, namely: *joint stiffness*, *robot configuration,* and *applied forces*. The positional accuracy of robots is attributed to the links and joints' general stiffness [11]. Stiffness may be regarded as a robot end-effector's ability to withstand loads without significant changes to its geometry. During the end-effector's loaded case, these applied forces determine the extent of deflection of the end-effector [110]. Other intrinsic characterises of the manipulator, such as backlash and tolerance in the actuation elements, materials used and dimensions of the links, govern the robot's effective stiffness [11]. This is relevant for the current study because the three factors that define robotic stiffness was detailed and investigated in this research.

According to worldwide statistics analysed by the IFR [113], 72.7% of all industrial robots are being applied to assembly tasks, welding, and general pick-and-place operations. However, such rudimentary operations are only providing a replacement for repetitive manual labour. Compared to other alternative machining tools, the lower costs and flexibility of SKMs are shifting and advancing their usage to more complex manufacturing operations. Robotic stiffness is affected by the compliance of reducers; typically, a 6-DOF SKM has stiffness values lower than 1N/μm, with a natural frequency of 10 Hz. On the contrary, CNCs have stiffnesses greater than 50 N/μm with high natural frequencies [111]. The low stiffness inherent in SKMs makes them more vulnerable to static and dynamic deformations during high-force manufacturing operations. Additionally, chatter vibrations could result during excessive loading on the end-end effector during a manufacturing operation [112]. The force-induced deflection deviates the tool from its original position and trajectory, leading to poor surface finishes and dimensional errors. Therefore, this necessitates further analysis and investigation into improving the stiffnesses and natural frequencies of SKMs.

According to Schneider *et al.* [113], backlash impacts a robot's gears and drives, especially when the applied load on the end-effector changes rapidly, or the end-effector experiences rapid motion; as a result, the robot's gear reduction system induces unwanted vibrations and resonances. The problem with current industrial serial robots is contour errors, which are prominent during curve tracking. When the robot moves at relatively low speeds, the contour errors are of acceptable accuracy. However, once rapid and accurate trajectories are required, such as laser cutting, deburring, and jet cutting, contouring errors are of a much higher magnitude [114]. This study provided incentive into the dexterity and stiffness approaches, as the research serves to fill the gap encumbering low precision manufacturing using SKMs and supplement alternatives to promote complex, high-force manufacturing tasks.

In dealing with pre-existing robots, characteristics such as mechanical transmission, dimension and materials, and actuators are nearly impossible to change. Therefore, it can be confirmed that the stiffness of a robot is based on identifying optimal configurations. Several authors concur with this observation [105, 112, 115, 116].

The various robotic stiffness models that exist in the literature include the Finite Element Analysis (FEA), the Matrix Structural Analysis (MSA), and the Virtual Joint Method (VJM) [58]. These are explained in more detail below. The most popular technique is the VJM, which models the joints as linear elastic torsional springs. The VJM is an extension of the conventional rigid body model of a manipulator, which assumes the links to be rigid bodies and joints to be compliant [117].

2.9.1 Modelling Of Industrial Robotic Stiffness

This section provides an overview of the three possible modelling techniques that can be used to model industrial serial robots' stiffness. In this sense, this research addresses Objective 3 of this study which seeks to *research, establish and identify a suitable stiffness modelling approach.* To ensure adequate compensation of compliance errors for robot-based machining applications and other precision tasks, suitable stiffness models that accommodate both changes in manipulator configuration and influences of external forces/torques are required. As previously mentioned, robotic stiffness can be modelled according to three main groups [118]: FEA, MSA, and the VJM. These are discussed in more detail below under their respective headings.

2.9.1.1 Finite Element Analysis (FEA)

Simply put, the FEA decomposes the robot's actual model into small finite elements and demonstrates compliant relations between adjacent nodes described by the robot's stiffness matrix. These elements include standard shapes such as pyramids, cubes, etcetera, which permits the stiffness matrix to be computed analytically. Such discretisation allows for the static equilibrium equations representing each node to be derived. The system of equations are then aggregated in a global matrix expression. The global matrix defines the relationship between the applied force/torque and the node deflections. The matrix is then inverted and applied to the stiffness matrix by the process of the simple extraction of proper elements.

However, due to the advancements in the modern CAD environment, the above procedure is automated. Precisely, the decomposition into finite elements, is defined via the discretisation step and mesh type only. The various mesh types include the linear and parabolic type. The CAD-based tools provide a numerical interpretation of the model and graphical displays of the deflection vectors at each node and potentially hazardous areas with high stresses and strain [118].

Furthermore, the FEA model's advantage is its high accuracy that is limited by its discretisation step. This is advantageous for robotic operations since the joints and links are usually modelled with exact dimensions and shapes [119, 120]. Increasing the discretisation step or number of finite elements, translates to limited computer memory, thereby making it more difficult to compute complex matrix inversion. Apart from the intensive computational efforts, the matrix inversion generates numerous accumulative round-off errors, which reduces the overall accuracy. In robotic applications, this induces severe computational expenses due to the re-meshing and re-computing [121]. In some instances, the FEA technique, combined with the VJM, can limit the computational expense for different manipulator configurations.

The next section provides a more detailed description of the MSA method.

2.9.1.2 Matrix Structural Analysis (MSA)

Having described the FEA model in the section above, this section looks at the MSA method. In short, the MSA method encapsulates most ideas from the FEA method; however, instead of decomposing the structure into finite elements, it operates with compliant elements such as arcs, cables, and beams. This reduction in the model reduces the computation expense and, in some cases, allows the analytical stiffness matrix to be obtained. Similar to the FEA analysis, the MSA provides force vectors at each node, but where it varies, is that it provides a concise and clear physical interpretation (active or passive joints), which is beneficial for some tasks [122]. From a computational viewpoint, the MSA method is more straightforward than the FEA approach. Although the MSA method integrates matrix operations of complex dimensions, it provides a decent trade-off between model accuracy and computational time, provided that an accurate representation of the link approximation is made by either the arc or beam elements. Both the FEA and MSA methods provide closed-form solutions, in that both interpret the physical system as a set of nodes with flexible and mutual connections. The primary difference between the MSA and FEA methods is that one operates with true physical objects such as beams and arcs, while the other method decomposes the physical structure into finite elements [118]. This section described the MSA method and clarified the difference and similarities between the MSA and FEA methods. The VJM will be the focus in the section below.

2.9.1.3 Virtual Joint Method (VJM)

Salisbury [123] developed the first closed-form solution for the Cartesian stiffness matrix by assuming that the robot's mechanical elasticity came from the actuated joints. The method was developed on the extension of the conventional rigid body model of a robotic manipulator, where the links are assumed to be rigid, and the joints compliant, to amass all flexibility in the joints only. This matrix forms the basis for manipulator stiffness analysis. The *Conservative Congruency Transformation* (CCT) method was used to define the joint and Cartesian stiffness matrices. Geometrically, this approximation is comparable to adding to the joints an auxiliary virtual joint with embedded virtual springs. This approach of such a lumped presentation of the manipulator stiffness that, in reality, is essentially distributed, simplifies the model. Presently, the VJM is the most applied model to approximate the stiffness of SKMs [118]. Salisbury [123], assumed that the main flexibilities were located at the actuator joints. The derived expression that defined the joint and Cartesian stiffness matrices using the CCT method became the foundation for robotic stiffness analysis. The concern with this method is defining the virtual spring parameters. According to Pigoski *et al.* [124], each actuated joint is assumed to be represented by a single 1-D virtual spring. Additionally, Majou *et al.* [125] considered the link flexibilities; the number of virtual joints increased, and in each actual actuated or passive joint, several translational and rotational virtual springs were integrated.

In recent developments of this area of modelling, robots operate with 6-D virtual springs using the FEA method. The advantage of merging both methods increases the accuracy of the VJM, making the results comparable to that of the FEA; however, with lower computational expense [126]. The following section explores existing literature on the VJM method.

2.9.2 Related Work on the Virtual Joint Method

It was overtly assumed that the primary source of elasticity was focused within the actuated joints. In conjunction, the manipulator links were assumed to be rigid and the joints elastic, which were modelled as 1-D springs. In modern works, compliance of the links has been accounted for by implementing additional virtual joints that describe their longitudinal elasticity or stiffness properties in a multi-directional approach [125]. Recent advancements in this area use 6-D virtual joints to define each link's elasticity [127].

The stiffness identification procedure in this research uses the concept of “virtual springs”, as outlined in the VJM technique. According to Klimchik [20], the advantage of the VJM is its ability to accurately represent the stiffness components of a robot and simplify the modelling approach [118]. As a result, this method was chosen to model the Fanuc M10-iA robot.

A fundamental step in the VJM technique is defining the virtual spring parameters. According to Pigoski *et al.* [124], each actuated joint is assumed to be represented by a single 1-D virtual spring. Majou *et al.* [125] further added to Pigoski’s work by considering the link flexibilities of a PKM. The study focused on actuated and passive joints, including the translational and rotational effects of the links, which were replaced by virtual springs.

According to Knapczyk and Ryska [128], two approaches were established to acquire the Cartesian stiffness matrix of an SKM. The first approach involved clamping of all joints except one to measure the robot's elastic deflection under an applied wrench (force/torque). The joint stiffness matrix was computed by repeating the process for each joint; hence, only n experiments were needed to model a n-DOF SKM. This method was completed carefully while running the motors to avoid any permeant damage to the robot links and joints. The second approach dealt with measuring the end-effector's linear and rotational displacements due to an applied wrench through means of interpolations. The latter method was preferred as it provided accurate results and was safer as several results were acquired for various robot configurations, and as a result, this technique was applied in this research.

For a mechanism consisting of rigid links and compliant joints, the static equilibrium equations are derived and linearised to obtain the Cartesian stiffness matrix, which depends on the manipulator's posture. The elastic deflection in the virtual spring is usually assumed to be relatively small, and linearisation is usually performed within the neighbourhood of the equilibrium configuration, conforming to zero forces and torques, representing the unloaded case [118].

In the method proposed by this research, the robot's end-effector response to an applied wrench (force/moment) under static equilibrium was estimated through the Cartesian stiffness matrix of the robot. The matrix was a predecessor to developing results to the linear and angular deflections of the robot's end-effector.

Current studies that have found a correlation between robotic workspace, kinematic singularity, and dexterity are reviewed next.

2.10 Relationship Between Robotic Workspace, Kinematic Singularity, Dexterity, and Stiffness

Studies that have linked robotic workspace, kinematic singularity, and dexterity are highlighted and discussed in this section. Other research that has implicitly considered the trio of analyses relating to stiffness identification techniques are also described in detail. The significance of each analysis in this study towards the posture identification technique is addressed. The literature considered that has combined two or more of the analyses discussed in this study include:

Malek *et al.* [78] established the idea that workspace boundaries can be generated from a set of output singularities. In particular, they focused their efforts on numerically tracing each singularity using continuation methods.

Malek and Yu [94] also analysed the necessity to carefully plan any manipulator's workspace, whether it be in robot-assisted surgical interventions or on the manufacturing floor. Their statement supported the idea that robot placement and location of the robot's base was crucial to maximise dexterity at or around a point.

Additionally, Goyal and Sethi [66] developed the idea that workspace identification, with its boundary singularities, was crucial due to its impact on manipulator placement, manipulator design, and manipulator dexterity.

Nadal [129], on the other hand, detailed the importance of performing a singularity analysis in conjunction with identifying the workspace of the robot. The study aimed to analyse specific configurations and their effect on the robot's kinetostatic properties. Additional effects such as motion control and dexterity losses were found, which gave rise to uncontrollable and unresolvable end-effector forces.

The four above-mentioned studies were significant for the current study since the joint stiffness testing must be based on a point coordinate system, ranging close to the robot base and the workspace boundary. Consequently, a singularity analysis and an understanding of the functional and reachable workspace played an essential role in identifying an optimal setting for the point coordinate system and dexterity study. The dexterity analysis focused on identifying possible configurations at a point in space. Without prior knowledge of the functional workspace and singularity investigations, the number of possible configurations would be restricted since there would be no prior knowledge of whether a configuration was possible or not.

Furthermore, Porges *et al.* [130] studied the development of a unique formulation that discretises the workspaces into voxels that contain several cells. By applying the forward or inverse kinematics, each cell was defined by a binary value that identifies it as reachable or not. This idea led to the development of a reachability map. The inverse applied to the map provided the robot with placement opportunities depending on its desired task. Each cell was accompanied by a quality index, which measured the dexterity of the robot at the desired position. This led to the development of a capability map.

Then, Malek and Yeh [93] presented an analytical method to determine the global dexterity of a robotic system. The technique relied upon defining all singularities present within the robot's workspace as well as the singular surfaces and curves. These singular surfaces that extend towards the boundary of the workspace were intersected with a service sphere. The results obtained via this formulation proved to be highly analytical and accurate, but also provided several limitations. The identification of singularities, mainly wrist singularities, affects the number of configurations that are reachable at a point in the workspace. This was important for the current study and was also confirmed by Roberts [131].

Moreover, Mohammed *et al.* [132] mentioned that various performance characteristics such as dexterity, manipulability, and stiffness are crucial metrics in designing and analysing robotic manipulators. In their works, manipulability was defined as the ability of the robot to manoeuvre in various directions. In contrast, stiffness, which implied the robot's accuracy, was the degree to which a manipulator can return to a previously taught point. Additionally, the works provided more insight into a manipulator's workspace and dexterous workspace, and how it can be related to the overall workspace. Other researchers who have focused on similar works incorporating manipulability index optimisation, include Engardt *et al.*[133].

Based on the above literature consulted, a strong relationship was found between each variable analysed in this research. This argument allowed further investigation into the stiffness modelling and application of a posture identification technique to locate stiff points and areas, which is analysed next.

A posture-based method forms the basis of this research and is further discussed in Chapter 6. A few of the significant contributions made by several authors to identify the stiffness parameters through posture identification as well as optimisation methods to improve stiffness, are listed below:

The first study mentioned here is by Schneider *et al.* [5]. These authors proposed a stiffness identification technique that was performed on various robot configurations that were heuristically selected to obtain experimental force and position data. A wrist force/torque (F/T) sensor and a laser-based tracking system were used to obtain the experimental results. The laser tracker system had an accuracy of ppm m/m, a distance resolution of 1.26 m, and coordinate repeatability of ppm m/m. Additionally, the system could measure the position of the target along three orthogonal axes. The algorithm used to estimate the stiffness values were based on a classical non-linear least-squares estimation. This study employed accelerometers instead of a laser tracker; however, this study served to confirm the stiffness trends measured for the Fanuc M10-iA.

In the next study reviewed, Klimchik *et al.* [134] implemented a VJM-based stiffness model with a gravity compensator attached to the second link of a serial robot. The assumption is that the gravity compensation torque was produced via a spring merged to an additional link, which created a closed-loop to be contained within the stiffness model. The focal idea was dedicated to identifying the model parameters and calibration experiment planning. Their approach was verified by experimental results dealing with compliance error compensation techniques for robot cells employed in manufacturing aircraft components. The mathematics of the VJM approach was confirmed using this study, along with other research by Klimchik [58, 118, 134]

Insightfully, Pham and Goutier [135] developed a band-pass filtering method to estimate the joint stiffness parameters, which was the primary source of flexibility in robot applications. Their approach was based on a series of unique tests by moving each joint while the rest were locked. The dynamic model simplified the analysis, which was linear relative to the gravity parameters (first moments), friction, stiffness, and joint moment of inertia parameters. These parameters were measured from a sampled data of motor currents and accessible position measurements using a least-squares method.

Another noteworthy study was conducted by Owen *et al.* [136]. These authors addressed the issue of the stiffness of a two-armed robotic sculpting machine using an integrated off-line planner and real-time re-planner. The accessible robotic stiffness was exploited during off-line planning via a trajectory resolution method, thus maximising the null space of the robotic system. A real-time trajectory re-planner employed a time-scaling method to account for the unmodeled disturbances, which decreased the tool speed and reduced the torque demanded by the robot's actuators, improving the overall dynamic stiffness capabilities. The real-time re-planning phase also accounted for conflicting performance criteria such as joint limits, stiffness, and collision avoidance. Their research mainly focused on identifying optimal trajectories that have high stiffness, whereas, in the current study, a static posture identification is presented. Their research is highly relevant here as stiff static points can extend this study towards dynamic machining by combining adjacent static points with high stiffnesses to plot optimal robot trajectories.

Also worth mentioning is the research by Dumas *et al.* [137]. These authors introduced a method to determine the optimal placement of a workpiece that required machining with prior knowledge of the cutting forces on the tool and the elastostatic parameters of their robot. The method was initiated by proposing a cutting force model to predict the range of forces applied by the tool on the workpiece. The joint stiffness identification model was incorporated to identify the stiffness of the robot. A mono-objective optimisation problem was developed to determine the optimum placement of the workpiece to be machined. Other authors who have focused on workpiece placement for optimal robot placement include; Spensieri *et al.* [138]; Dumas *et al.* [137]; Malhan *et al.* [139]; Lopes and Pires [140]; and, Pérez *et al.* [141] Again, the use of the VJM was confirmed in this study.

At least two of the three variables were used to identify a specific application, or the result of one variable was dependent on calculating the other. As a result, a secure connection exists between the three analyses used in this dissertation. Considering each study individually, and finally creating one unified product that combines all, successfully allows for precise identification of the stiffness parameters of the Fanuc M10-iA robot. A literature review matrix (Table 2–2) was developed to confirm the reliability of workspace, singularity, and dexterity on stiffness modelling, and identification of SKMs. The matrix highlights key authors for each analysis explored in this research.

Table 2-2: Literature Review Matrix Affirming the Importance of the Multivariable Approach

No.	Author	Workspace Analysis	Singularity Analysis	Dexterity Analysis	Manipulability	Stiffness
1	Abdolshah [142]	1	1	5	0	5
2	Arsenault and Boudreau [143]	5	5	5	0	5
3	Huang [144]	3	3	5	1	5
4	Dumas *et al.* [107]	0	0	5	1	5
5	Giuseppe Testa [110]	1	1	5	0	5
6	Li, *et al.* [145]	3	3	0	0	5
7	Schneider *et al.* [5]	2	1	0	0	5
8	Xiong *et al.* [146]	2	4	1	0	5
9	Zhang *et al.* [147]	5	0	4	2	4
10	Chen *et al.* [148]	3	0	0	2	5
11	Klimchik [118, 149]	4	4	0	0	5
Total		29	22	30	9	54

Table 2-2 synthesises the literature explored in this section on robotic workspace, kinematic singularity, dexterity, and stiffness, highlighting the importance of this study's multivariate approach. Some concluding remarks are provided next to wrap up this chapter.

2.11 CHAPTER SUMMARY

This chapter presented the effects of Industry 4.0 and its significance in the development of current and future robotic machines. The emerging trends in robotic machining regarding CNC and the robotic markets, both from a global and local perspective, were also explored. The consideration of PKMs and SKMs was further discussed, and a comparison between both was made. The challenges involved in robotic machining were also deliberated, followed by an in-depth literature overview on all the variables investigated in this research, including robotic workspace, kinematic singularity, dexterity, and stiffness, with emphasis on the VJM technique. These concepts were also discussed and defined by contemporary scholars in the field, providing a solid theoretical base.

In light of the above, this chapter partially addressed the following research objectives: *Research, establish and develop a dexterous posture identification method that can localise multiple configurations at a user defined point* (Objective 1); *Research, develop and simulate the workspace and singularities of the Fanuc M10-iA and understand their influence on the dexterity and stiffness analyses* (Objective 2); *and Research, establish and identify a suitable stiffness modelling approach* (Objective 3).

The conceptual framework of this study is presented next.

3. CONCEPTUAL FRAMEWORK

3.1 INTRODUCTION

This research focused on robotic stiffness identification. The process applied a dexterous posture identification technique to confirm that stiffness is posture dependent, and depending on the end-effector location within the reachable workspace, void of singularities, stiffness is either improved or worsened. As indicated in the literature review matrix in Table 2-2, the three analyses are highly interconnected. This chapter provides the blueprint of the analyses applied in the study (section 3.2). An investigation into the relationship between the workspace (sub-section 3.2.1), singularity (sub-section 3.2.2) and dexterity (sub-section 3.2.3) analyses are discussed, followed by the tools that are required to efficiently and effectively measure the joint stiffnesses (section 3.3). In this sense, this chapter builds on the insights of the previous chapter. Some concluding remarks are then provided to close the chapter (section 3.4).

3.2 ANALYSIS WITHIN THE FRAMEWORK

This section describes the methodology utilised for each analysis, namely, the workspace analysis (sub-section 3.2.1), singularity analysis (sub-section 3.2.2), dexterity analysis (sub-section 3.2.3), and stiffness analysis (sub-section 3.2.4). The technique employed for each analysis is also unpacked in detail.

3.2.1 WORKSPACE ANALYSIS

Determining the Fanuc robot workspace was at the forefront of the stiffness identification. The remaining investigations stemmed from identifying the workspace. The joint limits of the robot governed the workspace. Each study and test either fell on the workspace boundary or within the workspace itself. Workspace boundary identification is usually considered an intermediate but critical step in analysing and synthesising robotic manipulators. It was, therefore, critical to identify a fast and accurate method of determination. According to Dibakar and Mruthyunjaya [67], there are several modular kinematics to solve direct kinematics that allowed for a robot's workspace to be easily identified. Dibakar *et al.* [67] further elaborated on current heuristic methods and algorithms that were computationally efficient and robust.

Challenging mathematical formulations continue to persist in workspace identification. However, for each method, the conceptual framework remains the same [150]. Figure 3-1 below depicts the wrist centre, robot flange, and tooling workspace of the Fanuc M10-iA.

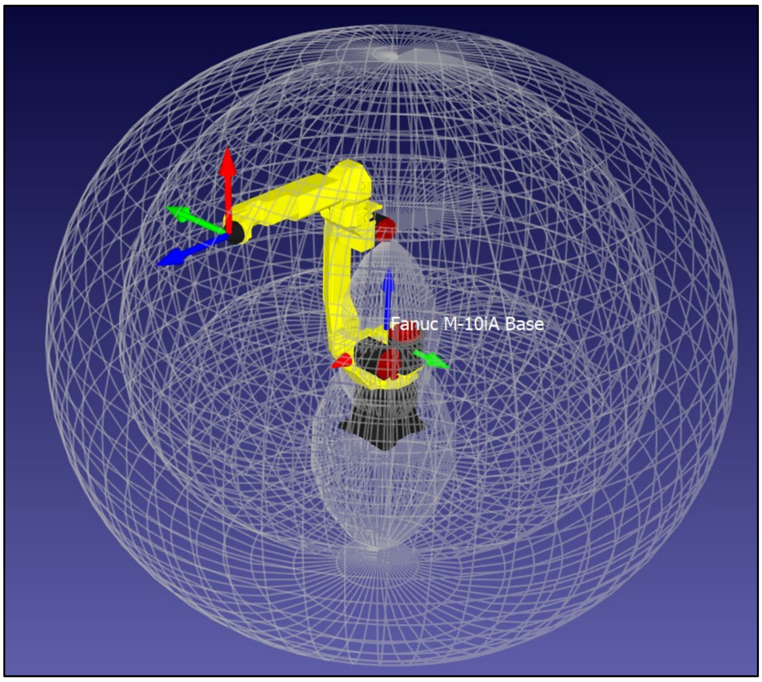

Figure 3-1: Workspace of Fanuc M-10iA Extracted from RoboDK

This visualisation of the robot was extracted from a robotic simulation software called RoboDK. This software provided an intuitive platform to control the robot analysed in this research. All joint coordinates, joint restrictions, and the robot's overall workspace were visible. These results, along with the robot's manufacturer guidelines, provided sufficient parameters to calculate and verify the forward kinematic solution, and plan and test the reachability of each point in the point cloud.

The analytical method applied to define the workspace of the Fanuc M10-iA robot was adapted from Aggarwal *et al.* [89]. The proposed workspace solution was developed by splitting the joint variables into intervals called "step sizes". The plotting of the joint values was randomised to prevent continuous data classes from forming. The method's application is discussed further in Chapter 4 and the forward kinematic solution and workspace results.

The focus of this sub-section was on workspace analysis. The following sub-section looks at the singularity analysis, followed by dexterity analysis thereafter. The purpose of this discussion is to establish the methodology applied to solve these variables.

3.2.2 Singularity Analysis

Several investigations are available in the literature [151-153] that characterise singularities and workspace boundary determination – two highly interlinking problems. Identifying the inner and boundary workspace singularities helped detect points in which the robot lost a DOF and regions unreachable by the robot. Defining the singularities early during the machining stage helped classify areas within the robot's workspace that were unfavourable for the stiffness tests. According to Donelan [154], kinematic singularities can affect the robot's overall performance and control, which can cause excessive torque fluctuation and forces on the robot's links leading to a reduction in stiffness or compliance and failure in control algorithms. Donelan [154] further proposed some rare design benefits in their presence, such as increased load-bearing, fine control, and singularity-free posture change. These results and the workspace analysis provided conclusive evidence on the available points to test for the stiffness methodology.

The singularity analysis applied in this research is adapted from Aggarwal *et al.* [89]. Similar to the workspace analysis, the singularities were analytically determined. The singularities were defined by subdividing the Jacobian matrix of the robot. Each component of the Jacobian matrix was used to determine specific singularity types. Further analysis of the technique is discussed in Chapter 5, along with the functional workspace and results. Dexterity analysis is described next.

3.2.3 Dexterity Analysis

The dexterous workspace is defined as a subspace within the manipulator's workspace in which the end-effector can assume multiple orientations. This phenomenon was important in identifying high stiffness areas. It is known that optimal robot postures are accompanied with improved stiffness performance. The principle behind the dexterity analysis was to locate and identify multiple configurations about a point within the robot's workspace. Since optimal postures occupy high kinematical properties, the ability of the robot to perform applications involving high force and torque fluctuations is improved, since the stress in the joints and link are more evenly distributed.

Additionally, the consideration of dexterity for robotic joint stiffness modelling simplifies the mathematical formulation in that the Complementary stiffness matrix (K_X), which is a highly non-linear matrix, can be neglected during the calculation. Additional information regarding the influence of the Complementary stiffness matrix on the modelling of SKMs has been investigated by Berntsen *et al.* [155], in which this study draws some important insights. This is discussed further in Chapter 7.

As mentioned in section 3.1, this study introduces a unique combination of analyses to solve the stiffness identification problem. This part of the research addresses the objectives concerned with workspace, singularity, dexterity, and stiffness (Objectives 2 and 3). The study combined another approach to replace the existing problematic conditioning number that defined robotic dexterity. The dexterity analysis adopted the methodology developed by Mondragon. [106] and Abdel Malek and Yeh [81]. The research applied an *Inverse Kinematic* (IK) solution to solve the dexterity problem. The dexterity analysis in Mondragon's study was initially developed for medical interventions. But now, its application has been extended away from gripper manipulability to locate optimal points, zones, and postures for high precision tasks. Note that the reference made to dexterous zones refers to all configurations at a point using the IK method. The method is further elaborated in Chapter 6, where the IK solution for the Fanuc M10-iA is provided, and the results of the dexterous ranges are represented in Chapter 8. Stiffness analysis is discussed next.

3.2.4 Stiffness Analysis

According to the literature presented in Chapter 2, there is a demand to improve the accuracy and stiffness of serial robots. Studies have proclaimed the current status and strain placed in the industrial market to expand manufacturing, not to replace conventional CNCs, but rather to assist them and improve operational efficiency. While CNC machines are known for their ability to machine intricate workpieces, they lack the reachability, workspace, repeatability, and flexibility of SKMs. This necessitates the need to shift the robotic paradigm towards improving machining and other high precision manufacturing tasks.

The joint stiffness analysis applied the VJM that was adopted by Dumas *et al.* [107]. The method replaces the joints with virtual springs. The forces/torques applied to the end-effector, and deflection results were used to analyse the stiffness at each test point. The stiffness analysis methodology was to first define stiff points around the robot's workspace, and secondly, to prove that stiffness is also posture dependent.

The experiments were conducted in two phases to validate the importance of the dexterity analysis for stiffness identification. Phase one applied a single pose, with the end-effector perpendicular to the ground. The single posture was considered as “non-dexterous” testing. The second phase, referred to as the “dexterous” tests, applied the IK solution from the dexterity analysis and tested multiple configurations about the same non-dexterous points tested in phase one. The workspace and singularity analyses provided a structured testing platform to perform both non-dexterous and dexterous tests. The testing points were comprised of twenty-five points located equidistantly around the robot base. A further description of the testing point layout is discussed in Chapter 4 and Chapter 8. Next, the tools used to conduct the study are described next.

3.3 Experimental Tools used in the Framework

This section explores the tools that were needed to perform the study (sub-section 3.3.1). A list of all the software packages that were used to simulate and analyse each analysis is also discussed (sub-section 3.3.2).

3.3.1 The Robot, Data Acquisition and Sensors Used in the Study

The Fanuc series M10-iA robot is a cable integrated small handling robot with a maximum payload of 12 kg. The robot can span over a range from 1.4 m to 2 m for several application adaptions. The robot can position any tool with minimum vibration, even during high speeds. For specific applications, high speed and accuracy can drastically improve the overall productivity. Ideally, this small handling robot is more suited towards welding and coating, however, it was the only robot accessible by the university for this research. The robot is equipped with a unique gear drive mechanism with a wrist axis. The hand cable utilities are appropriately integrated into the arm system with the tool mounted on the second link. This layout allows for seamless design and easy utilisation and system setup of the robot [156], as seen in Figure 3-2. The technical data of the Fanuc M10-iA robot can be seen in Appendix A1, Table A.1. along with physical dimensioning shown by the various views in Appendix A, Figure A.1 and Figure A.2 [156]:

Figure 3-2: Fanuc M-10iA Robot [156]

The sensors used in this research sought to provide a cost-effective alternative to deflection measurements used to identify the robot's stiffness. The sensors used in this research include:

1. Three Integrated Electronics Piezo-Electric (IEPE) accelerometers for the linear deflection measurements,
2. A 6-DOF Micro-Electro-Mechanical Systems (MEMS) MPU6050 accelerometer for the rotational deflection measurements,
3. An S-Type load cell for the force measurements.

Most literature used laser tracking devices that are highly expensive and not affordable by most manufacturing firms. The precision of laser trackers is within 100th of a millimetre, and are specialised sensors designed for deflection and displacement measurements. In terms of its deflection measurement capability, these sensors outweigh that of accelerometers, which usually offer a 10th of a millimetre precision after the acceleration to displacement conversion. The National Instruments (NI) data acquisition modules were used to connect and interact with all sensors. The setup of all hardware and software is further discussed in Chapter 8.

3.3.1.1 THE USE OF ACCELEROMETERS FOR DEFLECTION MEASUREMENTS

The velocity and displacement data acquisition history play a fundamental role in the vibration testing of robotic structures. The use of velocity and displacement transducers are usually impractical in robot applications due to requirements in identifying a fixed referential and the exorbitant costs (i.e., laser trackers) [157]. Unlike deflection, acceleration is absolute, implying that the state of acceleration is zero at a fixed point [158]. Nowadays, the compactness and robust construction of accelerometer sensors add simplicity to vibration measurements.

Acceleration offsets are usually classified as errors due to instrumental instability and low sampling rates, restricted resolution of the measuring system, non-linear instrument response, and level of electric noise. Additionally, background noise, depending on the measurement environment, estimation of the real acceleration signal, and data manipulation, impacts the raw acceleration signal [159]. Time integration usually amplifies low-frequency components of the incoming signal, hence, amplifying measurement errors [159]. This is a problem when manipulating the raw acceleration output or changing its form other than what the sensor would normally output under standard conditions. Digital acceleration recordings, unfortunately, contain so-called “baseline offsets”, which are minor steps or distortion in the reference level of motion. As a result, velocity and displacement are flawed with drifts in the signal, producing impractical results [160]. This is partly due to integration constants not being adequately defined.

Much research [161, 162] has been conducted on vibration, noise, and filtering. The problem of measuring displacement from acceleration was analysed by Ribeiro *et al.* [163], in which he developed an algorithm that uses a high-pass digital Finite Impulse Response (FIR) filter to eliminate the bias. Ribeiro *et al.* [163] further added that errors accompanying sampling rate choice are a function of frequency for the displacement measurement. Consequently, the higher the frequency, the higher the bias. The noise reduction technique applied to this research uses a polynomial detrending (least-squares approach), similar to that used by Pan *et al.* [164]. Other studies that concurred with the least-squares approach include Ren *et al.* [165] and Niu *et al.* [166]. Most environmental-related effects that influence the acceleration results are shown in Figure 3-3. These considerations were accounted for in this research, and is further discussed in Chapter 8.

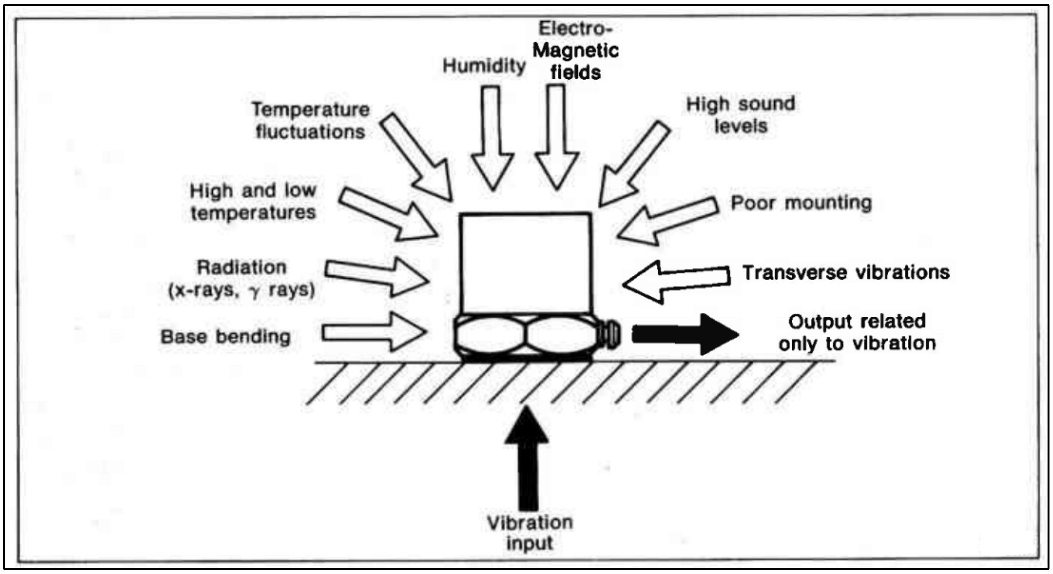

Figure 3-3: Various Types of Accelerometer Noise Interferences [167]

Having discussed the tools used in the framework in the sub-section above, the next sub-section focuses on the software applied in this research.

3.3.2 SOFTWARE

The range of software applied in this research includes MATLAB®, Wolfram Mathematica, RoboDK and LabVIEW. The capability of each software is addressed in this sub-section, including the software that was applied to each analysis.

3.3.2.1 MATLAB®

MATLAB®, the language of technical computing, in recent years, has been extensively used as a software environment throughout the engineering community [168, 169]. The software was only used to formulate the workspace and singularity analysis. Justification of the suitability of this software for this study is provided next. Firstly, it is widely accepted, and has a long history and well-developed computing infrastructure. Secondly, Peter Corke's Robotics toolbox [170] offers a wide range of robotic analyses that can be easily invoked. The analyses provided in the toolbox include forward and inverse kinematic analyses, and Jacobian evaluation, to mention a few. Thirdly, the software has received much recognition in the mechatronics field due to its powerful linear algebra tools, with a wide selection of toolboxes that extends past its basic functionality. Fourthly, the software is well understood with a vast amount of literature, user-manuals, online professional assistances, online-file exchanges, videos and guidelines. Fifth, and lastly, the Graphical User Interface (GUI) is exceptionally user-friendly and includes an easy and interactive environment with wide-ranging computation and visualisation.

3.3.2.2 WOLFRAM MATHEMATICA

Wolfram Mathematica is the world's only fully integrated environment for technical computing. It is a mathematical software package that is broadly used in several engineering disciplines. The software can easily analyse algebraic symbolic and numerical mathematics. The software was easily accessible during most parts of the research and was used to solve the algebraic dexterity and stiffness analyses. The dexterity and stiffness analysis and modelling were analysed using Robotica, which is an executable Wolfram Language Script file, and offers similar functionality to that of Peter Corke's Robotics toolbox.

3.3.2.3 ROBODK

RoboDK is an offline programming and simulation software that features a wide selection of SKMs. The software allows various types of SKMS to be selected, including popular brands, the DOF, and tooling. The Fanuc M10-iA was programmatically controlled. Each axis, including the robot's joint limits and end-effector coordinates, could be controlled. This allowed for the workspace and forward kinematic evaluation to be verified. A variety of machining applications, such as pick-and-place operations, milling, labelling, packaging, etcetera, can be modelled in the software.

3.3.2.4 LABVIEW

LabVIEW is a product of National Instruments (NI) and is a software used for Virtual Instrumentation (VI). The software can imitate physical instruments such as multimetres and oscilloscopes. The software assists with acquiring, analysing, displaying, storing data, and troubleshooting the code. The frontline of the software involves developing a user interface or front panel that consists of dials, controls, and indicators. The front display panel is controlled by a back-end code using VIs and structures. The VI has built-in controls to manage the infographics, such as knobs, pushbuttons, and other input mechanisms. The indicators include LEDs, graphs, and other output displays. Finally, the software can easily communicate with input hardware such as data acquisition, motion control devices, vision, GPIB, VXI, PXI, RS485, and RS232 instruments. The piezotronics accelerometers, MPU6050 accelerometer and load cell, were connected via an NI cDAQ 9174 controlled through a VI in LabVIEW. LabVIEW was used for each test of the joint stiffness analysis.

Some concluding remarks follow next.

3.4 CHAPTER SUMMARY

This chapter presented the conceptual framework of this study. Each analysis was discussed separately under their respective headings. The experimental tools were described, followed by the robot type, data acquisition, and sensors that were available and within budget to effectively conduct the research. This chapter partially addressed Objectives 1, 2 and 3, which sought to *research, establish and develop a dexterous posture identification method that can localise multiple configurations at a user-defined point; research, develop and simulate the workspace and singularities of the Fanuc M10-iA and understand their influence on the dexterity and stiffness analyses;* and, *research, establish and identify a suitable stiffness modelling approach,* respectively.

The next chapter investigates the workspace of the Fanuc M10-iA robot, followed by mathematical formulations of the workspace and the modelling results from MATLAB®.

4. WORKSPACE ANALYSIS

4.1 INTRODUCTION

The previous chapters introduced the study (chapter 1), presented the literature review on robotics and machining (chapter 2), and provided the conceptual framework of the study (chapter 3). Building on this research, this chapter presents the simulative results and analysis of the Fanuc M10-iA robot. The study of the robotic workspace is crucial in understanding the overall reachability of the robot. The Fanuc M10-iA is a popular industrial type manipulator with 6-DOF. A preliminary understanding of the robotic workspace is generally specified in manufacturer guidelines and manuals. However, only an in-plane 2-D workspace is visually shown for the Fanuc robot. As a result, this analysis seeks to provide an analytical approach to the workspace identification using a point cloud technique of the Fanuc's workspace (section 4.2) followed by the MATLAB® simulations (section 4.3). Finally, a brief summary is provided to wrap up the chapter (section 4.4).

4.2 FUNCTIONAL WORKSPACE KINEMATICS AND FORMULATION

To begin the discussion, the concept of "kinematics" will be explained and placed in context. Waldron and Schmiedeler [171] define kinematics as the study of motion, which focuses on the subject without considering the forces that cause the motion. The focus of the kinematic approach deals explicitly with the position, velocity, acceleration, and all higher-order derivatives of the position variables. A review of this approach considered the geometrical and time-based properties of the manipulator's motion. The robot's frames were affixed to specific parts to handle complex manipulator geometries, allowing a clear description to be made between consecutive frames.

The study of kinematics further focuses on frame transformations as the manipulator articulates. The emphasis of this sector is to evaluate the position and corresponding orientation of the manipulator's end-effector relative to the robot's base as a function of the joint variables. The Denavit-Hartenberg (D-H) convention was applied along with other definitions to assist with the necessary coordinate systems [110].

Appendix B.1 presents the methodology to calculate the forward kinematics for the Fanuc M-10iA robot using the standard D-H method. The first step was to determine the D-H parameters, which is shown in Table 4-1 and was developed using the reference coordinate system shown in Figure 4-1, followed by the joint limits of the robot, which is presented in Table 4-2:

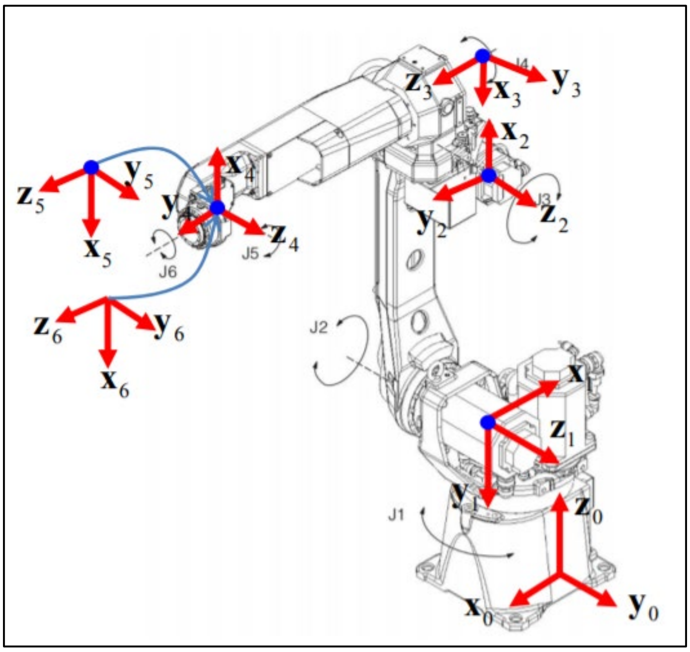

Figure 4-1: Coordinate Reference Frame Attached to a Schematic of the Fanuc M-10iA Robot [156]

Table 4-1: Denavit-Hartenberg Parameters for Fanuc M-10iA Robot

Joint (n)	**Link Length a_i (mm)**	**Link Offset d_i (mm)**	**Twist Angle α_i (radians)**	**Joint Angle θ_i (radians)**
1	-150	450	$\frac{\pi}{2}$	$\pi + q_1$
2	600	0	0	$\frac{\pi}{2} + q_2$
3	-200	0	$\frac{\pi}{2}$	$\pi + q_3$
4	0	640	$\frac{\pi}{2}$	$\pi + q_4$
5	0	0	$\frac{\pi}{2}$	$\pi + q_5$
6	0	0	0	q_6

The second step was to identify the joint limits for the Fanuc Robot, which is shown in Table 4-2

Table 4-2: Joint Limits of Fanuc M-10iA Robot

Joint Limits (n)	**Lower Limit (°)**	**Upper Limit (°)**
1	-360	+340
2	-250	+250
3	-290	+290
4	-380	+380
5	-380	+380
6	-720	+720

The section above defined the term “kinematics” and explained the methodology used to calculate the kinematics for the robot under study – the Fanuc M10-iA robot. The following section simulates the workspace of the Fanuc M10-iA robot used in this study.

4.3 MATLAB® RESULTS

A 3-D visualisation of the Fanuc M-10iA robot workspace (X-Y-Z) with a spherical topology is shown in Figure 4-2, followed by a 2-D top view (X-Y) in Figure 4-3, front view (X-Z) in Figure 4-4, and right view (Y-Z) in Figure 4-5. Other authors who have cited similar workspace topologies include Aggarwal *et al.* [89] and Gudla [172]. The yellow dots bordered by black in the four views represent the points in space that the end-effector of the Fanuc robot can reach according to the joint limits in Table 4-2 (without consideration given to any singularities). The entirety of every reachable point defines the overall workspace. A step size of 10 was used to gain a proper evaluation of the Fanuc-10iA robot’s workspace. This produced n^6 (where n was chosen as 10) joint configurations, each of which were individually substituted into the forward kinematic formulation. In Figure 4-3 (top view), a small cylindrical void can be seen directly in the centre coordinate (X, Y) → (0,0). This void represents the physical volume of the Fanuc robot itself, implying that the end-effector is not able to access this region. From the respective views of the workspace, it is noticed that several voids are visible. In Figure 4-3, the voids are more prominent; an extending spoke-like structure is detected, which was due to a step size of 10 that was applied during the simulation process. It is further noticed that 10 spokes are visible, which is equivalent to the step size. As the number of steps increases, these voids are not visible, but the centre void always remains. However, this drastically increases computational effort and time. According to the Fanuc user manual, the robot has a maximum reachability of 1,412 mm, which can be confirmed by the + x and - x-axis direction in Figure 4-3.

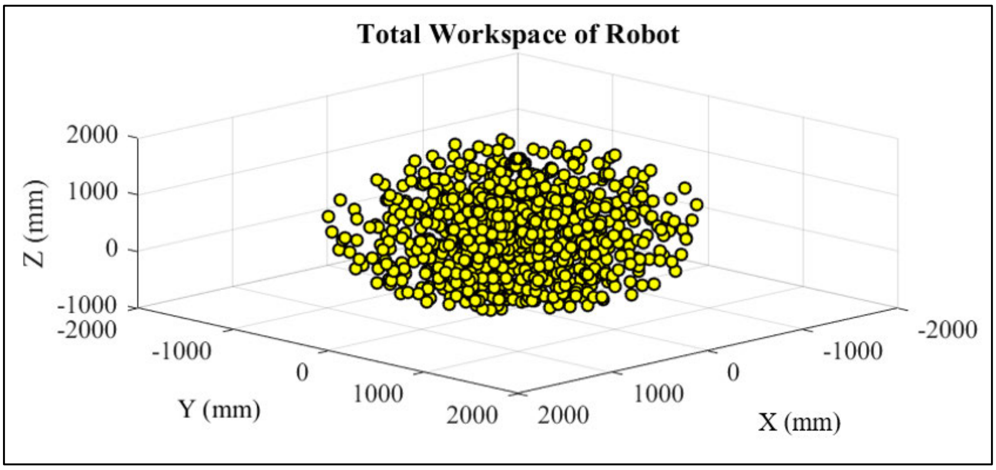

Figure 4-2: Total Workspace of Fanuc M-10iA Robot

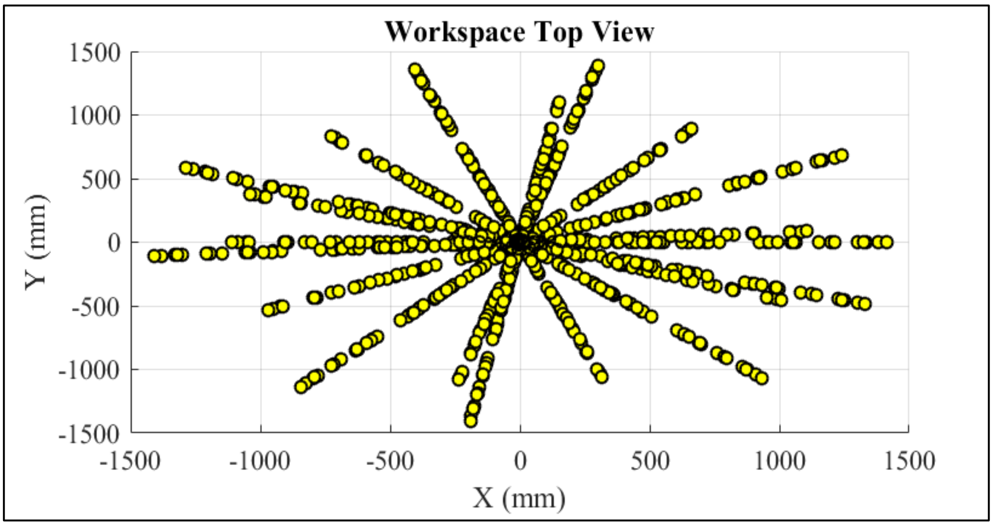

Figure 4-3: Workspace (Top View) of Fanuc M-10iA Robot

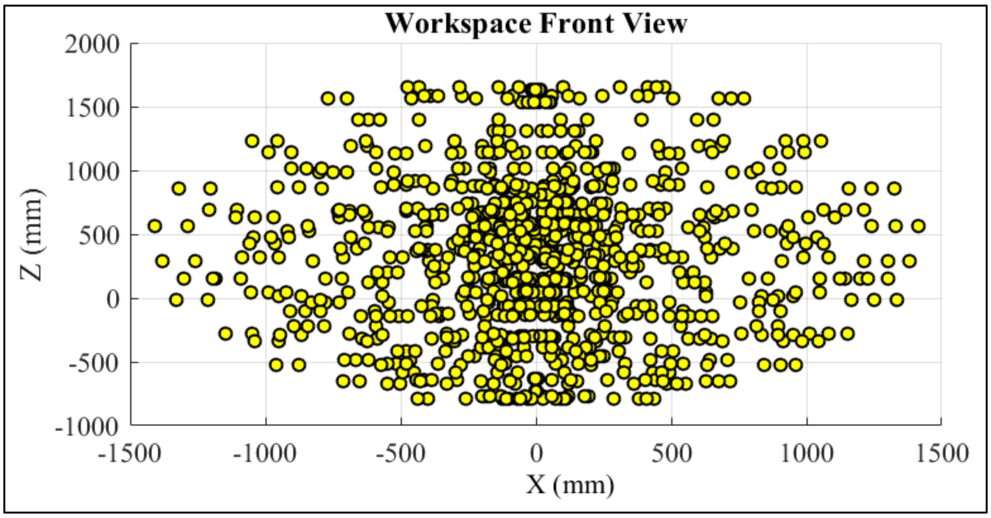

Figure 4-4: Workspace (Front View) of Fanuc M-10iA Robot

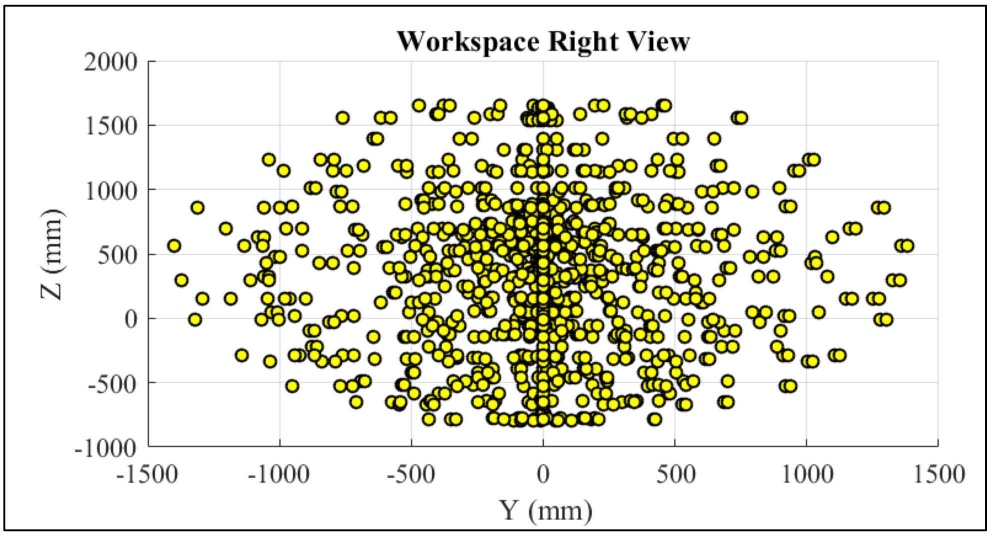

Figure 4-5: Workspace (Right View) of Fanuc M-10iA Robot

Some summary remarks follow next to wrap up the chapter on workspace analysis.

4.4 Chapter Summary

This chapter presented the first analysis to be performed. The workspace design and formulation for the Fanuc M-10iA robot using the analytical point cloud method was chosen as the preferred method. The forward kinematic solution applying the D-H convention was employed to model the workspace using MATLAB®. The results graphically presented the overall 3-D workspace of the robot, followed by the 2-D front, top, and right-side views. A more precise understanding of the Fanuc's workspace was developed from this analysis to develop possible areas/points for the stiffness analysis which will be explained in Chapter 5, and further elaborated on in Chapter 8. The workspace analysis partially addressed Objective 2, which was to *research, develop and simulate the workspace and singularities of the Fanuc M10-iA and understand their influence on the dexterity and stiffness analyses*. Kinematic singularity is the focus of the next chapter.

5. KINEMATIC SINGULARITY

5.1 INTRODUCTION

Having explored workspace analysis in the previous chapter, attention now shifts to the kinematic singularity analysis. This chapter presents the identification and analysis of the kinematic singularities. First, a mathematical investigation is presented to illustrate two singularity types (section 5.2), followed by explaining the MATLAB® results (section 5.3). A description of the point cloud is discussed (section 5.4), which also draws on information from Chapter 4. The chapter then concludes with a brief summary (section 5.5).

5.2 SINGULARITY FORMULATION

This section focuses on singularities. The methodology used to obtain the singularities of the Fanuc M10-iA involved analysing subsets of the Jacobian matrix. The inverse of the Jacobian matrix can mathematically determine singularity conditions. From a mathematical perspective, a singularity arises during a local or instantaneous phenomenon resulting from a rank deficiency of the Jacobian matrix.

The Jacobian matrix, $J(q)$, of a robot concerning its end-effector was determined from the generalised velocity vector (V) by extracting the i^{th} joint velocity vector(s), $\dot{q}$. The joint velocity vectors differ depending on the joint used for each link, such as:

$$\dot{q}_i^{i-1} = \begin{cases} \dot{\theta}_i^{i-1} - \text{for rotational joint i} \\ \dot{P}_i^{i-1} - \text{for translational joint i} \end{cases} \qquad [5\text{-}1]$$

The Jacobian matrix, $J(q)$, is represented by equation [5-2]:

$$V = J(q) \times \dot{q} \qquad [5\text{-}2]$$

The Jacobian matrix can be further subdivided into two parts, a *linear* velocity component, $J_v(q)$, and an *angular* velocity component, $J_\omega(q)$, as depicted by equation [5-3]:

$$J(q) = \begin{bmatrix} J_v \\ J_\omega \end{bmatrix} \qquad [5\text{-}3]$$

The dimension of the Jacobian matrix depends on the number of joints, n, and the dimension of the task space, t. For a robot manipulator with n-DOF, the Jacobian matrix has a dimension of $t \times n$. Due to most general manipulators having to position and orient its end-effector, the task space dimension is usually 6, resulting in an overall Jacobian matrix dimension of $6 \times n$ for any manipulator. As a result, the dimensions of both J_v and J_ω is $3 \times n$.

It is common for singular conditions to arise during the inverse mapping process from Cartesian space to joint space. By changing the subject of the formula in equation [5-2], the joint velocity vector in its joint space was easily mapped to its general velocity vector in Cartesian space, as seen in equation [5-4]:

$$\dot{q} = [J(q)]^{-1} \times V \tag{5-4}$$

The Jacobian matrix is required to be non-singular to obtain a solution from equation [5-4] and be of equal rank to the dimension of the joint and generalised velocity vectors.

According to most literature on robotics, a simplistic method of identifying a kinematic singularity was through the determinant of an $n \times n$ subset, J_n of the Jacobian matrix, where n signifies the number of joints. Mathematically, the inverse Jacobian is represented by equation [5-5]:

$$[J(q)]^{-1} = \frac{C_{ij}}{|J(q)|} \tag{5-5}$$

Where C_{ij} represents the matrix of cofactors (adjugated matrix), and $|J(q)|$ the Jacobian matrix determinant. For a non-invertible singular Jacobian matrix, the matrix determinant is zero, as shown in equation [5-6]:

$$\text{Singular Jacobian: } |J(q)| = 0 \tag{5-6}$$

where:

$$J(q) = \begin{bmatrix} J_{A_{3\times3}} & 0_{3\times3} \\ J_{3\times3} & J_{B_{3\times3}} \end{bmatrix} \tag{5-7}$$

The two upper quadrants represent the linear component $J_v(q)$, and the two lower quadrants represent the angular velocity component $J_\omega(q)$, as shown in equations [5-8] and [5-9].

$$J_V(q) = \begin{bmatrix} J_{V_{11}} & J_{V_{12}} & J_{V_{13}} & J_{V_{14}} & J_{V_{15}} & J_{V_{16}} \\ J_{V_{21}} & J_{V_{22}} & J_{V_{23}} & J_{V_{24}} & J_{V_{25}} & J_{V_{26}} \\ J_{V_{31}} & J_{V_{32}} & J_{V_{33}} & J_{V_{34}} & J_{V_{35}} & J_{V_{36}} \end{bmatrix} \tag{5-8}$$

$$J_{\omega}(q) = \begin{bmatrix} J_{\omega 11} & J_{\omega 12} & J_{\omega 13} & J_{\omega 14} & J_{\omega 15} & J_{\omega 16} \\ J_{\omega 21} & J_{\omega 22} & J_{\omega 23} & J_{\omega 24} & J_{\omega 25} & J_{\omega 26} \\ J_{\omega 31} & J_{\omega 32} & J_{\omega 33} & J_{\omega 34} & J_{\omega 35} & J_{\omega 36} \end{bmatrix} \qquad [5\text{-}9]$$

Both $J_V(q)$ and $J_\omega(q)$ combined form the overall Jacobian matrix for the Fanuc M10-iA robot, as shown by equation [5-10].

$$J(q) = \left[\begin{array}{ccc|ccc} J_{11} & J_{12} & J_{13} & J_{14} & J_{15} & J_{16} \\ J_{21} & J_{22} & J_{23} & J_{24} & J_{25} & J_{26} \\ J_{31} & J_{32} & J_{33} & J_{34} & J_{35} & J_{36} \\ \hline J_{41} & J_{42} & J_{43} & J_{44} & J_{45} & J_{46} \\ J_{51} & J_{52} & J_{53} & J_{54} & J_{55} & J_{56} \\ J_{61} & J_{62} & J_{63} & J_{64} & J_{65} & J_{66} \end{array}\right] \qquad [5\text{-}10]$$

The results of the linear velocity component (equation [5-8]), and angular velocity component (equation [5-9]), combined to give the Jacobian matrix (equation [5-10]), are presented in Appendix C.

5.2.1 Singularity Types Present in Fanuc M10-iA Robot

Most kinematic singularities presented in general wrist partitioned industrial robots are classified according to their joint configurations. This sub-section presents the two common singularity types, namely: *forearm singularity* and *wrist singularity*. These are described in more detail below.

5.2.1.1 Forearm Singularity

In a 6-DOF revolute manipulator, *forearm singularities* arise due to the motion of the forearm and are instigated by the **first three joints** of the robot. The singularities are prevalent at the workspace boundary and occur when the robot arm is fully extended or retracted. Robotic arm singularities can, therefore, represent boundary or internal singularities based on the arm configuration. To obtain the forearm singularities, a subset of the Jacobian ($J_{A_{3\times3}}$) is analysed and can be mathematically represented by equation [5-11]:

$$|J_A| = 0 \qquad [5\text{-}11]$$

From equation [5-7], the submatrix (J_A) is a 3×3 matrix, as shown in equation [5-12]:

$$J_{\mathrm{A}} = \begin{bmatrix} J_{11} & J_{12} & J_{13} \\ J_{21} & J_{22} & J_{23} \\ J_{31} & J_{32} & J_{33} \end{bmatrix} \qquad [5\text{-}12]$$

taking the determinant provides the singularity equation for the Type 1 – forearm singularity for the Fanuc M10-iA robot:

$$|J_A| = (16\mathrm{Cos}[\theta_3] + 5\mathrm{Sin}[\theta_3]) \times (15 + 64\mathrm{Cos}[\theta_2 + \theta_3] + 60\mathrm{Sin}[\theta_2] + 20\mathrm{Sin}[\theta_2 + \theta_3]) = 0 \quad [5\text{-}13]$$

which was further condensed as:

$$|J_A| = \vartheta(\theta_3).\tau(\theta_2, \theta_3) = 0 \quad [5\text{-}14]$$

where a singularity arises when condition 1 or 2 occurs:

$$\text{Condition 1: } \vartheta(\theta_3) \triangleq 0 \quad [5\text{-}15]$$

$$\text{Condition 2: } \tau(\theta_2, \theta_3) \triangleq 0 \quad [5\text{-}16]$$

Due to the complex nature of equations [5-15] and [5-16], the equations were numerically solved in Wolfram Mathematica.

- From $\vartheta(\theta_3)$ – singularities would arise when:

$$q_3 = -2.838 \text{ rad}$$

- From $\tau(\theta_2, \theta_3)$ – singularities would arise when:

$$q_2 = -1.571 \text{ rad} \approx -\frac{\pi}{2} \text{ rad}$$

$$q_3 = -1.268 \text{ rad}$$

5.2.1.2 WRIST SINGULARITY

In a 6-DOF revolute manipulator, *wrist singularities* arise due to the motion of the wrist and are instigated by the **last three joints** of the robot. Singularities of this type occur when two of the three wrist joints become collinear. As a result, equal and opposite rotational movements about their axis cancel out all possible end-effector orientations. These singularities can only be left out from the joint space, provided that reasonable restrictions are placed on the joint variables. To obtain the wrist singularities for the Fanuc M10-iA, a subset of the Jacobian ($J_{B_{3\times 3}}$) matrix was analysed, and is mathematically represented by equation [5-17] as follows:

$$|J_B| = 0 \qquad [5\text{-}17]$$

Like before, from equation [5-7], the submatrix (J_B) is a 3×3 matrix, as shown in equation [5-18]:

$$J_{\mathrm{B}} = \begin{bmatrix} J_{44} & J_{45} & J_{46} \\ J_{54} & J_{55} & J_{56} \\ J_{64} & J_{65} & J_{66} \end{bmatrix} \qquad [5\text{-}18]$$

taking the determinant provides the equation for the Type 2 – wrist singularity for the Fanuc M10-iA robot:

$$|J_B| = -\sin(q_5) = 0 \qquad [5\text{-}19]$$

where singularities arise when:

$$\theta_5 = [-2\pi, -\pi, , 0,\ \pi,\ 2\pi]\ \text{rad}$$

Since all angles lie with the robot's joint space (see Table 4-2 for θ_5), as θ_5 approaches these angles, a singular condition arises.

This section focused on kinematic singularities, providing a description of the Fanuc M10-iA robot singularity types – *forearm singularity* and *wrist singularity.* Building on these insights, the next section simulates the singularity space of the Fanuc M10-iA robot used in this study.

5.3 MATLAB® RESULTS

A 3-D visualisation (X, Y and Z) axes of the singularity space of the Fanuc M10-iA robot is presented in Figure 5-1, followed by a 2-D top view (X-Y) in Figure 5-2, front view (X-Z) in Figure 5-3, and right view (Y-Z) in Figure 5-4. These red dots signify points in the workspace that are not reachable by the robot's end-effector. Similar to the workspace results, a step size of 10 was used to simulate the singularity space.

From the literature presented in Section 2.7, both Type 1 and 2 singularities can be noticed. Type 1 singularities are clearly shown in Figure 5-2, Figure 5-3, and Figure 5-4, at the outer boundary of the end-effector. These singularities were represented by equation [5-13].

Singularities of Type 2 can be noticed further within the workspace (internal). These types of singularities occur when two or three end joints become collinear. These singularities were represented by equation [5-19]. In Figure 5-2 and Figure 5-3, an oval-like structure is noticed in the centre. This space represents the void presented in the workspace results in Chapter 4. The void characterises the space occupied by the volume of the robot itself, and as a result, the end-effector would not be able to reach anywhere within that region. The open spaces between each point (inner and outer voids) are due to the step size of 10 that was chosen. Increasing the step size covers all voids but at a higher computational expense.

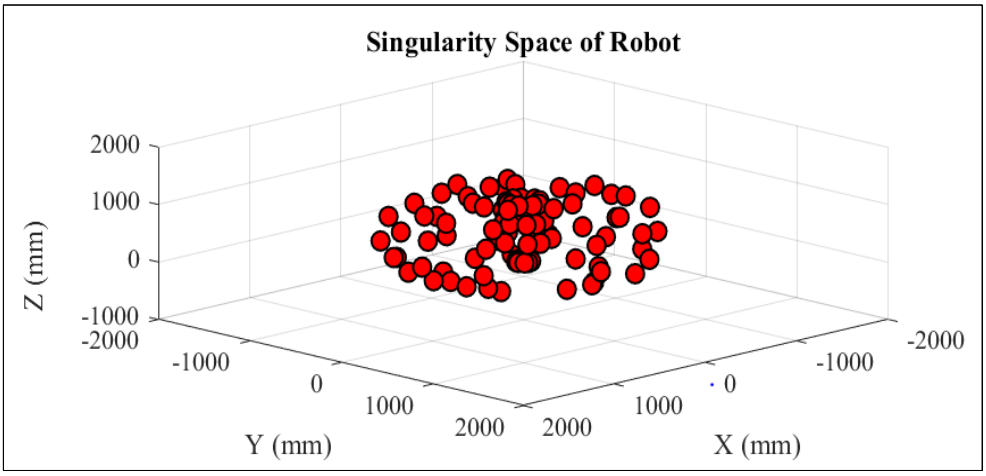

Figure 5-1: Singularity Space of Fanuc M10-iA Robot

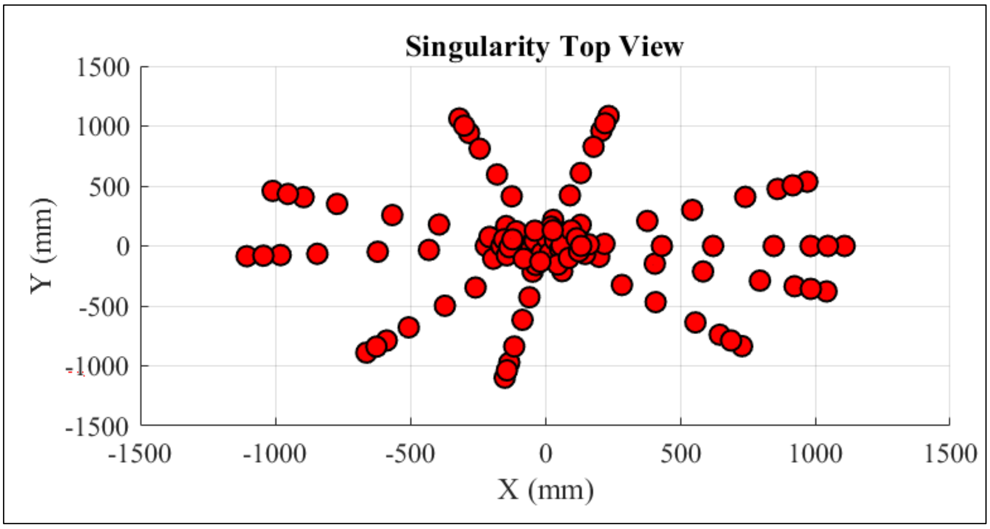

Figure 5-2: Singularity of Fanuc M10-iA Robot (Top View)

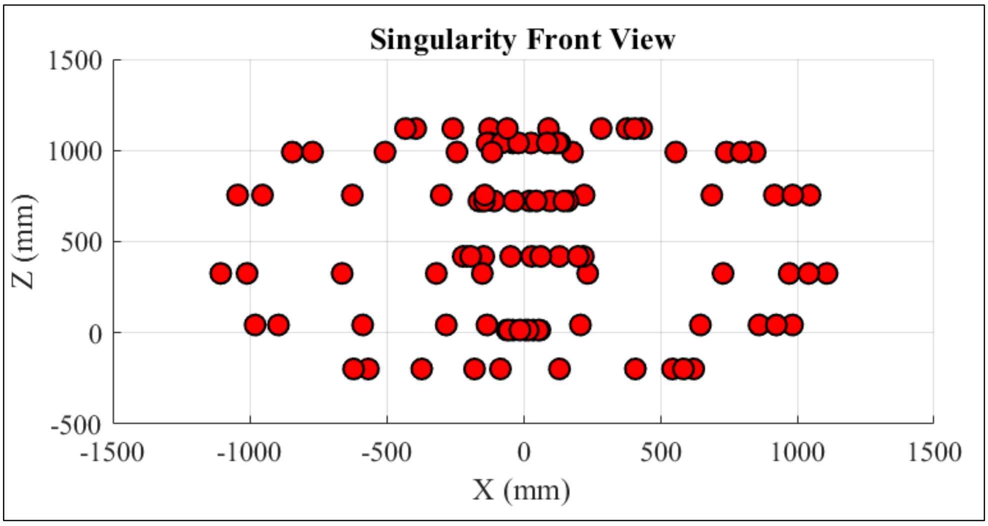

Figure 5-3: Singularity of Fanuc M10-iA Robot (Front View)

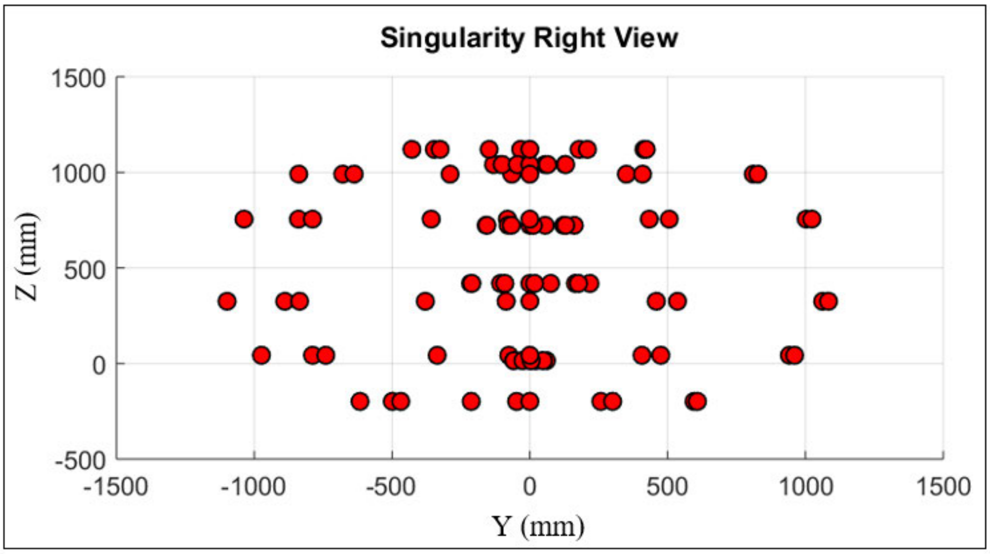

Figure 5-4: Singularity of Fanuc M10-iA Robot (Right View)

Below is the modelled functional workspace that shows a combination of the workspace and kinematic singularities of the Fanuc M10-iA robot. Similar to the kinematic singularity layout presented above, in Figure 5-5, a 3-D (X, Y and Z) axes functional view of the Fanuc robot is presented. The yellow dots signify the reachable workspace with the kinematic singularities (red dots). Similarly, Figure 5-6, Figure 5-7 and Figure 5-8 displays the top-view (X, Y) axes, front-view (Z, X) axes, and right-view (Z, Y) axes, respectively.

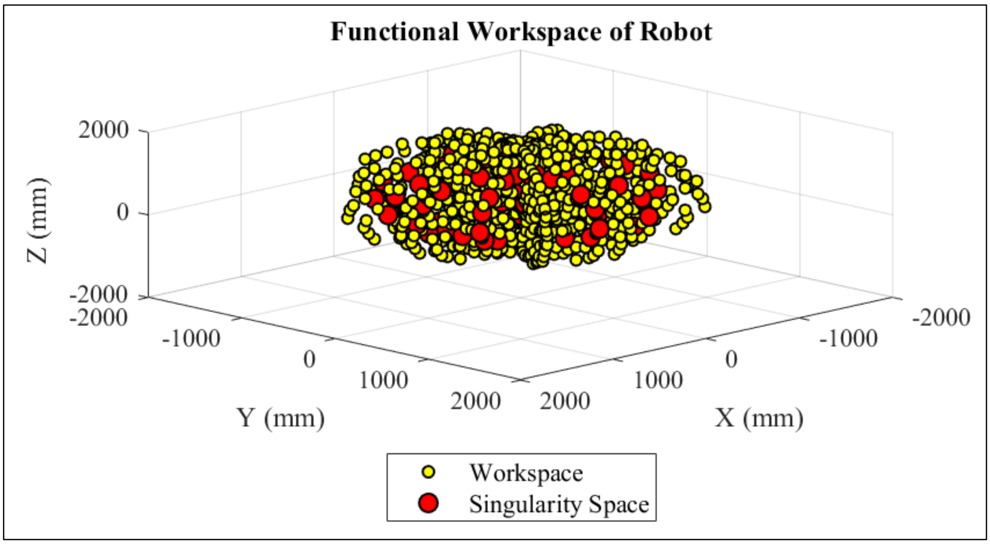

Figure 5-5: Total Functional Workspace of Fanuc M10-iA Robot

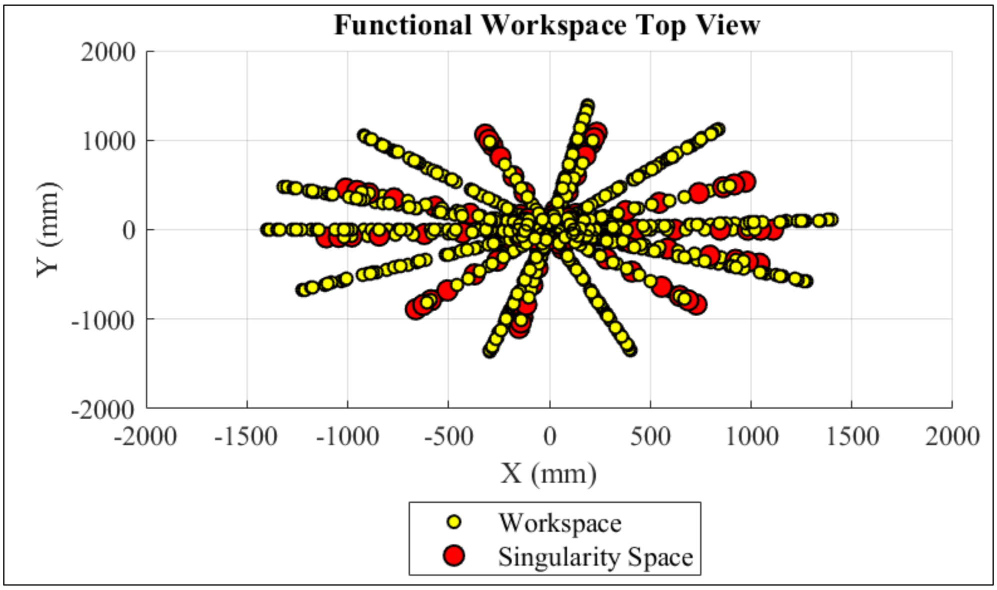

Figure 5-6: Functional Workspace of Fanuc M10-iA Robot (Top View)

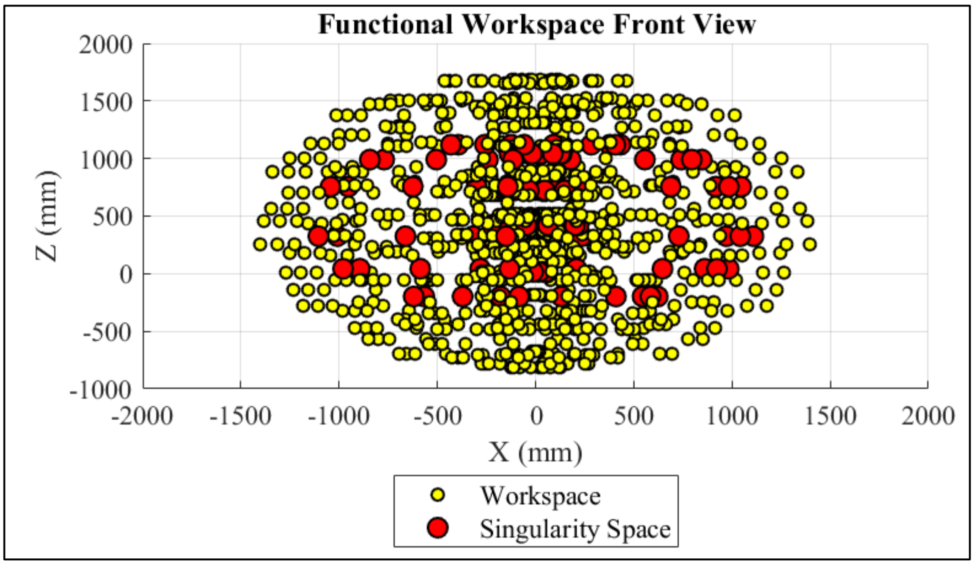

Figure 5-7: Functional Workspace of Fanuc M10-iA Robot (Front View)

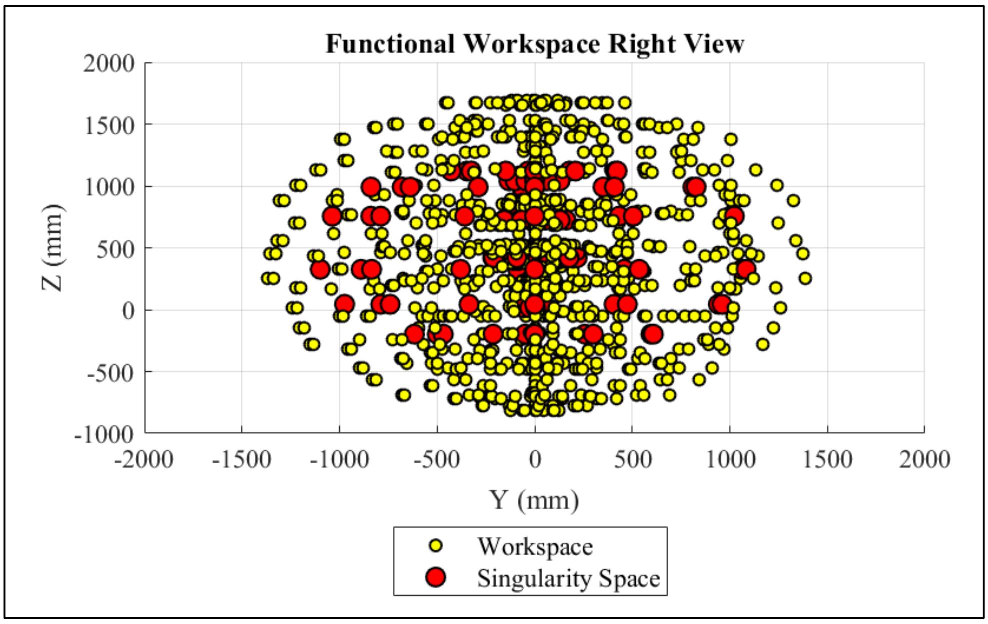

Figure 5-8: Functional Workspace of Fanuc M10-iA Robot (Right View)

The point cloud development to test the dexterous posture identification and stiffness analyses is the focus of the next section.

5.4 Point Cloud Development

The workspace top view in Figure 4-3 and top view functional workspace in Figure 5-6 aided in developing a structured point cloud to test the dexterous posture identification and stiffness analyses. Due to the general ovular shape of the workspace, a cylindrical coordinate point cloud system sought to provide a structured testing ground. Based on the results in Figure 4-3, Figure 4-5, Figure 5-7, and Figure 5-8, the point cloud was structured to cater for multiple equidistant radial distances. At each radial distance (r), equiangular points (θ) at multiple heights (z) were developed. Additionally, from the right view topology of the Fanuc's functional workspace in Figure 5-8, the collection of red and yellow points at (0,0) represents the robot's volume, as previously mentioned. Consequently, the (0,0) line marked the reference line. In this regard, the first radial distance was placed at a radial distance of 400 mm (r_1) from the reference line. To evaluate the stiffness as the end-effector moves away from the base, several radial distances were required; therefore, from the first radial distance at r_1 = 400 mm, 4 consecutive radial distances were constructed at r_2 = 600, r_3 = 800, r_4 = 1,000, and r_5 = 1,200 mm. In the same manner, various heights (z) were required. For convenience, the x-axis in Figure 5-7 represented the ground. Consequently, from Figure 4-4, Figure 4-5, Figure 5-7, and Figure 5-8, the first point was placed at z_1 = 100 mm, then at z_2 = 300 mm, z_3 = 500 mm, z_4 = 700 mm, and a maximum height of z_5 = 900 mm was chosen. Additional points at each radius (r) and height (z) were further added at a constant $\theta = 30°$. This created a 5×5 layered network of points at each radial distance. This cylindrical coordinate point cloud will be discussed further in Chapter 8. Some concluding remarks are provided next.

5.5 CHAPTER SUMMARY

This chapter presented the singularities for the Fanuc M10-iA robot, which were calculated by finding the determinant of a subset of the Jacobian matrix. The singularity space and reachable workspace were analytically simulated using MATLAB®. The functional workspace portrayed a clearer understanding of all singular configurations of the Fanuc robot. The forearm and wrist singularities were appropriately identified, and the results were used to determine appropriate testing points for both the non-dexterous and dexterous tests. The singularity analysis partially addressed Objective 2 and 6 of this study, which was to *research, develop and simulate the workspace and singularities of the Fanuc M10-iA and understand their influence on the dexterity and stiffness analyses,* and *research, design, construct and implement a suitable testing ground to test the workspace, singularity, dexterity, and stiffness model.* The dexterity analysis is provided next.

6. DEXTERITY ANALYSIS

6.1 INTRODUCTION

Having focused on workspace analysis (chapter 4) and kinematic singularities (chapter 5), this chapter investigates and identifies the dexterity analysis. To this end, the dexterity technique applied an IK approach. The purpose of this analysis was to identify multiple configurations at a point within the robot's workspace. These configurations about a point developed a dexterous zone that was formed by the intersection of two workspaces. The stiffness of these configurations was tested using the VJM approach, which is explained in more detail in Chapter 7. Apart from improving the stiffness, the dexterity analysis simplified the mathematical stiffness approach. After providing a brief introduction (section 6.1), the chapter explores the IK formulation (section 6.2). This section focuses on identifying the Euler angles defined by β and α angles, which is followed by a brief summary that concludes the chapter (section 6.3).

6.2 DEXTERITY FORMULATION

The dexterity analysis applied in this research was based on the approach implemented by Mondragon [106]. The Inverse Kinematic (IK) solution focused on two fundamental concepts: the clear case was developing the required coordinate position within the robot's workspace, and the second case was the correct orientation. The 3×3 orientation matrix entailed solving the IK problem in terms of Euler angles (α, β, γ). The concept that encapsulates defining all conceivable α, β, γ orientations of the end-effector at a point is referred to as "dexterity analysis", which is the focus of this section.

To determine admissible orientations of the end-effector at a user-defined point, tracing a sphere (service sphere) with a radius equal to the length of the manipulator's last link around the point was required. The intersection of the Second-to-Last-Joint (SLJ) workspace with the service sphere outlined the maximum and minimum α and β orientations. This geometrically defined the intersection of the SLJ workspace with the service sphere as an ellipsoid, as seen in Figure 6-1. A relationship between α and β exists. As β angles were identified away from the ellipse centre line, the possibilities of α values were narrowed. Consequently, if a maximum or minimum value was allocated to β, then the α values were constrained to a single value. It was confirmed that γ values are unaffected when dealing with a 6-DOF serial arm. Such validation is the focus of the next sub-section. Attention now shifts to the γ (sub-section 6.2.1), β (sub-section 6.2.2), and α (sub-section 6.2.3) orientations.

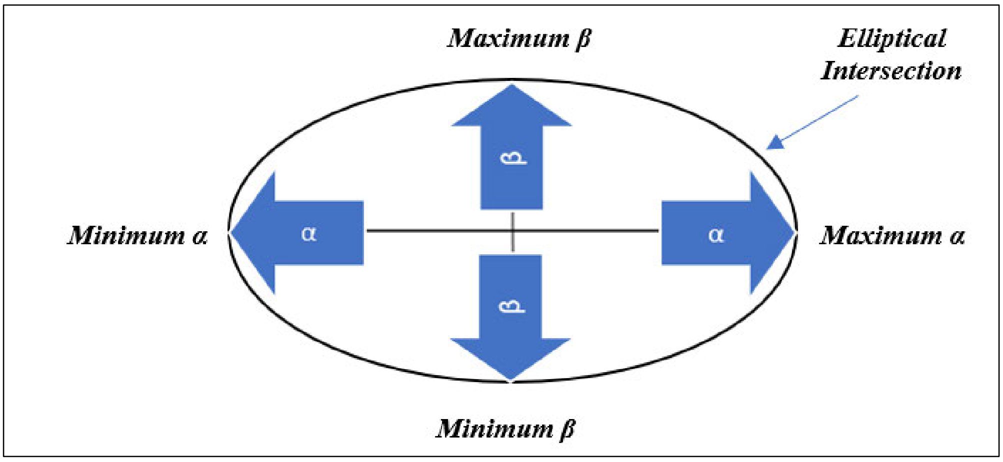

Figure 6-1: Alpha and Beta Directions

6.2.1 CALCULATING GAMMA (γ) ORIENTATION

The end-effector orientation matrix is of size 3×3 and was computed using the Euler angles convention (Z-X-Z) [173]. The orientation matrix for any serial manipulator can be computed as:

$$\begin{bmatrix} r_{11} & r_{12} & r_{13} \\ r_{21} & r_{22} & r_{23} \\ r_{31} & r_{32} & r_{33} \end{bmatrix} = \begin{bmatrix} cos_\alpha cos_\beta cos_\gamma - sin_\alpha sin_\gamma & -cos_\alpha cos_\beta sin_\gamma - sin_\alpha cos_\gamma & cos_\alpha sin_\beta \\ cos_\alpha cos_\beta cos_\gamma - cos_\alpha sin_\gamma & -sin_\alpha cos_\beta sin_\gamma + cos_\alpha cos_\gamma & sin_\alpha sin_\beta \\ -sin_\beta cos_\gamma & sin_\beta sin_\gamma & cos_\beta \end{bmatrix} \quad [6\text{-}1]$$

When examining the equations to calculate the joint angles of θ_1 to θ_5 using the IK method, the vector considered was the end-effector z orientation $[r_{13} \quad r_{23} \quad r_{33}]$. This vector could only be altered by varying α and β and not γ. The only joint which (γ) affected, was joint 6 – the end-effector. Since joint 6 has a range higher than $\pm 180°$, between $\pm 720°$, γ can have any value. Gamma is usually modified during an obstacle avoidance test when the end-effector approaches an object. For this analysis, all tests within dexterous zones, γ was kept constant at 0° since obstacle avoidance was not considered and fell out of the scope of this research.

6.2.2 BETA (β) ORIENTATIONS

The SLJ workspace contained an interior and exterior boundary. As a result, this led to multiple intersections with the service sphere. In conjunction with the above single intersection discussed, this created three different scenarios for the end-effector orientation depending on the position of the service sphere. These were:

1. End-effector facing outside – The service sphere intersects the exterior boundary of the SLJ, shown in Figure 6-2a;

2. Ring Effect – The service sphere intersects the exterior and interior boundary of the SLJ, shown in Figure 6-2b; and
3. End-effector facing inside – The service sphere intersects the interior boundary of the SLJ, shown in Figure 6-2c.

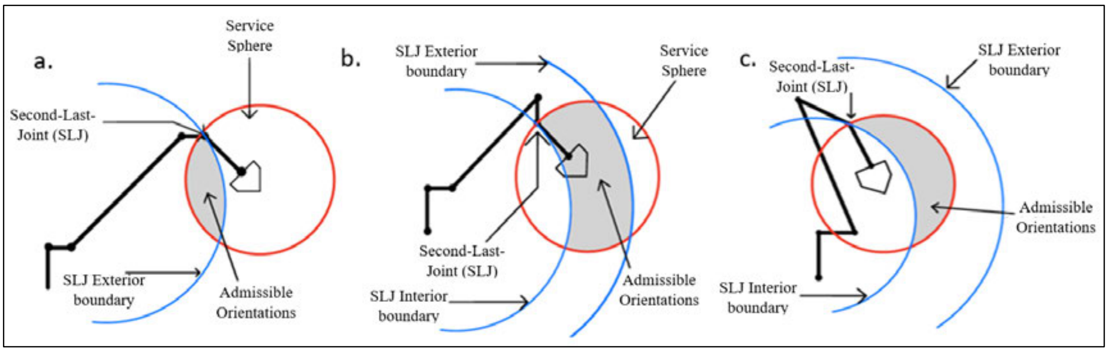

Figure 6-2: a) End-effector Facing Outside, b) Ring Effect, and c) End-effector Facing Outside

Note that only cases where the outer intersection was formed were analysed in this research. In other words: 1) only end-effector facing outside, and 2) ring effect. The concept of the "inner and outer intersection" of the workspace boundary as well as α and β directions are displayed in Figure 6-3 below.

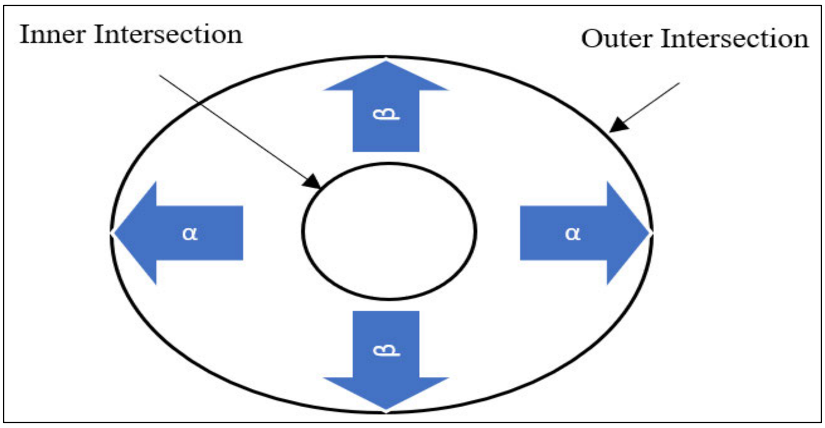

Figure 6-3: Inner and Outer Intersection

6.2.2.1 BETA FORMULATION – OUTER INTERSECTION

An adjoining line between the coordinate position of the end-effector and the coordinate position of joint 2 was traced and allowed for a nominal β value to be determined. This value characterised the end-effector's inclination when the manipulator passes through the centre of the elliptical intersection. The expression used to calculate the nominal β angle is shown by equation [6-2] below.

$$\beta' = atan\left(\frac{p_z - z_2}{\sqrt{(p_x - x_2)^2 + (p_y - y_2)^2}}\right) \quad [6\text{-}2]$$

The nominal β angle equally separated the maximum and minimum β angles. Figure 6-4 shows the path of movement required for the manipulator to attain a point with maximum β inclination. This allowed a triangle to be formed that connected the end-effector, the SLJ with maximum β inclination and joint 2 as shown in Figure 6-4. All dimensional lengths for the triangle were known, which enabled the internal angles to be determined. Lastly, an angle δ, formed between link 5 and the nominal distance ρ, allowed for the β orientation of the end-effector with respect to the global coordinate system to be calculated. The expressions used to calculate the minimum and maximum β orientations are as follows:

$$\beta_{max/min} = \beta' \pm \delta \quad [6\text{-}3]$$

where:

$$\delta = acos\left(\frac{(l_4 + l_5)^2 + \rho^2 - (l_3)^2}{2(l_4 + l_5)\rho}\right) \quad [6\text{-}4]$$

where:

$$\rho = \sqrt{(px - x_2)^2 + (py - y_2)^2 + (pz - z_2)^2} \quad [6\text{-}5]$$

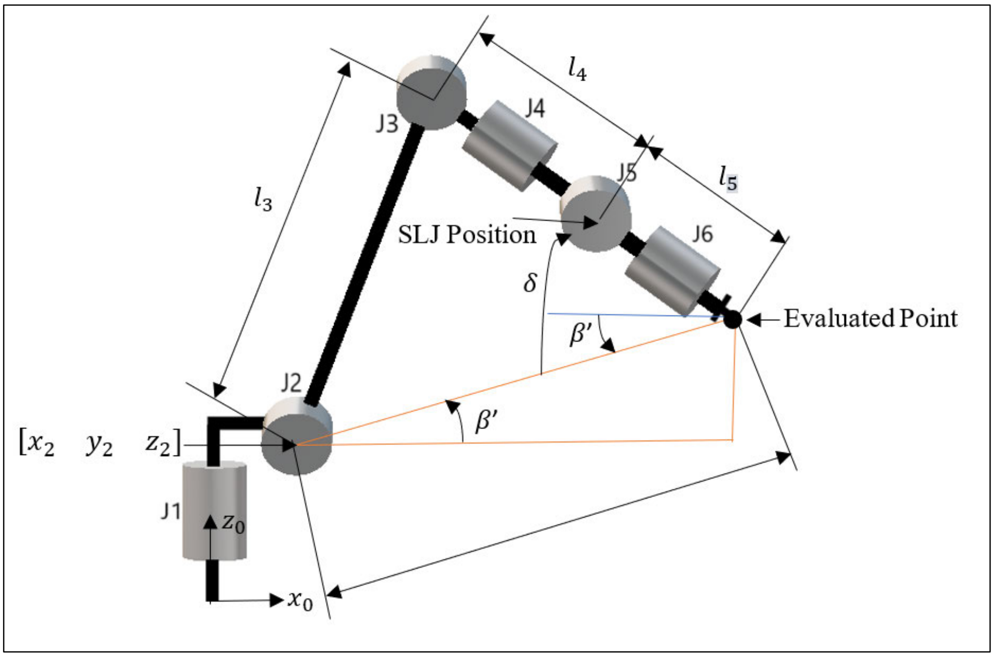

Figure 6-4: Fanuc Robot Configuration with Maximum β Orientation

6.2.3 ALPHA (α) ORIENTATION

As mentioned previously, the β and α regions are strongly connected. After the β formulation was determined from an acceptable range of values, the α formulation followed. The acceptable range for α angles varied for every β angle calculated for a specific end-effector coordinate position. Similar to the β analysis, the existence of two boundaries developed by the SLJ workspace created two different scenarios:

The analysis for the α formulation followed a similar approach to the β formulation. However, it varied in that the maximum and minimum values were derived from the x-y coordinate position (horizontal displacement). Likewise, the α orientation also depended on the inner/outer intersection. This is described in more detail below.

6.2.3.1 ALPHA ORIENTATION– OUTER INTERSECTION

To unpack this further, a nominal α angle was needed to determine the admissible range of values for the α orientation. This value represented the end-effector directed towards the centre of the horizontal line (x-y coordinate) positioned at a corresponding β inclination. As the end-effector pointed towards the centre of α values in the elliptical intersection, the robot lay in a common plane. The nominal α angle is determined by:

$$\alpha' = atan2(p_y, p_x) \qquad [6\text{-}6]$$

Furthermore, the maximum and minimum angular displacements for the α orientation was equal to the nominal α angle. To calculate this angular displacement, and considering that the length of link 3 was fixed, only the outer elliptical intersection was reachable. For the entire range of α orientation, the height of the SLJ remained constant and aided in determining the inclination, as shown in Figure 6-5. The end-effector coordinate position and β orientation was needed to determine the z-coordinate element of the SLJ. The equation governing the height of the SLJ is:

$$h_{SLJ} = p_z - (l_4 + l_5)\sin(\beta) \qquad [6\text{-}7]$$

The inclination of link 3 was calculated as:

$$\delta = atan\left(\frac{h_{SLJ} - l_1}{l_3}\right) \qquad [6\text{-}8]$$

Using the angles mentioned above and projecting the links in the x-y plane, a triangle was formed, as shown in Figure 6-6. Projecting links 2 and 3 formed one side of the triangle, while links 4 and 5 represented the other, and the distance between the robot base (global coordinate position) and end-effector over the x-y plane completed the triangle. The interior angle σ, formed by the nominal position line ρ and links 3 and 4, denote the deviation of the α orientation concerning the nominal position shown in Figure 6-6. Finally, adding the σ angle, the following equation identified the α′ nominal angle, and the minimum and maximum α angles:

$$\alpha_{max/min} = \alpha' \pm \sigma \qquad [6\text{-}9]$$

where:

$$\sigma = acos\left(\frac{\rho^2 + \left((l_4 + l_5)\, cos(\beta)\right)^2 - \left((l_3)\, cos(\delta) + l_2\right)^2}{2\rho\left((l_4 + l_5)\, cos(\beta)\right)}\right) \qquad [6\text{-}10]$$

where:

$$\rho = \sqrt{p_x^2 + p_y^2} \qquad [6\text{-}11]$$

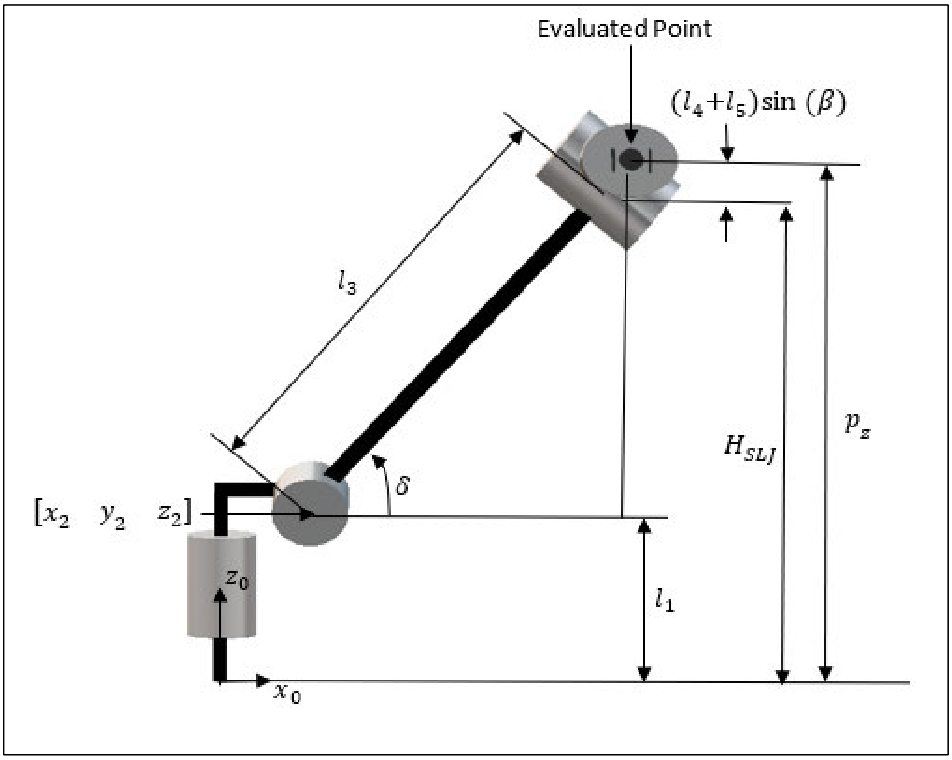

Figure 6-5: Robot Configuration with Maximum α Orientation – Side View (x-z plane)

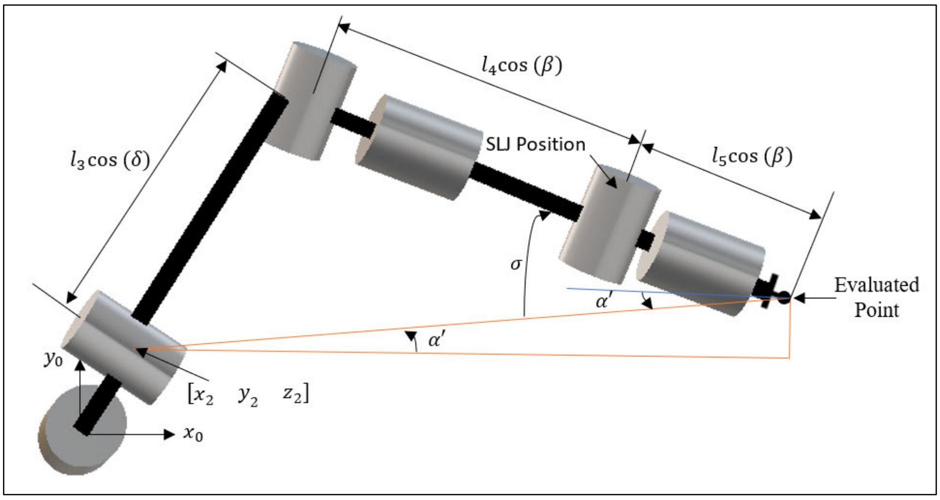

Figure 6-6: Robot Configuration with Maximum α Orientation – Top View (x-y plane)

A few concluding comments follow next, summarising the main points of the chapter.

6.3 CHAPTER SUMMARY

This section analysed the IK technique that was used to define the dexterity analysis applied in this research. The method was able to localise multiple configurations at a point within the robot's reachable workspace, thus meeting Objective 1, which was to *research, establish and develop a dexterous posture identification method that can localise multiple configurations at a user-defined point*. The benefit of this technique is substantiated in the Experimental Analysis and Results section of Chapter 8. The need for such analysis was detailed in Chapters 2 and 3 and will further be highlighted during the stiffness identification technique presented in the next chapter.

7. STIFFNESS MODELLING AND IDENTIFICATION

7.1 INTRODUCTION

The previous three chapters focused on workspace analysis (chapter 4), kinematic singularity (chapter 5), and dexterity analysis (chapter 6). Building on this research and that of the earlier chapters, this chapter presents the stiffness modelling approach for SKMs using the VJM technique. The chapter sets out to define the Joint Stiffness modelling approach using the VJM (section 7.2), partially addressing Objective 3. The procedure for determining the stiffness (section 7.3) and link deflections (section 7.4) is detailed to provide a procedural guide for roboticists and manufacturers to follow, which also partially addresses Objective 3 and fully addresses Objective 4. Lastly, the chapter closes with a brief summary of the VJM technique (section 7.5).

7.2 JOINT STIFFNESS MODELLING

This section presents the process of calculating the estimated joint stiffness values using the VJM technique. The procedure applies to any n-DOF revolute serial kinematic robot. The method is based on Hooke's Law, by replacing the revolute robot joints with virtual springs, as shown in Figure 7-1 below:

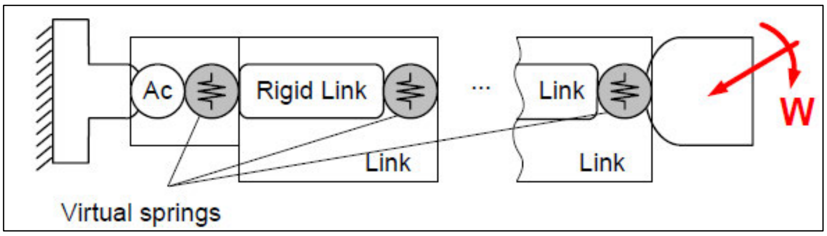

Figure 7-1: Virtual Joint Method (VJM) Model

For this research, an algebraic analysis was considered to evaluate the model. To understand the fundamental derivation of the VJM procedure, consider equations [7-1]–[7-3]. Equation [7-1] was derived from the manipulator's geometrical model. Equation [7-2] defines the static equilibrium condition under the assumption that the load is not necessary, and equation [7-3] describes the linear elasticity relation using Hooke's Law.

$$\delta t = J.\delta\theta \quad [7\text{-}1]$$

$$\tau = J^T.\omega \quad [7\text{-}2]$$

$$\tau_\theta = K_\theta.\delta\theta \quad [7\text{-}3]$$

To explain further, δt, equation [7-4], denotes the 6-D displacement and orientation vector of the end-effector, and ω, equation [7-5], is the measured 6-D wrench vector of forces and moments.

$$\delta t = [x \quad y \quad z \quad r_\alpha \quad r_\beta \quad r_\gamma] \qquad [7\text{-}4]$$

$$\omega = [F_x \quad F_y \quad F_z \quad M_x \quad M_y \quad M_z] \qquad [7\text{-}5]$$

J is the $6 \times n$ matrix, where n represents the number of joints. Furthermore, $\delta\theta$ characterises the deflections in the virtual joint coordinate space due to the loadings ω, while τ signifies the 6-D actuated torques in the elastic joints. Finally, K_{θ_i} reflects a diagonal $6 \times n$ matrix of the ith joint stiffness value. The preliminary equations – [7-1], [7-2], and [7-3] – denote transitional equations to reach the Cartesian stiffness matrix K_C. The K_C matrix describes the relationship between the translational and rotational displacements of the end-effector in Cartesian space and the static forces and torques responsible for the transition. This is defined in equation [7-6] as follows:

$$\omega = K_C . \delta t \qquad [7\text{-}6]$$

Differentiating the actuated torques shown in equation [7-3] with respect to the 6-D joint coordinates yields the robot Cartesian stiffness matrix K_C as shown:

$$K_C = J^{-T}(K_\theta - K_X)J^{-1} \qquad [7\text{-}7]$$

Defining the dexterous zones in Chapter 6 and solving equation [7-7], the Cartesian model is drastically simplified since the non-linear Complementary stiffness matrix (K_X) is negligible with regards to K_θ. The simplified Cartesian stiffness matrix, shown in equation [7-8], now yields:

$$K_C \approx J^{-T} K_\theta J^{-1} \qquad [7\text{-}8]$$

After algebraic manipulation of equations [7-1]–[7-3] and [7-6], a linear model detailing the end-effector deflection due to the applied wrench ω is presented in equation [7-9]. Equation [7-9] constituted the fundamental basis of the VJM technique. The calculated deflection matrix is shown in equation [7-9] and is dependent on the number of DOF of the robot. The greater n is, the higher the computational effort and expense. The joint compliance variable ${K_\theta}^{-1}$ represents the inverse of the joint stiffness matrix. The compliance of a robot characterises its degree of flexibility.

$$\delta t = J_\theta \cdot K_\theta^{-1} \cdot J_\theta^{T} \cdot \omega \quad [7\text{-}9]$$

The compliance matrix, K_θ^{-1} in equation [7-9] is represented via matrix x, in equation [7-10], and is defined as:

$$K_\theta^{-1} = x = \left[\frac{1}{K_{\theta_1}}\ \frac{1}{K_{\theta_2}}\ \frac{1}{K_{\theta_3}}\ \cdots\ \frac{1}{K_{\theta_n}}\right]^{T} \quad [7\text{-}10]$$

Equation [7-9] can be expanded as shown in equation [7-11], where x_j is the jth component of matrix x for an n-DOF system:

$$\delta t = \begin{bmatrix} \sum_{j=1}^{n}\left(x_j \cdot J_{1j}\sum_{i=1}^{n} J_{ij}\cdot\omega_i\right) \\ \vdots \\ \sum_{j=1}^{n}\left(x_j \cdot J_{6j}\sum_{i=1}^{n} J_{ij}\cdot\omega_i\right) \end{bmatrix} \quad [7\text{-}11]$$

To establish a linear model to estimate the joint stiffness values K_θ, matrix x needs to be isolated from δt. By separating x, δt can be transformed into matrix A, shown in equation [7-12]. The transformation process of δt to matrix A describes the forces in the joint space based on the forces applied in the end-effector space (ω). In simpler terms, the Jacobian J in matrix A defines the connection between the applied end-effector forces and the resultant torques required by the robot's joints to sustain these forces. The size of the matrix is $n \times n$, where n denotes the number of DOF. The product of x and A evaluates back to δt in equation [7-11].

$$A = \begin{bmatrix} J_{11}\sum_{i=1}^{n} J_{i1}\cdot\omega_i & \cdots & J_{16}\sum_{i=1}^{n} J_{in}\cdot\omega_i \\ \vdots & \ddots & \vdots \\ J_{n1}\sum_{i=1}^{n} J_{i1}\cdot\omega_i & \cdots & J_{n6}\sum_{i=1}^{n} J_{in}\cdot\omega_i \end{bmatrix} \quad [7\text{-}12]$$

The product of matrix A and the joint compliances can be linearly represented in terms of the measured end-effector displacement, δt, as follows:

$$Ax = \delta t \quad [7\text{-}13]$$

For improved accuracy of the VJM technique, it is necessary to perform multiple tests. If i tests are performed, let B_i represent the A matrix and c_i the δt matrix such that equation [7-13] now becomes:

$$Bx = c \qquad [7\text{-}14]$$

where:

$$B = \begin{bmatrix} B_1 \\ \vdots \\ B_i \\ \vdots \\ B_n \end{bmatrix} \qquad [7\text{-}15]$$

$$c = \begin{bmatrix} c_1 \\ \vdots \\ c_i \\ \vdots \\ c_n \end{bmatrix} \qquad [7\text{-}16]$$

When $(n > 1)$ – the linear-equation system shown by equation [7-14] – becomes overdetermined, it implies that matrices B and c become rectangular. Matrices of this nature can be solved using the *Moore-Penrose Pseudo Inverse* method shown by equation [7-17]:

$$x_0 = (B^T B)^{-1} B^T c \qquad [7\text{-}17]$$

Therefore, many tests can be achieved using this approach to evaluate the joint stiffness values. The end-effector deflections and rotations at each pose can be analysed through the Homogenous Transformation Matrix (HTM). The HTM matrix is developed using the D-H convention by assigning frames to the links of a spatial kinematic chain. This matrix is used to identify the position and orientation of the end-effector for an n-DOF robot. Each pose has a unique HTM. To mathematically evaluate the deflections and rotations of the end-effector, ε_{n} defines the pose before the applied wrench and $\varepsilon_{\mathrm{n}}{}'$ defines the pose after the applied wrench. The difference in the HTM between the two frames represents the deflection of the robot.

Let ${}^0T_6$ and ${}^0T_6{}'$ define the HTM from the base frame (ε_0 to ε_{n}) and from (ε_0 to $\varepsilon_{\mathrm{n}}{}'$), respectively. The two HTM's are obtained via the recorded end-effector coordinates before and after the applied wrench, and take the form:

$$^{0}T_6 = \begin{bmatrix} R_n & p_n \\ 0_n^T & 1 \end{bmatrix} \quad [7\text{-}18]$$

$$^{0}T_6' = \begin{bmatrix} R_n' & p_n' \\ 0_n^T & 1 \end{bmatrix} \quad [7\text{-}19]$$

Equations [7-18]-[7-19] should be calculated independently and in parallel with the above stiffness methodology (i.e., before and after each applied wrench ω, for every test). Subsequently, the calculated translational displacement δp (equation [7-20]) and rotation δR (equation [7-21]) of the end-effector can be expressed in the base frame ε_0 as:

$$\delta p = {}^{0}p_n' - {}^{0}p_n \quad [7\text{-}20]$$

$$\delta R = {}^{0}R_n' - {}^{0}R \quad [7\text{-}21]$$

This section detailed the process of calculating the joint stiffness values. The following section looks at the procedure that can be used to determine the joint stiffness values.

7.3 Procedure for Determining the Joint Stiffness Values

Applying the VJM technique within a robot's dexterous zones simplifies the stiffness analysis. The Complementary stiffness matrix (K_X) is a highly non-linear matrix and can be ignored during the calculation. For further understanding of (K_X) and its exclusion based on applying a dexterity analysis, refer to [58, 107, 149].

SKMs are usually fixed to the ground or ceiling, depending on the application. The workpiece can be situated at any location within the robot's workspace envelope. The workpiece is usually secured on worktables and tilt tables and can be adjusted at several angles and distances away from the robot. The procedure of detecting postures of higher stiffness necessitates multiple points to be tested at various robot configurations. The stiffer points can be used to locate the workpiece within the workspace for enhanced robot performance. The following process applies to estimate the joint stiffnesses of an n-DOF robot within a dexterous zone. The method is illustrated in Figure 7-2. Similarly, the process to identify the calculated translational and rotational deflections of the robot end-effector is shown in Figure 7-3.

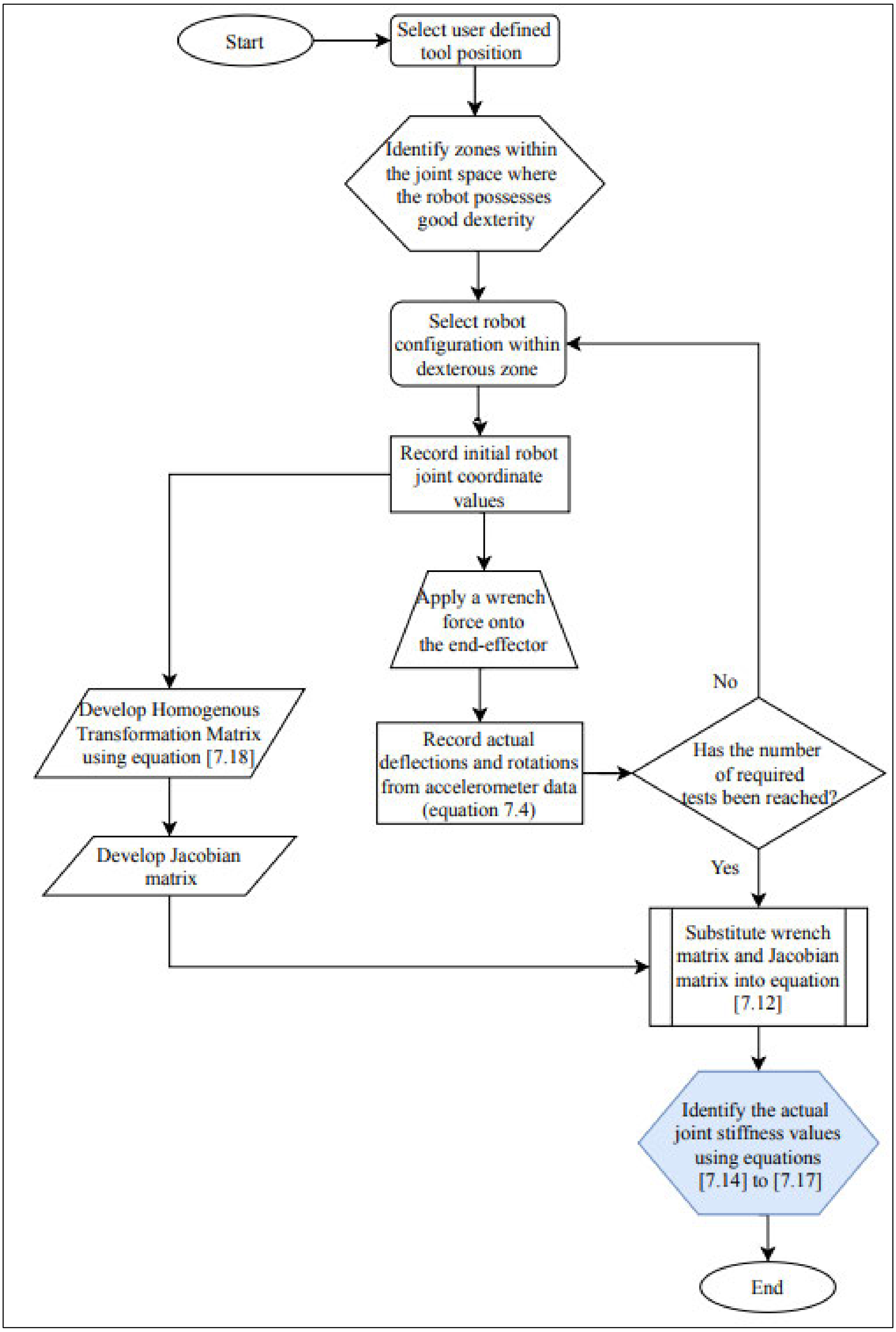

Figure 7-2: VJM Stiffness Procedure

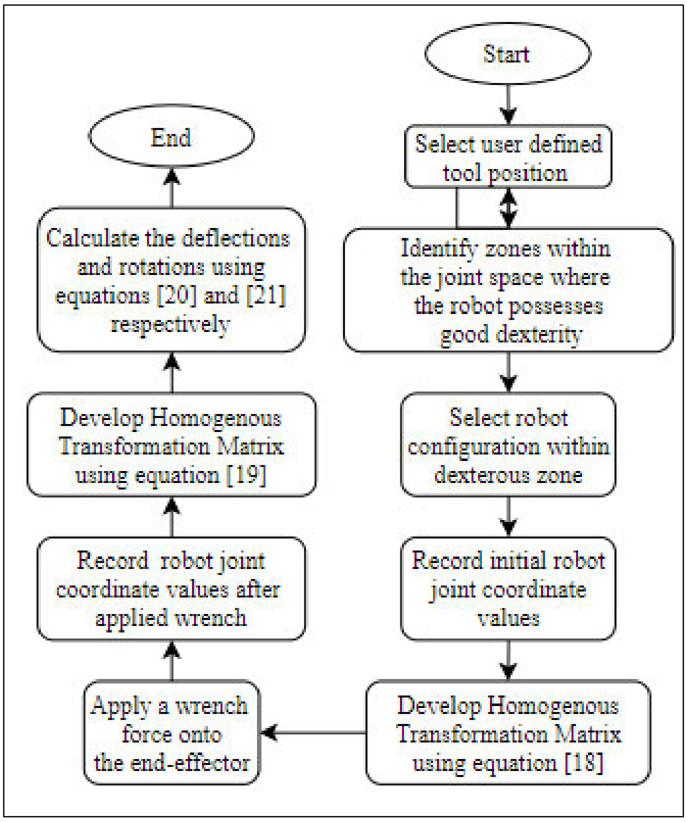

Figure 7-3: End-effector Calculated Deflection Procedure

Step 1: Records the initial robot joint coordinates at the user-defined point, which is required to evaluate the equation [7-18].

Step 2: Evaluates the Jacobian matrix derived from the robot's forward kinematic model. The Jacobian matrix provides an expression of the end-effector velocities derived from the robot's joint velocities, as shown in equation [7-22] below:

$$\begin{bmatrix} \dot{x} \\ \dot{y} \\ \dot{z} \\ \omega_x \\ \omega_y \\ \omega_z \end{bmatrix} = J \begin{bmatrix} \dot{q}_1 \\ \dot{q}_2 \\ \vdots \\ \dot{q}_n \end{bmatrix} \tag{7-22}$$

The Jacobian matrix has dimensions $6 \times n$, where n is the number of joints. For a 6-DOF robot, the Jacobian is of size 6×6, where the upper three rows of the matrix represent the linear velocity and the lower three rows, the angular velocity. The Jacobian matrix is configuration dependent and must be evaluated at points and configurations of interest.

Step 3: Applies the wrench force to the end-effector. The wrench force is a measured variable. The wrench vector is of size 6×1, as shown in equation [7-5]. The first three components represent the forces in the x, y, and z directions, and the last three components are the moments about each axis.

After the wrench force is applied, the joint coordinates of the end-effector are recorded to note the deflection from its initial position. These coordinates are used to evaluate equation [7-19]. The end-effector's translational and rotational displacements are determined by applying equations [7-20]–[7-21] about the user-defined point. Once the Jacobian and wrench matrices have been derived:

Step 4: Evaluates matrix A, as shown in equation [7-12].

Step 5: Records the measured deflection and orientation matrix δt , as shown in equation [7-4]. The translational and rotational deflections can be measured using several sensors, including accelerometers, laser trackers, and other precision displacement sensors.

Step 6: After developing the A and δt matrices, the joint stiffness values for one configuration can be evaluated using equation [7-13]. The result obtained from equation [7-13] is a square matrix. As previously mentioned, for improved joint stiffness accuracy, several tests are required, thus changing the matrix of size square to rectangular. This necessitates the need for equation [7-14].

The Moore Penrose Pseudo Inverse method, equation [7-17], can solve such non-square matrices. The output is the estimated joint stiffness of the robot, with better accuracy. The stiffness values can then be further analysed based on various sources of errors during the experimental procedure.

Having unpacked the procedure used to ascertain the joint stiffness values above, a clear and succinct stiffness modelling approach along with the workspace, singularity and dexterity analysis can provide manufacturers, roboticist and machinists with a simplistic solution to follow, to identify and improve the precision of their manufacturing tasks using SKMs, which has addressed Objective 4 of this study.

The next section endeavours to explore the procedure used to determine the link deflections.

7.4 Procedure for Determining the Link Deflections

Attention now shifts to identifying the deflection of the robot links. This analysis/exploration in section 7.3 was necessary because it provided a procedural guide to modelling the joint stiffness using the VJM, making it easy for machinists and roboticists to follow. Additionally, this analysis meets Objective 4, which was to *develop a systematic approach to the stiffness identification algorithm such that any roboticist can universally adopt it*.

The shortfall of the VJM is due to its lack of consideration of the link deflections, as the model assumes the links to be infinitely stiff. The deflection of the Fanuc M10-iA robot links was tested. The contribution of the link deflection to the end-effector deflection was examined. The procedure to determine the link deflections considers the links' weight, motors, and the translational force applied onto the end-effector. This section will evaluate the link deflection of an SKM with force applied to its end-effector. This link deflection methodology can be applied to any SKM of similar architecture. The method was also used to evaluate the link deflection of the Fanuc M10-iA, and its contribution to the end-effector deflection, in which the results are presented in Chapter 8.

Although the process of identifying the link stiffnesses may be regarded as straightforward, the result is an estimation and not the true value. SKM links are usually assumed to take the form of round-hollow or square-hollow shapes. The links can be approximated as a cantilever beam of length L with a payload W exerted at its end-point. The schematic of the cantilever beam is shown in Figure 7-4:

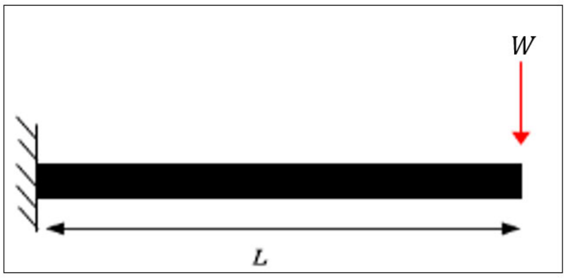

Figure 7-4: Schematic Diagram of a Cantilever Beam

The serial linkage system illustrated in Figure 7-5 shows a 3-link manipulator with 6 joints. The vertical displacement of links L_2 and L_3 are assumed to be far greater than the horizontal deflection occurring at L_1; hence, the deflection of the two upper links was considered in this research. To accurately model the links as a cantilever beam, the links are required to be fully extended.

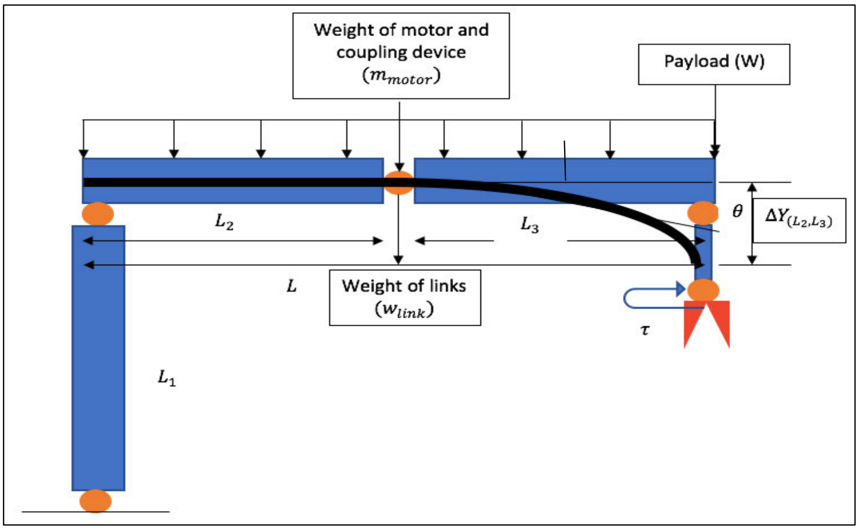

Figure 7-5: Free Body Diagram of Serial Link

The payload (W) is applied at the end at a distance L away from the L_1. The end-effector deflection is a result of both bending and torsion effects. Since the attention is on links L_2 and L_3, their weights, and weight of the motor that controls L_3, contributes to the overall deflection of the links. Furthermore, L_2 and L_3 are assumed to be of equal lengths, and hence the position of the weight of the motor is directed vertically downwards in between the links.

The deflection due to bending of the two links $\Delta Y_{(L_2,L_3)}$ is a product of the three forces acting on both the links. This is encapsulated in equation [7-23] below:

$$\Delta Y_{(L_2,L_3)} = \left[\frac{g w_{link} L^4}{8EI}\right]_{\substack{Links \\ (uniformally \\ distribute\ load)}} + \left[\frac{5 g m_{motor} L^3}{48EI}\right]_{\substack{motor \\ (concentrated\ load \\ at\ centre)}} + \left[\frac{g W L^3}{3EI}\right]_{\substack{payload \\ (end-point)}} \quad [7\text{-}23]$$

where E defines the modulus of elasticity; I, the moment of inertia; L , the total length of both links; g, the acceleration due to gravity; w_{link}, the weight of the links; m_{motor}, the weight of the motor; and lastly, W, the payload applied to the end-effector.

The weight of the links can be calculated using equation [7-24]:

$$w_{link} = \rho_{material} A_c L \quad [7\text{-}24]$$

where, $\rho_{material}$ is the density of material and A_c, the cross-sectional area of the links.

The payload (W) is responsible for the bending of the end-effector, and is the only force acting at the end-point. The deflection due to the wrist configuration ΔY_{wrist} is shown in equation [7-25] below:

$$\Delta Y_{wrist} = \frac{gWL_{wrist}^3}{3EI} \qquad [7\text{-}25]$$

where, L_{wrist} is the length of the wrist configuration.

The twisting of links L_2 and L_3, ΔY_{twist}, is due to the torque produced by the payload applied at a perpendicular distance to the main links. The applied torque twists links L_2 and L_3 by an angle θ, and as a result, the deflection due to the twisting of the links is shown in equation [7-26]:

$$\Delta Y_{twist} = L_{wrist}\, sin(\theta)\, cos(\theta) \qquad [7\text{-}26]$$

where θ defines the angle of the twist

Finally, the overall robot arm deflection can be determined by summing up the deflections due to both bending and torsion of links L_2 and L_3. This is expressed in equation [7-27] as follows:

$$\delta_{Total} = Total\ deflection = \Delta Y_{(L_2,L_3)} + \Delta Y_{wrist} + \Delta Y_{twist} \qquad [7\text{-}27]$$

This section focused on identifying the deflection of the robot links, since the VJM does not include the contribution of the links to the end-effector deflection. This is used to determine the contribution of the links to end-effector deflection, as this is a shortfall of the VJM approach. However, this will be discussed further in Chapter 8. Additionally, factors contributing to deflection were also noted, along with the forces impinging on the links. To conclude this chapter, some closing comments follow next.

7.5 Chapter Summary

This chapter presented the analysis of the joint stiffness of an n-DOF serial kinematic structure. The analysis began with the joint stiffness identification using the VJM. Based on the literature review presented in Chapter 2, the three most popular methods used for stiffness modelling of robotic systems are the FEA, MSA, and VJM techniques. Thus, for the purpose of this research, the VJM was applied, which is attributed to Objective 3 of this study, which was to *research, establish and identify a suitable stiffness modelling approach*. This model was broken down and discussed in detail to allow any machinist or roboticist to follow through quickly and easily, addressing Objective 4 of this study, which was to *develop a systematic approach to the stiffness identification algorithm such that any roboticist* *can universally adopt it*. Finally, the method of identifying the link deflection was presented. The next chapter proceeds to unpack the experimental procedure and physical testing results.

8. EXPERIMENTAL ANALYSIS AND RESULTS

8.1 EXPERIMENTAL ANALYSIS AND TESTING OVERVIEW

This chapter elucidates the experimental procedure and physical testing results. To illustrate the application of the VJM technique, and the effectiveness of the proposed dexterity analysis, two tests were developed, namely, the *non-dexterous* and *dexterous* tests. The non-dexterous tests were based on setting the robot's end-effector at a fixed posture at multiple equidistant points, and the dexterous tests were based on applying various robot configurations at the same equidistant points. This setup aimed to provide an effective means of comparing multiple stiff areas and postures within the robot's workspace. Both tests were developed in two phases. The first phase involved measuring the actual deflections using three piezoelectric IEPE accelerometer modules attached to the end-effector, and an MPU-6050 to measure the rotations using its gyroscopic sensor in 3-D (x, y, and z). The second phase applied the formulation proposed by Mondragon [106] for the dexterity study, to evaluate the joint stiffnesses using the VJM technique.

The layout of this chapter is as follows. The first section below looks at the experimental apparatus (section 8.2) used. This is followed by a discussion of the accelerometer setup and technique to remove bias (section 8.3); experimental point cloud development (section 8.4); experimental results (section 8.5); application of the static point dexterous posture identification approach (section 8.6); a discussion of the results (section 8.7); and a summary of the main findings of the chapter (section 8.8).

8.2 EXPERIMENTAL APPARATUS

This section presents the experimental apparatus applied to test the VJM technique. This includes the robot (sub-section 8.2.1), sensors, and data acquisition devices (sub-section 8.2.2). These are explained in more detail below.

8.2.1 THE ROBOT USED IN THIS STUDY

The robot shown in Figure 8-1a is a Fanuc M10-iA manufacturing robot. This robot simplifies applications due to its compact structure and flexibility in terms of mounting configurations. The robot has 6-DOF, and can withstand a maximum end-load of 13 kg. The robot is primarily designed for general top-speed pick-and-place, coating, cutting, and machine tending. This specific robot was the only SKM available to conduct this research. For further information about the robot in terms of its front, side, and top dimensions, see Appendix A. For the wrench tests a stainless-steel mounting, herein called "torque tool" shown in Figure 8-1b was developed as well as a custom made torque wrench.

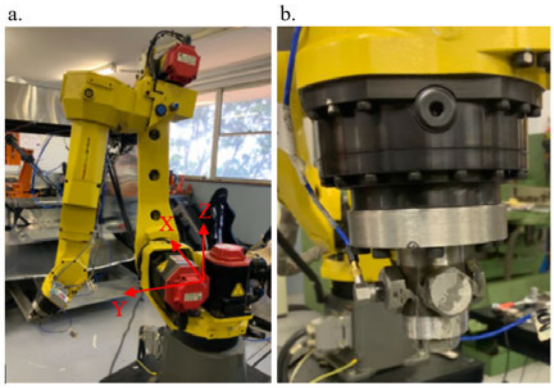

Figure 8-1: a) Fanuc M10-iA Robot, and b) Mounting and Fabricated Torque Tool

8.2.2 Data Acquisition and Sensors

The sensors used to measure the deflection of the robot's end-effector were three IEPE accelerometers attached on the (x, y and z) axis of the fabricated torque tool shown in Figure 8-1b. To measure the rotation of the end-effector, a MEMS 6-DOF accelerometer comprising of 3-axis, the accelerometer, and 3-axis, the gyroscope was used. The specifications of both the IEPE and MPU accelerometers and a 25 kilogram S-Type load cell in Figure 8-2 are presented in Table 8-1 further below.

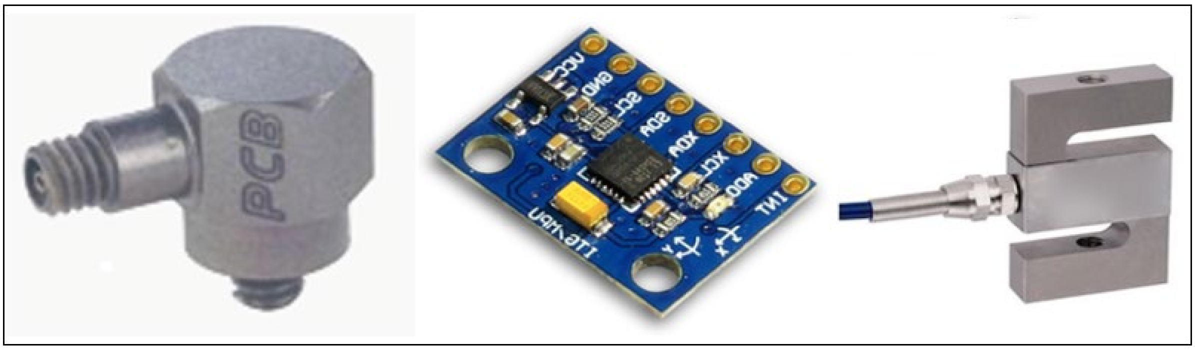

Figure 8-2: PCB Accelerometer, b) MPU Accelerometer, and c) 25 kilogram S-Type Load Cell

Table 8-1: Accelerometer Specifications

Piezoelectric Accelerometers			**S-Type Load Cell**			
Make	**Sensitivity**	**Measurement range**	**Material**	**Capacity**	**Output Sensitivity**	**Cable Length**
PCB	(±10%) 100 mV/g (10.2 mV/(m/s²))	±50 g pk (±491 m/s² pk)	Alloyed Steel	25 kg	3mV/V	3 m

The Data Acquisition (DAQ) device used includes: (a) a 4-slot USB CompactDAQ (cDAQ) 9174 chassis; (b) a 4-channel dynamic signal acquisition NI 9234 module – used to interface with the 3 IEPE accelerometers; (c) a simultaneous bridge NI 9237 module – interfaced with the S-Type load cell; and lastly, (d) an Arduino Mega 2560 – a microcontroller interfaced with the MPU6050 accelerometer. These are illustrated in Figure 8-3 below.

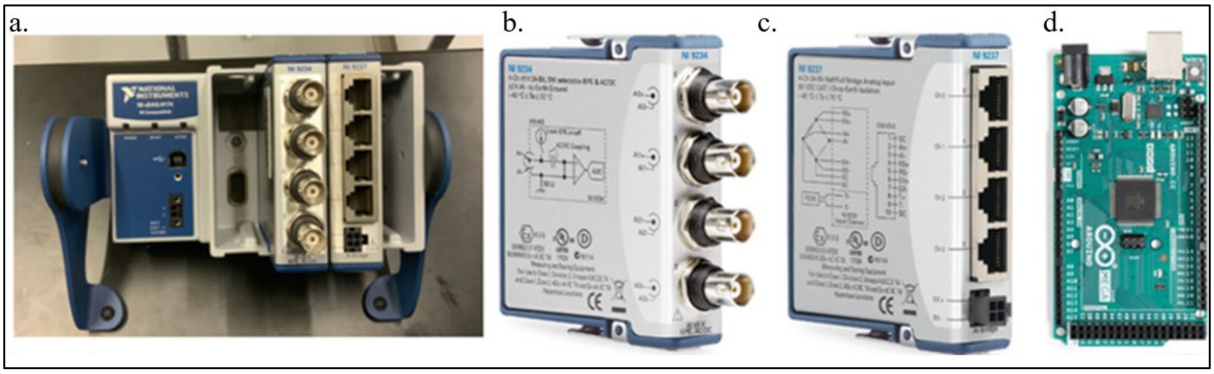

Figure 8-3: a) cDAQ, b) IEPE Module, c) Strain Gauge Module, and d) Arduino Mega

The flow diagram displaying all the connections between the equipment and sensors is shown in Figure 8-4 below. A LabVIEW GUI shown in Figure 8-5 was developed to show: the raw acceleration and wrench force, and gyroscope measurements from both the NI DAQ and Arduino, respectively. The LabVIEW code was automated, and data logging was controlled with a virtual Boolean switch in the VI.

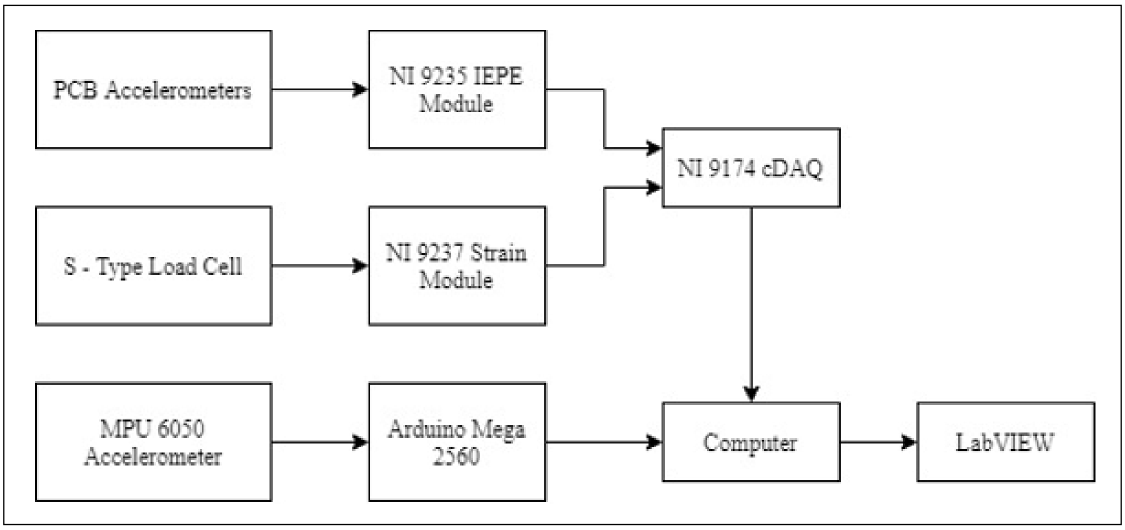

Figure 8-4: Hardware and Software Fusion

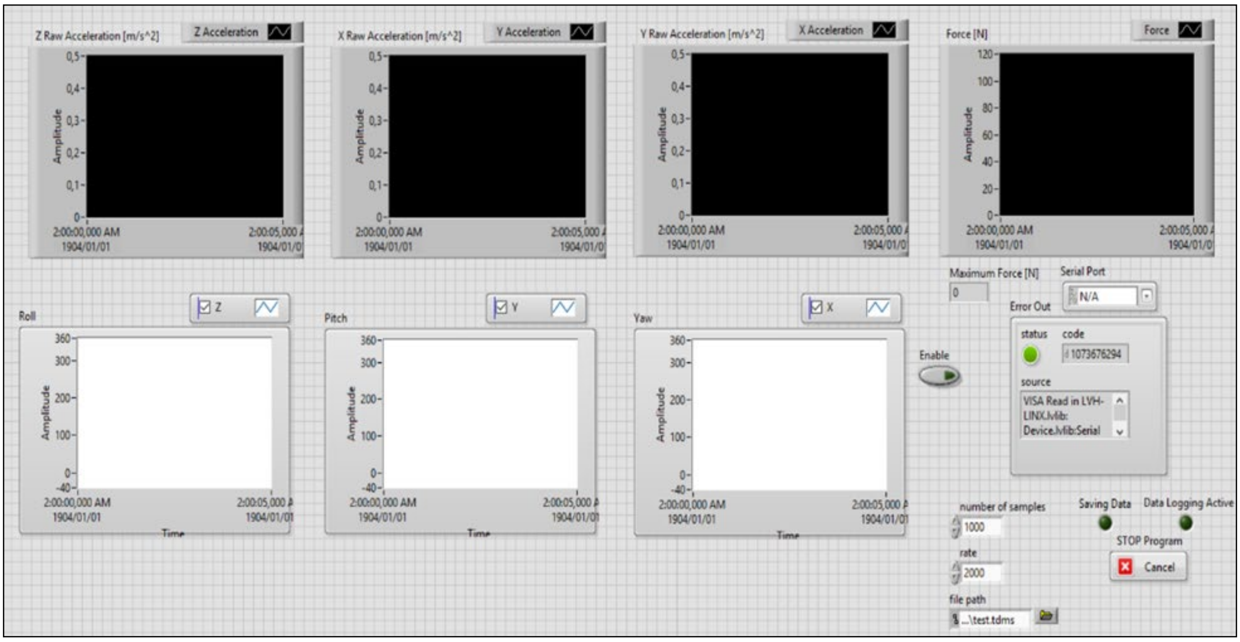

Figure 8-5: LabVIEW GUI Interface

The code was split into two parts. The LabVIEW VI, as shown in Figure 8-6, was used to obtain the raw acceleration, rotation and force signals from the IEPE accelerometers, MPU6050, and S-Type load cell, respectively. The second VI shown in Figure 8-7 was used to post-process the data and filter the noise by applying a polynomial detrending bias removal technique that was applied by Pan *et al.* [164] and discussed in Chapter 2 to correct the integration errors from acceleration to displacement.

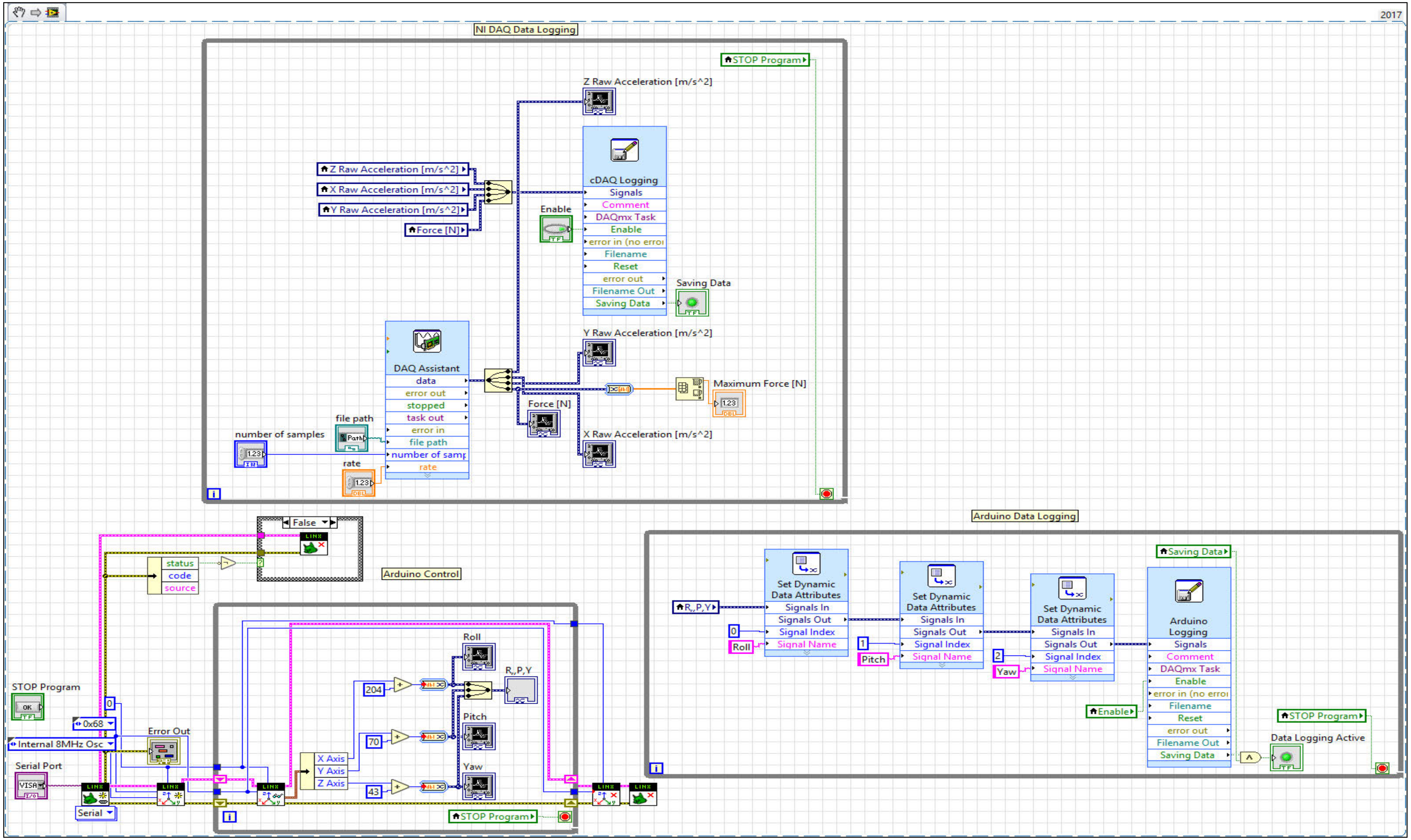

Figure 8-6: LabVIEW Real Time Testing GUI (Block Diagram)

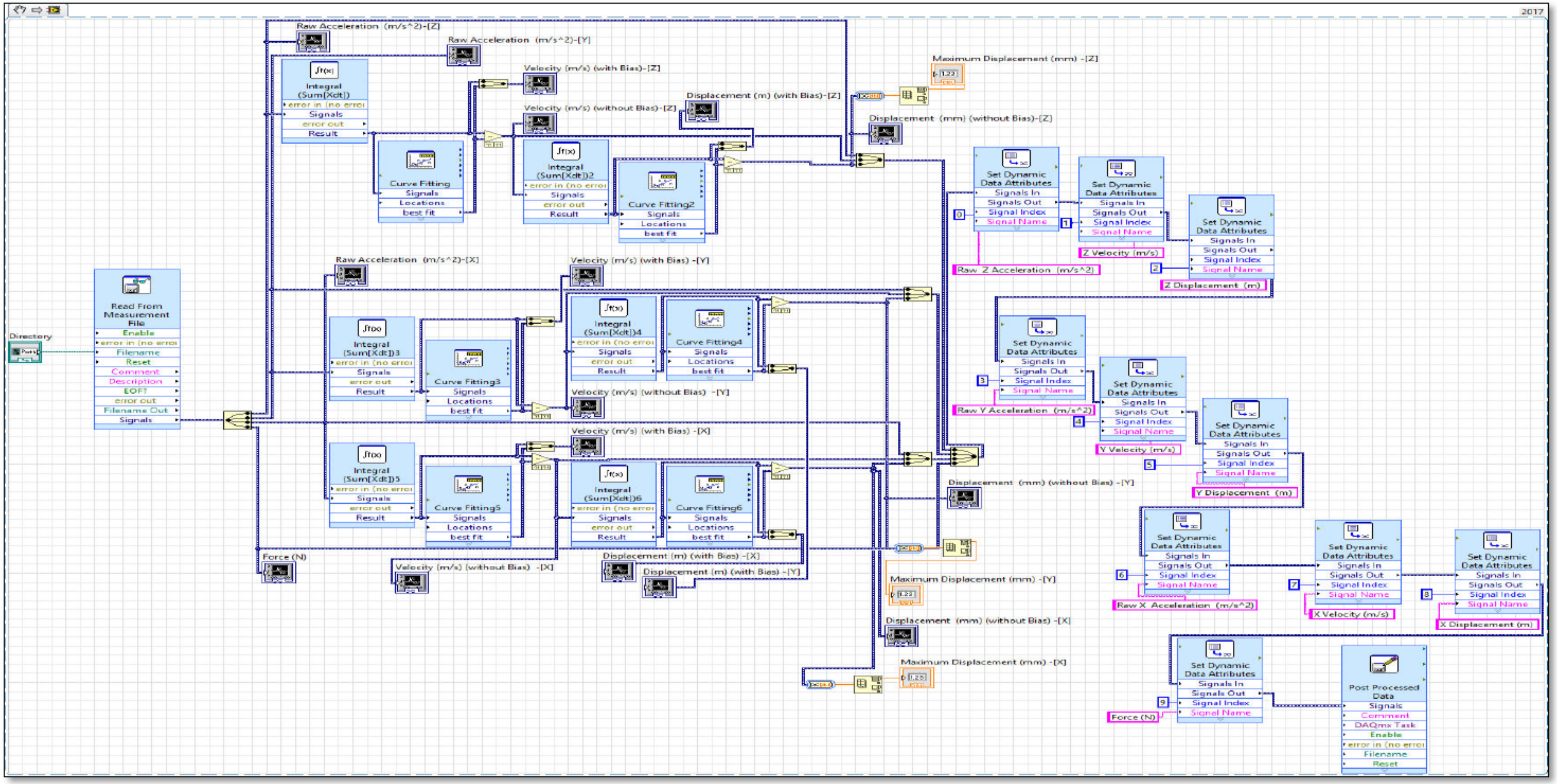

Figure 8-7 LabVIEW Post-Processing GUI (Block Diagram)

8.3 ACCELEROMETER SETUP AND SOURCES OF NOISE

This section looks at the accelerometer setup and considered all sources of noise that influenced the end-effector deflection measurements. As already mentioned, three IEPE accelerometers were used to measure the deflection. Due to budget constraints, a tri-axial accelerometer could not be used.

The use of sensitive accelerometer modules during deflection testing should consider several factors to ensure accurate measurements [167]. A few considerations that were enforced during the experimental setup include: the stainless-steel torque tool was bolted with 8 M4 socket head cap screws, each torqued accordingly to ensure a rigid connection with the end-effector. The PCB accelerometers were carefully fixed using a strong adhesive that had zero interference with their frequency. Due to physical constraints, such as hard to reach/inaccessible areas of the robot, the accelerometers could not be ideally located along each axis of rotation. They were located on the torque tool and placed as close as possible to the centre of rotation. The accelerometers were all connected via Bayonet Neill-Counselman (BNC) cables to the Ni DAQ and were neatly mounted to ensure minimal cable noise. The temperature of the laboratory was fairly consistent during testing, as most tests were performed after sunset. The sensitivity to environmental effects was low and was adequately considered before performing each test. Figure 8-8 shows the placement of the accelerometers on the torque tool.

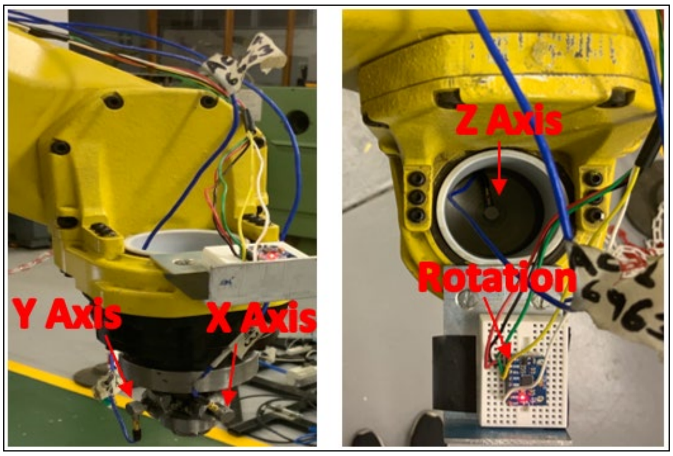

Figure 8-8: Stainless-Steel End-Effector Mounting and Accelerometer Placement

The stainless-steel torque tool attached to the end-effector was explicitly designed to handle multiple cyclic wrench tests. An average force of 55 – 60 N was applied along the z-axis of the tool. The robot's end-effector was capable of handling greater forces, however, due to the cyclic nature of the non-dexterous and dexterous tests, the forces were controlled to prevent any permanent damage to the robot. The force was measured by attaching an S-Type Route 25 kg capacity load cell. The load cell was secured by eye bolts attached to the custom-made torque wrench and used as the applied wrench (force) to deflect the end-effector.

As previously mentioned, the bias removal technique to offset the error during the conversion of acceleration to displacement was a least-squares polynomial fitting algorithm. Studies that have validated this algorithm as a feasible solution to correct the DC offsets include Ren *et al.* [165] and Niu *et al.* [166]. Having considered the accelerator setup and bias removal technique in the section above, attention now shifts to the development and layout of the testing points.

8.4 Experimental Point Cloud Development

This section focuses on the testing point cloud development using a cylindrical coordinate system approach. An explanation of the point cloud setup was presented in Chapter 4, however, an alternative explanation is provided with the use of Figure 8-9 and Figure 8-10 below.

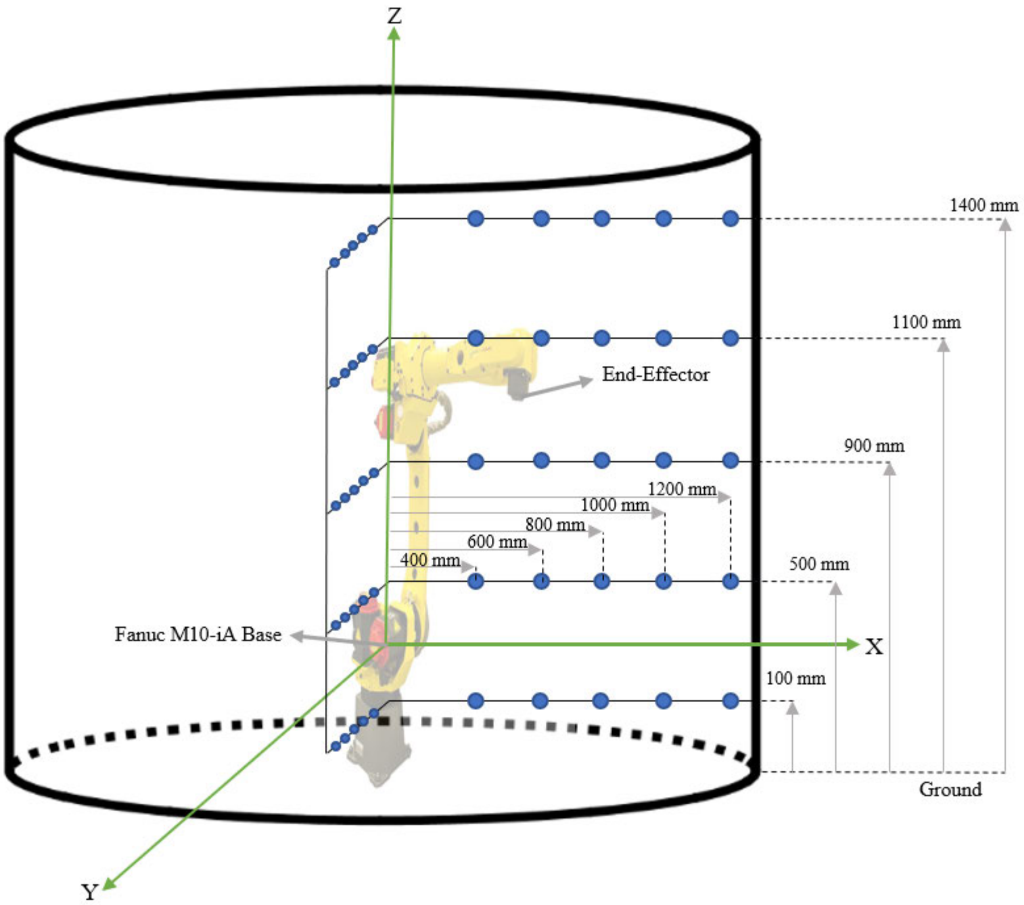

Figure 8-9: 3-D View of Joint Stiffness Testing Points

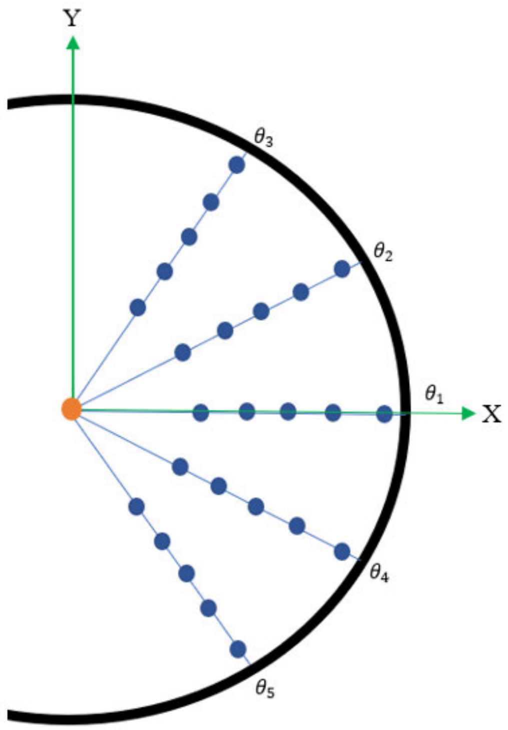

Figure 8-10: 2-D View of Joint Stiffness Testing Points (X-Y Plane)

The joint stiffness values were tested and compared by a 25-layered network of testing points. The network was established, starting at the robot base, by placing a point at a radial distance (r) of 400 mm away from the centre of the robot's base and 900 mm above the ground in the z-direction. This point was incremented twice in the -θ (counterclockwise) and twice in the +θ (clockwise) by a constant 0.523599 radians (equivalent to 30°), see Figure 8-10. This formed an arc consisting of 5 testing points. Each of the 5 points along the arc was multiplied twice in the +z and -z directions by a constant vertical distance of 400 mm. This gave a network of 25 testing points at 400 mm away from the robot base. The network of 25 points was repeated at a constant r of 200 mm, giving 5 networks of 25 testing points. As a result, the joint stiffness values were tested at 400 mm, 600 mm, 800 mm, 1,000 mm, and 1,200 mm distances away from the centre of the robot's base, and the dexterous tests were tested at 400 mm, 800 mm, and 1,200 mm.

This testing configuration was developed for three reasons: (1) to develop a trend analysis of the joint stiffnesses at multiple distances away from the robot's base and at multiple heights above the ground; (2) the VJM requires multiple testing points to arrive at an accurate solution; and (3) to test the repeatability of the VJM modelling approach. The setup of points helped identify optimal points and areas to perform tasks that impose high applied forces. In total, the joint stiffness consisted of 125 testing points. The experimental results are presented next. Each network of points at a radial distance of 400 mm will be referred to as r_1; at 600 mm as r_2; at 800 mm as r_3; at 1,000 mm as r_4; at 1,200 mm as r_5. Also, for the angular distances, and from Figure 8-10, θ_1 was chosen as the reference line. This implied θ_2 and θ_4 lines were 30° from θ_1, and, θ_3 and θ_5 were 60° from θ_1.

8.5 Experimental Results

The experimental results are presented in this section. The stiffness and dexterity analyses were algebraically solved using Wolfram Mathematica. The suitability of this software was explained in Chapter 2.

As described in Chapter 7, each test was accompanied by a 6-D wrench vector, a 6-D end-effector displacement vector, and an A matrix. A linear regression model was applied to verify the measured deflections and rotations against the calculated deflections and rotations, as determined by a number of equations [7-18]–[7-21]. The regression analysis confirmed the deflection and rotation measurements to be reliable since a strong correlation existed. Based on the sample size of the tested point per radial distance, the R-Squared number was adequate to confirm the reliability of the measured deflection and rotation values.

The following sections present the dexterous zones developed using the formulation presented in Chapter 6. This is followed by discussing the measured and calculated deflections and rotations, estimated joint stiffness values, and overall joint stiffness per radial distance. The trends per radial distance and a joint stiffness by posture are also presented and analysed further below.

8.5.1 Identification of Dexterous Zones

The dexterity analysis aimed at testing various equidistant points at multiple configurations away from the robot's base. The initial investigation made to identify the optimal configurations within a radial distance was crucial to understanding the kinematical characteristics of the manipulator.

The dexterity postures were determined by constraining the end-effector at equidistant points along r_1, r_3 and r_5, and then adjusting the robot's configuration at the point. The dexterous range was determined by Euler angles (α, β, γ). The γ rotation, which is generally used for obstacle avoidance, falls out of scope for this research and was set to zero. A total of 5 configurations per zone was tested, giving a total of 45 testing points.

The dexterous ranges evaluated as per the methodology explained in Chapter 6 were evaluated at θ_1, θ_2 and θ_4 at r_1, r_3, and r_5 , and at the height of z_2 = 500 mm. The results are displayed in Table 8-2.

Table 8-2: End-Effector Coordinates and Dexterous Coordinate Ranges

Radial Distance	**Dexterous Zone**	**End-Effector Coordinate (x, y, z)**	**Beta (β) (°)**	**Alpha (α) (°)**	**Gamma (γ) (°)**
r_1	1	-600 -100 100	-9.75 ± 34.04	-99.46 ± 62.45	0
	2	-600 -100 -300	-40.60 ± 37.28	-99.46 ± 78.41	0
	3	-600 -100 500	27.28 ± 36.00	-99.46 ± 68.21	0
r_3	1	-600 -500 100	-11.20 ± 29.75	-129.81 ± 58.81	0
	2	-600 -500 -300	-44.70 ± 36.91	-129.81 ± 69.93	0
	3	-600 -500 500	30.70 ± 33.93	-129.81 ± 62.64	0
r_5	1	-600 -900 100	-6.89 ± 37.18	-146.31 ± 50.35	0
	2	-600 -900 -300	-31.14 ± 35.68	-146.31 ± 52.79	0
	3	-600 -900 500	19.92 ± 36.84	-146.31 ± 51.31	0

8.5.2 JOINT STIFFNESS IDENTIFICATION

The focus of this section is to provide the results of the VJM at each radial distance for both non-dexterous and dexterous tests. The point cloud shown in Figure 8-9 represents the layout of each testing point. For the non-dexterous tests, the robot end-effector was fixed in the $-z$ direction at each point. Although the point cloud was developed to test 25 points per radial distance. On average, 20 tests were performed per radial distance. This was due to singularities that were unavoidable, especially when the robot's end-effector was set to r_1 and r_5. Towards the middle of the workspace, at r_2, r_3 and r_4, the testing points were hardly affected by singularities. Although the singularity identification explored in Chapter 5 assisted with developing points that are far from singularities, tests had to be performed at multiple distances away from the robot base and multiple heights from the ground. As a result, some singularities were unavoidable.

The methodology shown by equations [7-18] and [7-19] calculated the linear and angular displacements. The stiffness measurements were dependent on the deflection and rotation values, and hence, a relationship between the measured and calculated deflection and rotations was required. As previously mentioned, the measured end-effector displacements and rotations were validated by applying a linear regression model. The model was performed such that the measured deflections and rotations represented the response (Y) input, and the calculated deflection and rotation, the predictor (X) input. For the non-dexterous tests, the results exhibited a strong positive relationship between both measured and calculated, with R-Squared values ranging between 69.9% and 79.7% for the deflection values, and 63.3% and 68.3% for the rotation values for all 5 radial distances. For the dexterous tests, the linear regression analysis had R-Squared values ranging between 72.7% and 82.3% for the deflection values, and 65.7% and 71.1% for the rotation values. This showed that the calculated model was robust and that the measured results were fit for the stiffness evaluation.

It is important to note that the VJM approximates the joint stiffness results, since the joints are being modelled as virtual springs.

The tests within the dexterous zones followed the same point configuration shown in Figure 8-9; however, as previously mentioned, only r_1, r_3 and r_5 were analysed. A total of nine dexterous zones were tested. Figure 8-11 and Figure 8-12 reveal the deflection box-and-whisker plot for both non-dexterous and dexterous tests, respectively.

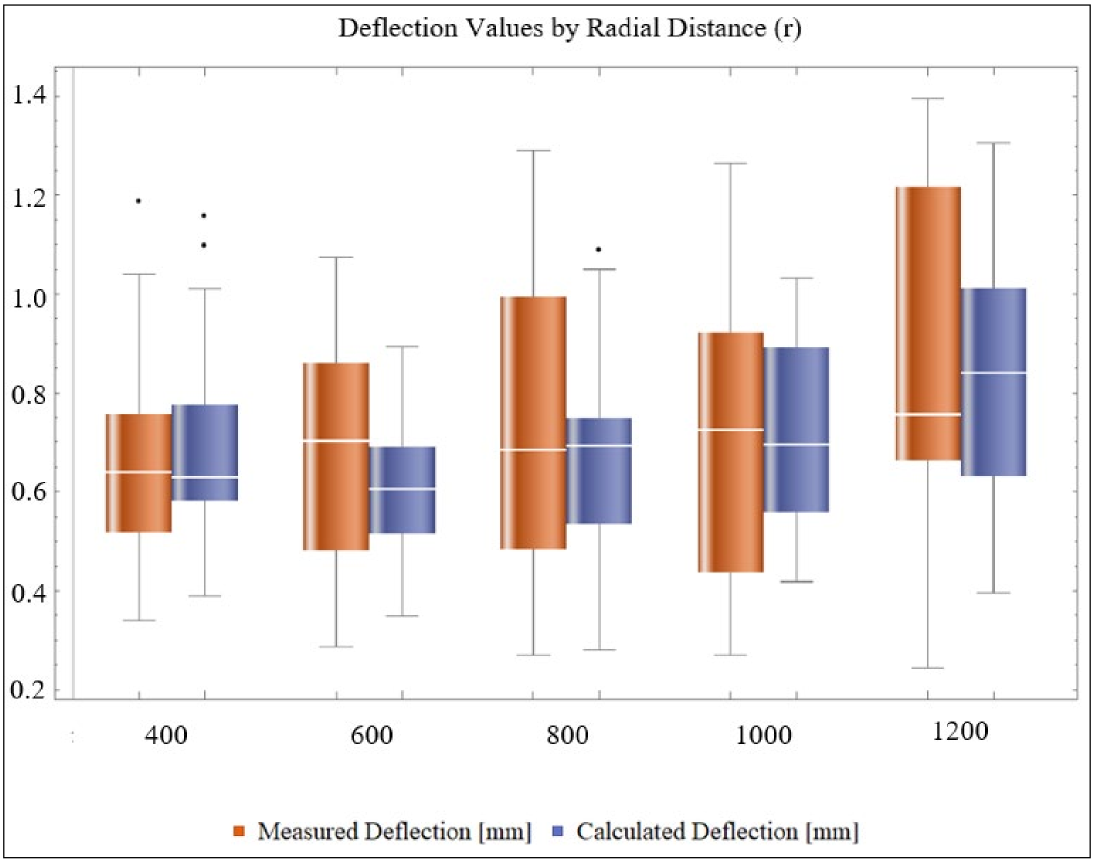

Figure 8-11: Non-Dexterous Tests: Measured and Calculated Deflections [mm]

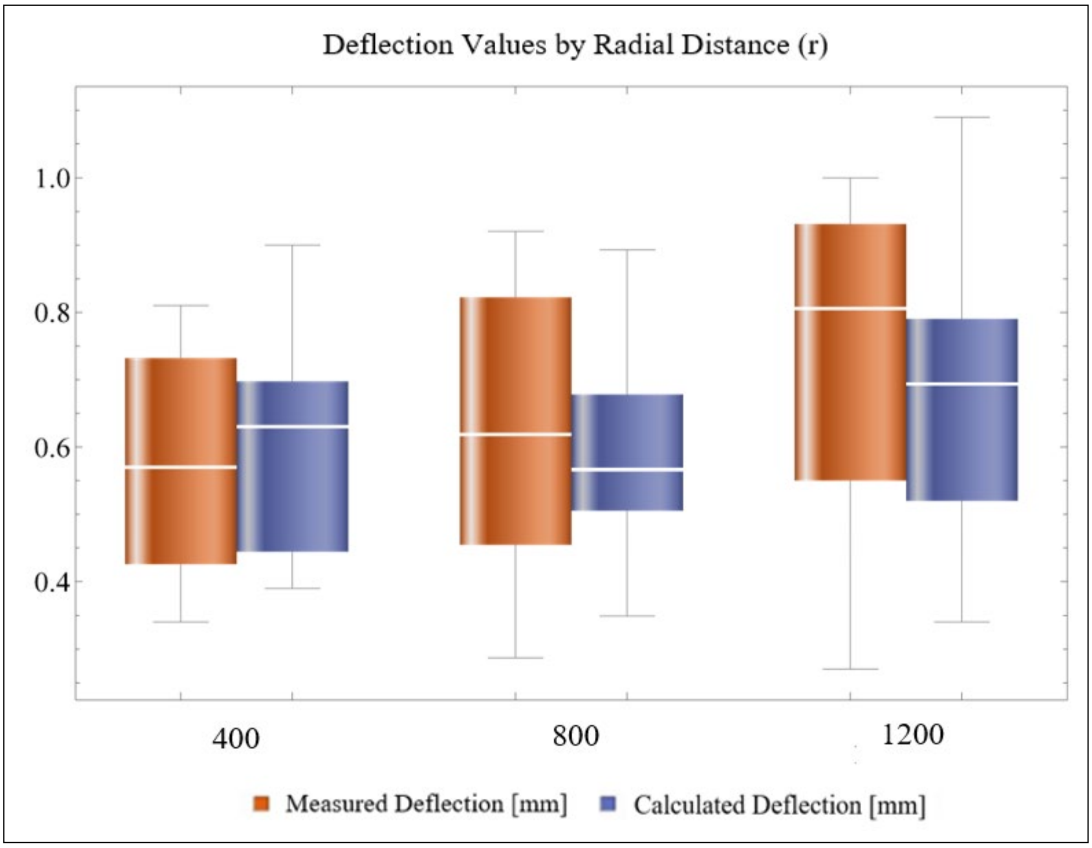

Figure 8-12: Dextrous Tests: Measured and Calculated Deflections [mm]

To note, the overall trend in Figure 8-11 and Figure 8-12 for the non-dexterous and dexterous tests displayed a gradual increase in deflection from r_1 to r_5. The maximum measured and calculated deflection for r_1 was 1.19 mm and 1.16 mm, while for the dexterous tests, the measured and calculated deflections for r_1 was 0.81 and 0.9, respectively. The measured and calculated deflections for r_3 was 1.29 mm and 1.02 for the non-dexterous tests, and 0.92 mm and 0.89 for dexterous tests, respectively. Evidently, an improvement in deflection is noticed between the non-dexterous and dexterous tests. The greatest measured deflections for both tests were recorded at r_5, with the measured and calculated deflection being 1.39 mm and 1.31 mm for the non-dexterous tests and 1.00 mm and 1.09 mm for the dexterous tests. The overall deflection performance during the dexterous tests shown in Figure 8-12 improved by 46% compared to the non-dexterous tests. This improvement was subjected to dexterous configurations about a point in space.

A further examination was performed to understand the influence of the robot's link deflections to the end-effector deflection. The link deflections were modelled during each test, with the robot arm fully extended. The greatest contribution to the end-effector deflection, apart from the joints, were links 2 and 4. The link stiffnesses were estimated under various wrenches by modelling the robot links as a square cross-sectional hollow beam. The link deflections measured were during the maximum extension of the robot. Results displayed link 3 to be responsible for 0.9% of the end-effector displacement. Link 4, the second-longest of the links, was positioned nearly horizontal when the robot was fully extended, and due to its cantilever effect, it contributed 11% to the end-effector displacement. Link 2, the longest link and furthest from the end-effector, contributed 9% to the end-effector displacement. These results presented a limitation of the VJM stiffness identification method in non-dexterous and dexterous tests.

Furthermore, Figure 8-13 and Figure 8-14 show the box-and-whisker plot of the rotations measured and calculated about the x, y, and z-axes due to the applied torque wrench end-effector for both non-dexterous and dexterous tests.

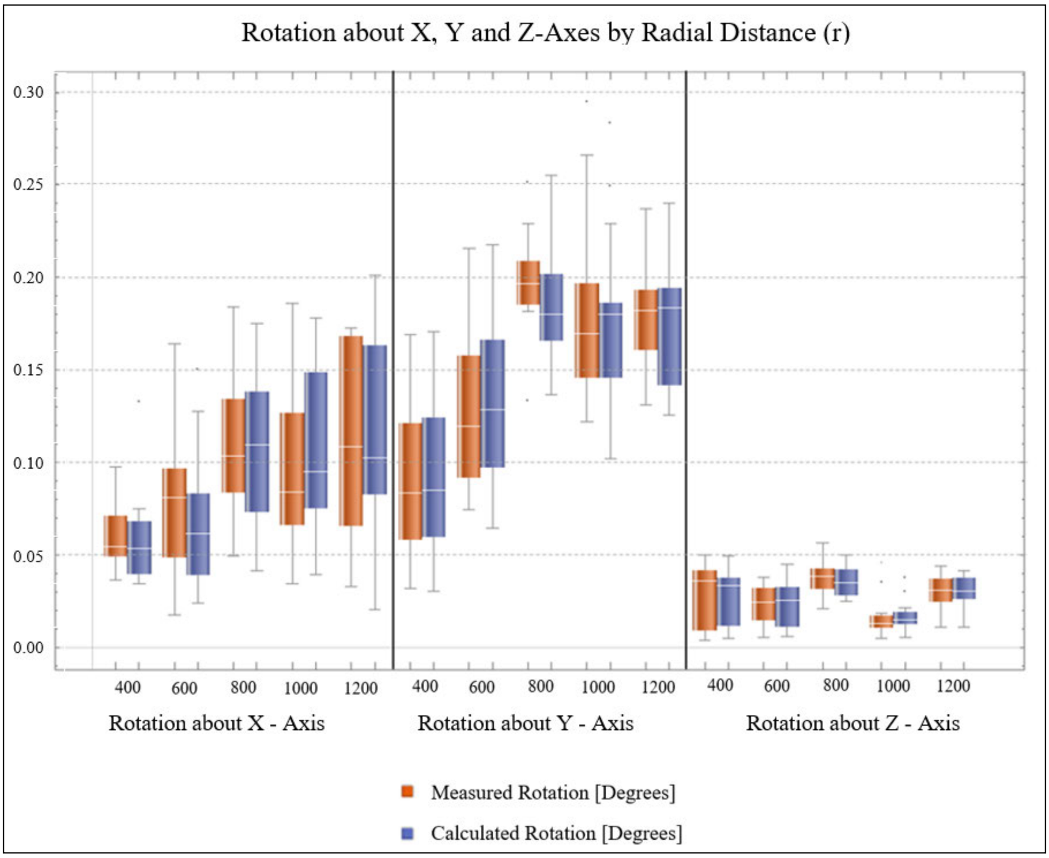

Figure 8-13: Non-Dexterous: End-effector Rotations about X, Y and Z-Axes by Radial Distance [°]

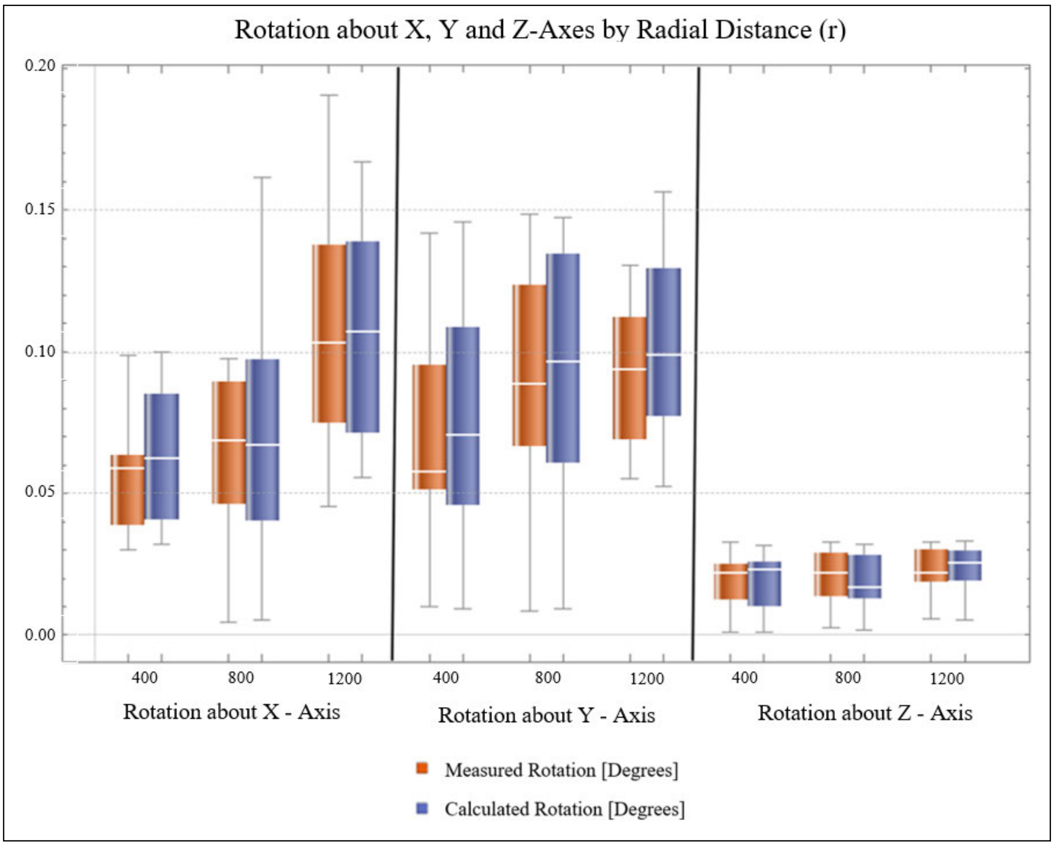

Figure 8-14: Dexterous: End-effector Rotation about X, Y and Z-Axes by Radial Distance [°]

To explain, a similar trend to the end-effector deflections was observed for the rotation measurements. For the x and y directions, the minimum end-effector rotations occurred closest to the robot base at r_1 and increased as the end-effector moved further away to r_5. The z-axis recorded a similar rotation, with relatively small magnitudes over all radial distances. In Figure 8-14, the z-axis rotation remained relatively consistent in magnitude over r_1, r_3 and r_5. The rotations about the x, y and z-axis during the dexterous tests shown in Figure 8-14, showed an improvement compared to the non-dexterous tests shown in Figure 8-13. The average rotation measured about the x-axis improved by 16%, the y-axis improved by 42%, and the z-axis improved by 28%.

The trend line of the non-dexterous and dexterous stiffness values evaluated over 21 and 15 points for r_3 is presented in Figure 8-15 and Figure 8-16, respectively.

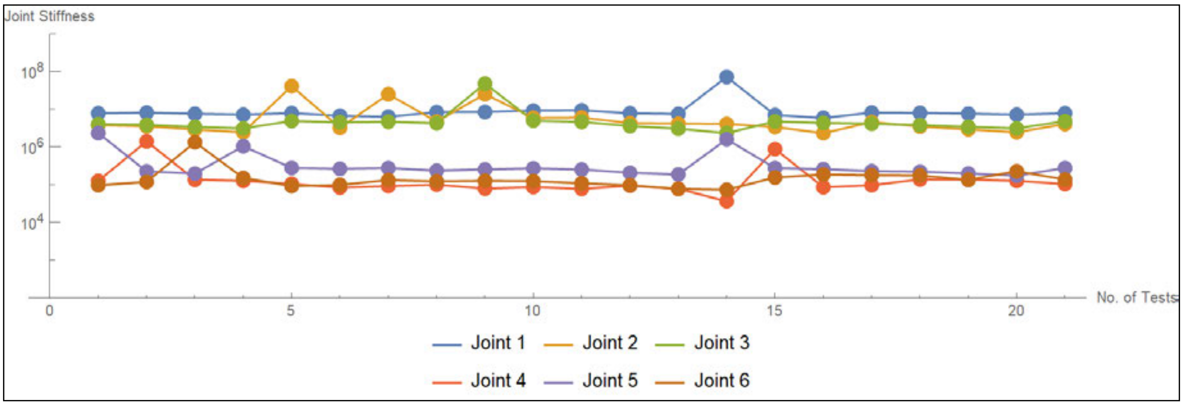

Figure 8-15: Non-Dexterous: Estimated Joint Stiffness Values [MN. m/rad] – r_3

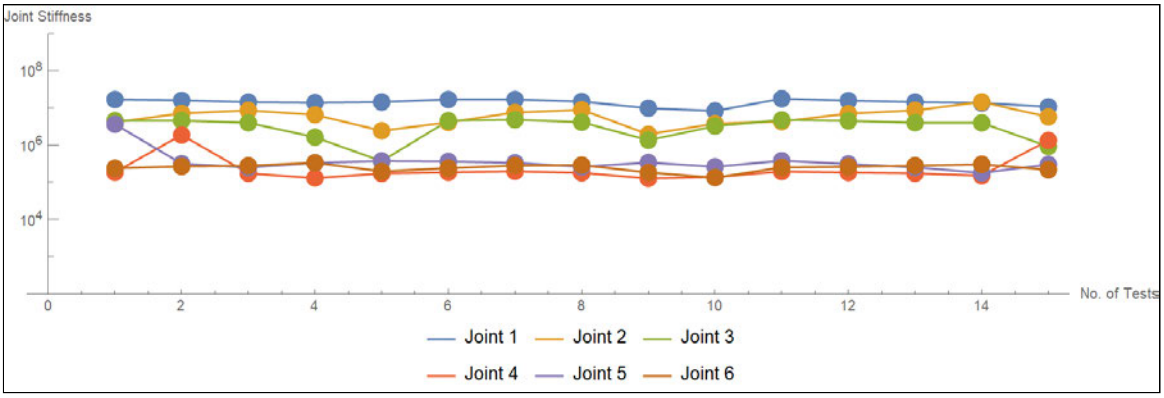

Figure 8-16: Dexterous: Estimated Joint Stiffness Values [MN.m/rad] – r_3

Evidently, r_1 and r_5 showed a similar trend analysis (refer to Appendix D). The linearity of the trend line is reasonable, bearing in mind that tests were performed without considering dexterity. Figure 8-16 shows the trend line for the joint stiffness evaluation during the dexterous tests. The linearity of the graph for r_3 drastically improved from the non-dexterous tests shown in Figure 8-15. A comparable trend line relationship with and without considering dexterity was found in Testa [110]. The linearity in Figure 8-16 suggests that the kinematical performance of the robot is more stable as opposed to tests without considering dexterity.

A stiffness analysis by posture was also investigated according to the dexterous ranges recorded for r_1, r_3 and r_5 in Table 8-2. At r_1, r_3 and r_5, the joint stiffnesses were measured within the dexterous zones defined by Table 8-2 for each. The joint stiffnesses were estimated by averaging all stiffness values for r_1, r_3 and r_5 (at points mentioned in Table 8-3). For each posture, the end-effector (joint 4, joint 5 and joint 6) stiffness values are shown in Figure 8-18, Figure 8-20, and Figure 8-22 (note that only testing points and postures for r_1, r_3 and r_5 at z_2 = 500 mm are shown in each image) – refer to point cloud setup in Figure 8-9. Since the lower half of the robot (joint 1, joint 2 and joint 3) generally displayed high stiffnesses, the focus was more on the end-effector joints stiffnesses, since the applied wrench force directly impacted these joints.

Table 8-3: Dexterous Testing Points

Radial Distance	***r* (mm)**	***z* (mm)**	***θ* (°)**
r_1	400	100	0
		500	
		900	
r_3	800	100	0
		500	
		900	
r_5	1200	100	0
		500	
		900	

The posture tests were performed about the mean β *and* α values at each dexterous zone, then a further four tests at two equally distant β and α values above and below the mean. This gave a total of five postures per dexterous zone. Each posture was labelled from 1 to 5 as shown in Figure 8-17, Figure 8-19, and Figure 8-21, and the corresponding posture joint stiffnesses are labelled above each of the bars as shown in Figure 8-18, Figure 8-20, and Figure 8-22.

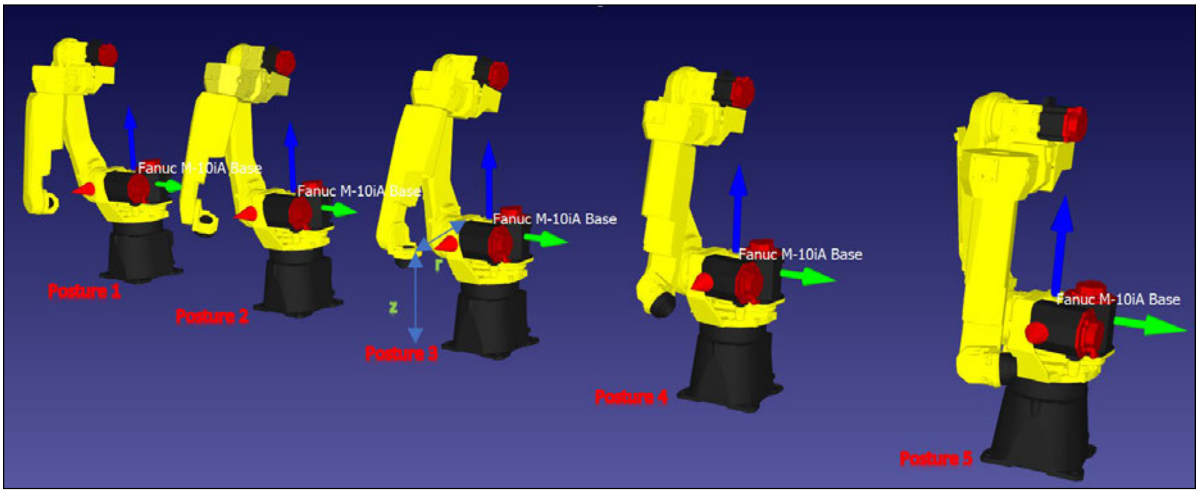

Figure 8-17: Dexterous Postures at r_1 and z_2 = 500 mm

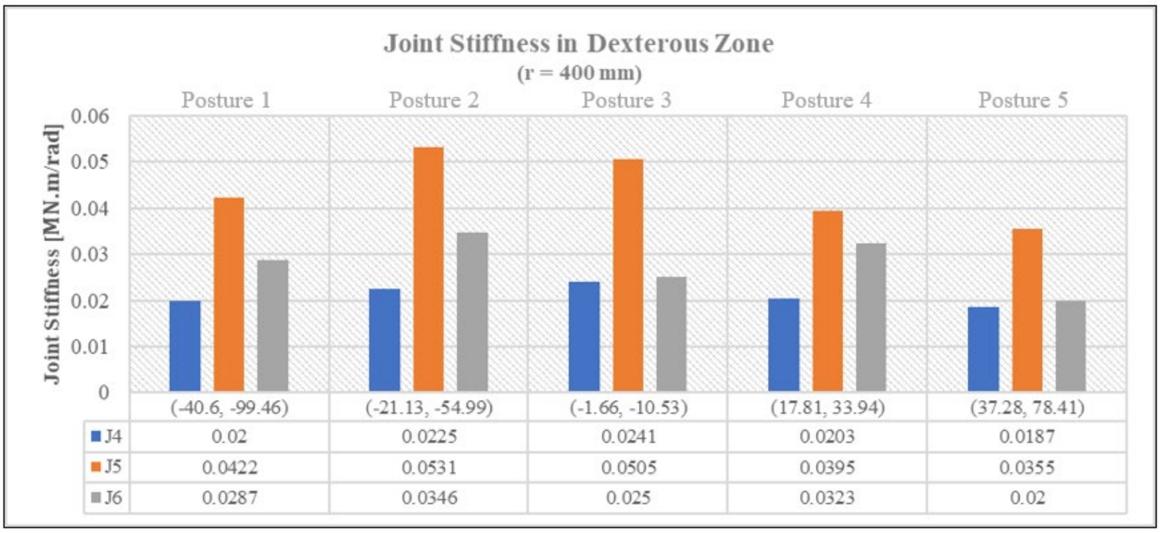

Figure 8-18: Dexterous Stiffness Results at r_1 and z_2 = 500 mm

As is evident in Figure 8-18 above (r_1) - posture 2 and posture 3 - documented the highest overall joint stiffnesses. This implies that within the dexterous range defined by $\beta\{\min, \max\} = \{-40.6, 37.28\}$ and $\alpha\{\min, \max\} = \{-99.46, 78.41\}$, the stiffest postures were recorded between $\beta\{\min, \max\} = \{-21.13, -1.66\}$ and $\alpha\{\min, \max\} = \{-54.99, -10.53\}$. Joints 5 and 6 had the highest stiffness at posture 2 of 0.0531 MN.m/rad and 0.0346 MN.m/rad, and posture 3 recorded the highest joint 4 stiffness of 0.0241 MN.m/rad. Postures 1 and 5, at the extremity of the dexterous zone, for r_1, r_3 and r_5, generally recorded the lowest stiffnesses. This was possibly due to the perpendicular alignment of links 3 and 4 at these configurations.

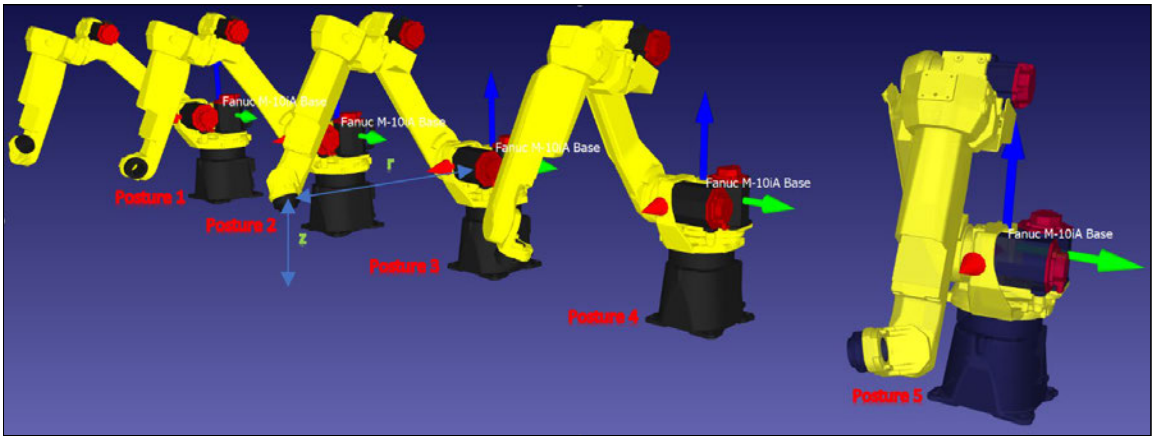

Figure 8-19: Dexterous Postures at r_3 and z_2 = 500 mm

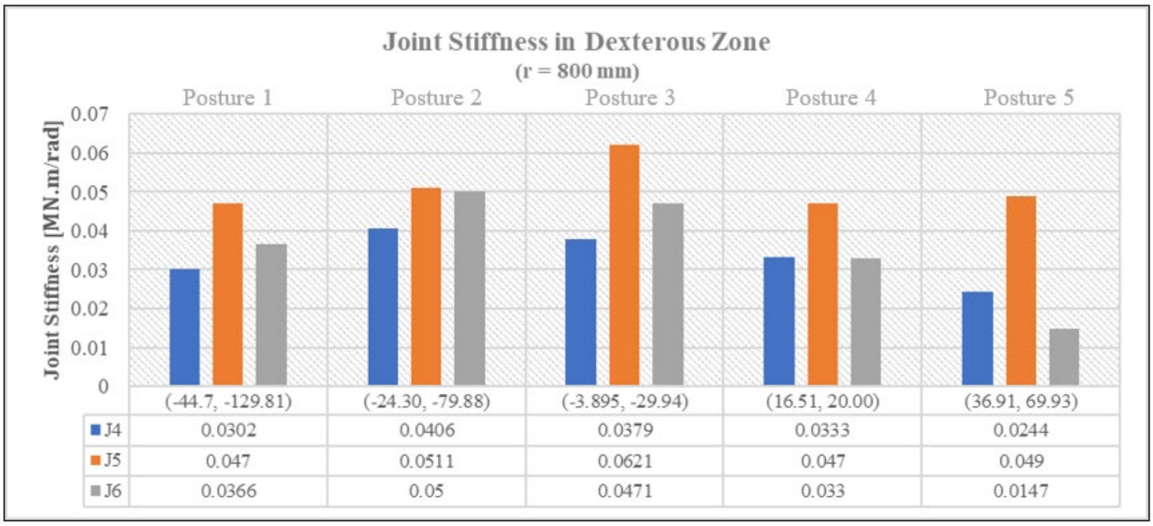

	(-44.7, -129.81)	(-24.30, -79.88)	(-3.895, -29.94)	(16.51, 20.00)	(36.91, 69.93)
J4	0.0302	0.0406	0.0379	0.0333	0.0244
J5	0.047	0.0511	0.0621	0.047	0.049
J6	0.0366	0.05	0.0471	0.033	0.0147

Figure 8-20: Dexterous Stiffness Results at r_3 and z_2 = 500 mm

As indicated in Figure 8-20 above, a similar trend in stiffness occurred with postures 2 and 3 being the highest, and 1 and 5 being the lowest. The β *and* α ranges were higher at r_3 compared to r_1. The maximum β *and* α range at r_1 was $-77.88°$ and $177.87°$, respectively, compared to r_3, where the range for β *and* α was $81.61°$ and $199.74°$, respectively. These results were expected since there was a greater variety in configurations that were possible towards the centre of the workspace, as opposed to when the links were contracted (r_1) or when the robot was fully extended (r_5). The dexterous range was defined by $\beta\{\min, \max\} = \{-44.70,\ 36.91\}$ and $\alpha\{\min, \max\} = \{-129.81, 69.93\}$. The stiffest postures were recorded between $\beta\{\min, \max\} = \{-24.30, -3.895\}$ and $\alpha\{\min, \max\} = \{-79.88, -29.94\}$. Joints 4 and 6 had the highest stiffness at posture 2 of 0.0406 MN.m/rad and 0.0500 MN.m/rad, respectively, and posture 3 recorded the highest with joint 5's stiffness measuring 0.0621 MN.m/rad.

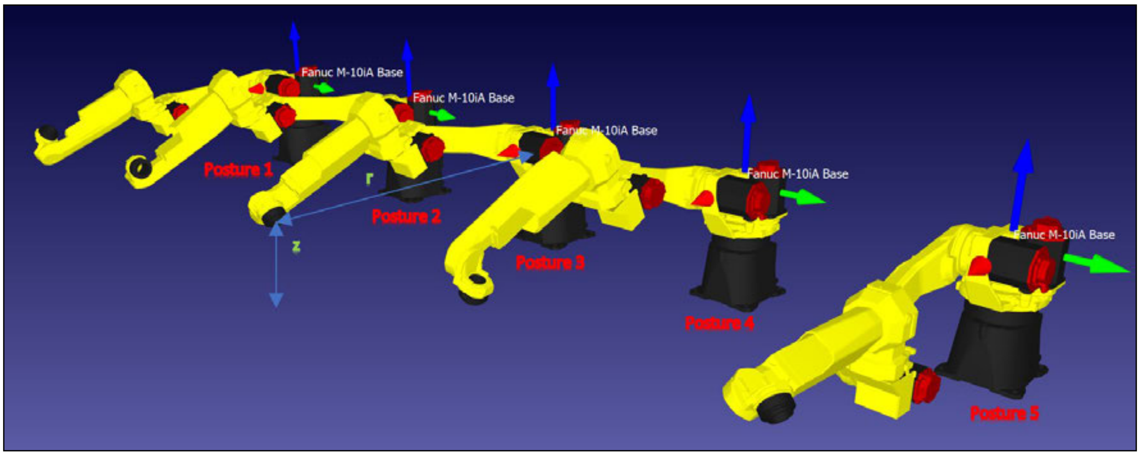

Figure 8-21: Dexterous Postures at r_5 and z_2 = 500 mm

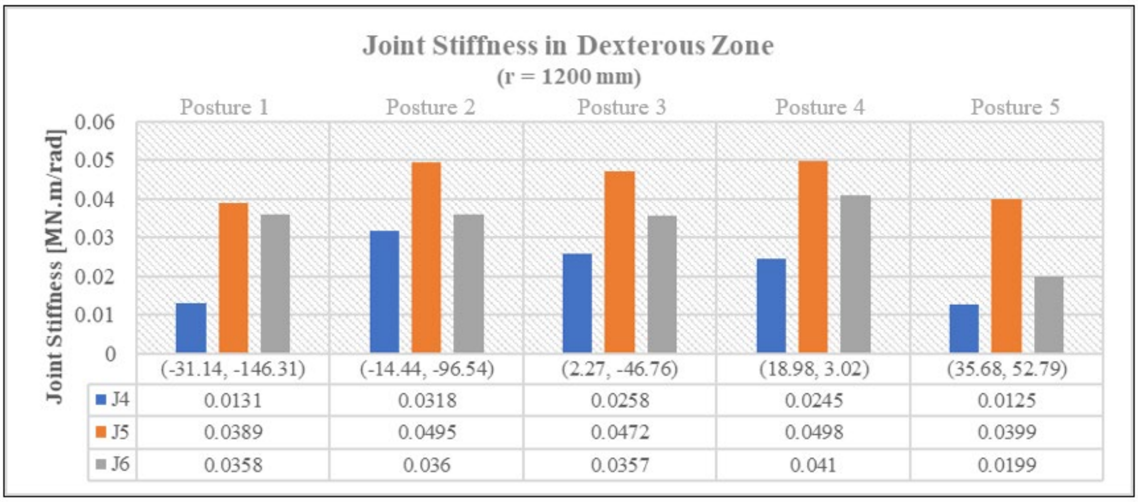

Figure 8-22: Dexterous Stiffness Results at r_5 and z_2 = 500 mm

Then, shown in Figure 8-22 above, postures 2, 3, and 4 had the greatest stiffnesses, and again, postures 1 and 5 were the lowest. The dexterous ranges were defined at $\beta\{\min, \max\} = \{-31.14,\ 35.68\}$ and $\alpha\{\min, \max\} = \{-146.31, 52.79\}$. The stiffest postures were between $\beta\{\min, \max\} = \{-14.44, 18.98\}$ and $\alpha\{\min, \max\} = \{-96.54, 3.02\}$. Although the robot was almost fully extended at r_5, the possibility of stiffer configurations was proven.

Overall, for each dexterous zone, joint 5 approximated as the stiffest of the end-effector joints, followed by joint 6, and then joint 4. As the end-effector moved further away from the base of the robot, the joint stiffness decreased. These results have been consistent throughout the non-dexterous and dexterous tests. In addition, r_1 possessed the highest stiffness at postures 2 and 3, and overall, was the stiffest compared to all other radial distances. Since adjacent postures had the highest joint stiffness, it can also be said that other configurations that lie within the range of postures 2 and 3 at r_1 and r_3, and postures 2, 3 and 4 at r_5 have high stiffnesses. Throughout each dexterous analysis, the stiffness was lowest at the extremities of the dexterous zones (postures 1 and 5). Although these values were lower at each distance (r_1, r_3 and r_5), the end-effector joint stiffness was still improved, compared to the joint stiffness recorded during the non-dexterous tests.

To explain further, Table 8-4 below displays the estimated measured and calculated joint stiffness values, the errors, percentage (%) error of the mean, and the joint stiffness percentage (%) improvement by radial distance. For the non-dexterous tests, 5 radial distances were tested (r_1 to r_5), and for the dexterous tests all odd radial distances were tested (r_1, r_3 and r_5). The overall joint stiffness decreased from r_1 through to r_5. The result was expected as the robot entered a cantilever like posture, as the end-effector moved away from the robot.

Moreover, the errors for each stiffness variable shared a normally distributed relationship. The primary sources of errors that were reported during the experimental procedure include the sensitivity of the PCB accelerometers ($\pm 10\%$ 100 mV/G or 10.2 $\mathrm{mV/m/s^2}$); the conversion to displacement, which approximated to a 0.1 mm difference between measured deflection and calculated deflection; the sensitivity of the S-Type load cell ($\pm$ 0.01 kg); the error in the servo-joint of the robot ($\pm$ 0.05°); and finally, the consistency in applying the wrench onto the torque tool.

To test the repeatability of the VJM approach, an additional 9 tests per radial distance for both dexterous and non-dexterous tests were performed. The deflection errors were evaluated as a percentage of the mean deflections across all joints. Table 8-4 displays the errors recorded during the non-dexterous tests, which ranged between 1% and 32%. The errors during the dexterous tests ranged between 4% and 23%. The results that were recorded were acceptable, considering the sensors and robot applied in the research.

Table 8-4: Estimated Joint Stiffness Values for Non-Dexterous and Dexterous Tests [MN.m/rad]

Radial Distance	Joint Number	Estimated Joint Stiffness Values						Stiffness Percentage Improvement
		Non-Dexterous			Dexterous			
		Measured [MN m/rad]	Error [MN m/rad]	% of mean	Measured [MN m/rad]	Error [MN.m/rad]	% of Mean	
r_1	1	16.840	±3.02	±18%	18.310	±2.12	±12%	9%
	2	7.300	±0.97	±13%	8.120	±1.40	±17%	11%
	3	11.570	±1.07	±9%	12.120	±1.62	±13%	5%
	4	0.016	±0.0035	±22%	0.0211	±0.0017	±8%	32%
	5	0.035	±0.0079	±23%	0.0442	±0.0043	±10%	26%
	6	0.016	±0.0019	±12%	0.0281	±0.0035	±12%	76%
r_2	1	15.030	±2.4800	±17%				
	2	10.530	±2.7200	±26%				
	3	7.060	±0.9000	±13%				
	4	0.021	±0.0012	±6%				
	5	0.050	±0.0159	±32%				
	6	0.022	±0.0088	±28%				
r_3	1	13.900	±2.31	±17%	15.560	±1.22	±8%	12%
	2	6.790	±0.04	±1%	7.970	±0.36	±5%	17%
	3	5.120	±0.39	±8%	5.840	±0.22	±4%	14%
	4	0.020	±0.0021	±9%	0.0330	±0.0012	±4%	38%
	5	0.050	±0.0027	±6%	0.0512	±0.0019	±4%	2%
	6	0.032	±0.0021	±7%	0.0363	±0.0052	±14%	13%
r_4	1	13.500	±0.8000	±6%				
	2	4.250	±0.9200	±22%				
	3	5.660	±1.0500	±19%				
	4	0.022	±0.0029	±13%				
	5	0.043	±0.0100	±23%				
	6	0.040	±0.0022	±6%				
r_5	1	6.790	±1.5300	±23%	8.070	1.7100	±21%	19%
	2	3.580	±0.8900	±25%	3.710	0.3200	±9%	4%
	3	2.770	±0.4800	±17%	2.520	0.5900	±23%	-9%
	4	0.010	±0.0008	±8%	0.0215	0.0018	±8%	115%
	5	0.017	±0.0007	±4%	0.0451	0.0044	±10%	165%
	6	0.041	±0.0031	±8%	0.0337	0.0062	±18%	-18%

The joint stiffness values increased for most joints in the dexterity tests. For r_1 – joint 1 stiffness was 18.310 ×10 MN.m/rad, whereas in the non-dexterous tests, the stiffness recorded for r_1 was 16.840 ×10 MN.m/rad – a 9% improvement. Joint 2 (shoulder) increased by 11%, from 7.300×10 MN.m/rad to 8.120×10 MN.m/rad. For joints 3 and 4 (elbow), the stiffnesses increased by 5% and 32%, respectively. Finally, the wrist (joints 5 and 6) increased in stiffness by 26% and 76%, respectively. The results showed that the points closest to the robot's base possessed high stiffness with smaller deflections and rotations. The overall joint stiffnesses gradually decreased with increased deflections and rotations as the end-effector moved away from the robot's base (confirmed in Figure 8-11, Figure 8-12, Figure 8-13, and Figure 8-14). For r_5 – although for joints 3 and 6 stiffness decreased, for joints 1, 4 and 5 the joint stiffnesses measured the highest performances of 19%, 115%, and 165%, respectively. Three possible reasons for the decrease in stiffness for joints 3 and 6 are: 1) measurement inconsistencies during the deflection and rotation testing; 2) sensitivity of the accelerometers to noise, and the post-processing of the data from acceleration to displacement; and 3) unpredictability of the robot joint motion at r_5, since the robot entered a cantilever position.

Table 8-5 shows the average estimated joint stiffnesses recorded for all tests, and the average joint stiffness percentage (%) improvement.

Table 8-5: Average Estimated Joint Stiffness for Non-dexterous and Dexterous Tests

Average Estimated Joint Stiffness Values			
Joint	**Non-Dexterous [$\mathbf{MN.m/rad}$]**	**Dexterous [$\mathbf{MN.m/rad}$]**	**Stiffness Percentage Improvement**
1	13.212	13.980	6%
2	6.490	6.600	2%
3	6.436	6.827	6%
4	0.018	0.0252	40%
5	0.039	0.0468	20%
6	0.0300	0.0327	9%

In addition, the robot's first joint, located on the base, measured the highest stiffness with an average estimated joint stiffness value of 13.212 $\mathrm{MN.m/rad}$ during the non-dexterous tests and 13.980 $\mathrm{MN.m/rad}$ during the dexterous tests, a 6% increase. The robot's base is heavily reinforced and firmly mounted, resulting in the expected high stiffness. Joints 2 and 3 are linked to the robot's base through link 2 and share comparable stiffness values. Joint 2 recorded an average joint stiffness improvement of 2%, and joint 3 increased by 6%. These joints were not significantly improved since the magnitude of the applied force on the end-effector had a minimal effect, and as a result, the focus of the results are mostly on the end-effector joints. Joints 4, 5, and 6 were the main joints affected by the applied wrench force on the end-effector. These joints recorded the largest stiffness improvements of 40%, 20%, and 9%, respectively.

The aim of this section was to present and clarify the experimental results. Expanding on these findings, the following section looks at the application of the dexterous posture and stiffness identification technique and the results thereof.

8.6 Application of the Static Point Posture Identification Approach and Study Results

The research presented a simple, user-friendly, cost-effective dexterous posture identification approach and procedural stiffness methodology to determine stiff areas and postures within the Fanuc M10-iA's workspace. Although the obtained results are specific to the Fanuc robot itself, other robots within its class that share similar mechanical structures and joint configurations might obtain similar stiffness trends. The study investigated by *Dumas et al.* [107] recorded a similar joint stiffness trend, with joints 1 to 3 being the stiffest, and joints 4 to 6 being the weakest. In their research, a KR-240-2 belonging to the KUKA robot family was analysed. As far as prismatic joints and universal joints are concerned, the dexterous methodology could work, since the dexterous equations can be geometrically obtained using the IK approach, and depending on the type of robot and its structure. However, for the joint stiffnesses, most VJM studies have been applied to rotary joints. Therefore, additional mathematical transformations of the VJM parameters might be required to ensure that the model is fit for the stiffness estimation.

In any manufacturing event, robot applications either involve the links of the robot being stationary, and the tool dynamically operates, or the robot links move, and the tool remains static, or both. In all instances, the tool is attached to the end-effector, and therefore, the robot posture and placement of the end-effector are pivotal to ensure the robot's best elastostatic and kinematic performance. Based on the research findings of the static point posture identification approach, applications in which this research, as well as the results, can be applied to, in terms of tasks that require greater joint stiffnesses, include, but are not limited to, machining processes, such as drilling, tapping, and other high contact force operations. Before these analyses investigated in this research can be applied, the machinist or roboticist would be required to first analyse the robot intended for an application and ensure that the robot meets the design criteria requirements discussed at the beginning of this chapter. Secondly, a point cloud in the workspace should be setup by locating virtual points close to the robot base and points towards the boundary to understand and test the stiffness performance of the robot. Then, lastly, the dexterous postures can be geometrically identified, and the joint stiffness can be analytically determined by following section 7.3.

So far, the application has been discussed from the robot stance; however, in most practical applications, and depending on the availability and restrictions on robot workspaces in a manufacturing setting, some, if not the majority of robot applications are task placement dependent. This means that most processes are performed on dedicated worktables and tilt tables fixed within the manufacturing line. For example, at car production facilities, the robots are fixed on either side of the conveyor system and are required to reach out at prescribed distances to manipulate and fit the car parts. When placing the worktable, other considerations include safe working distances, for instance, where humans can reposition or realign parts while the robot moves. This implies that not every robot can operate close to its base. While this research focused on identifying stiffer areas, the advantage of the developed dexterous posture identification method was that although joint stiffness is posture and position-dependent, it is still possible to identify optimal postures with improved stiffnesses even at the workspace boundary. With this being said, the methodology can work at any user-defined point. The only factor that will distinguish low stiffnesses to high stiffnesses will be the selection of the robot posture. Additionally, this research also promotes further investigation into workpiece placement for optimal robot placement, which has been studied by a number of researchers [7, 138-140, 174]. As an example, the importance and effect of optimal workpiece placement is depicted in Figure 8-23 below:

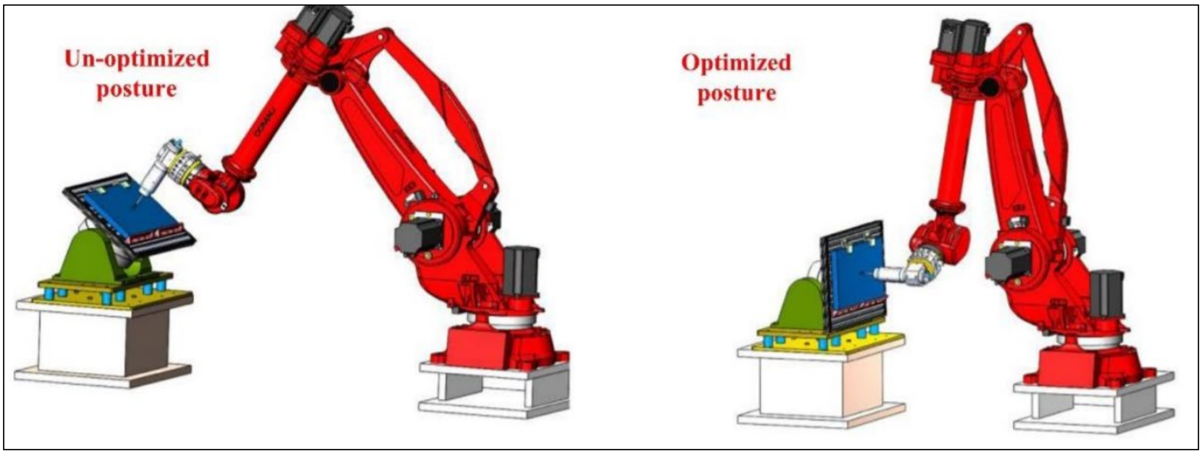

Figure 8-23: Workpiece Placement for Optimal Robot Positioning [141]

In cases where a user possesses the same robot analysed in this study, or even a similar robot belonging to the Fanuc class of robots, the following observations from this study may be useful: The joint stiffness results, both in and out of dexterous zones, showed that the end-effector at distances of 800 mm and closer to the base, possessed the greatest stiffnesses, as opposed to distances greater than 800 mm. The joint stiffnesses tested towards the Fanuc's workspace boundary had the lowest stiffnesses due to the cantilever structure of the links. These results were expected due to the irregular kinematic characteristics at the workspace boundary. The joint stiffnesses that were recorded by posture showed that postures 2 and 3 possessed the greatest stiffnesses at r_1, r_3 and r_5.

Furthermore, the robotic kinematics and stiffness matrices can be evaluated and applied to more dynamic conditions. The high joint stiffness points, areas, and postures can be used to map stiff robot trajectories, which ultimately extends the research application to dynamic machining operations that are not limited to milling, painting, cutting, polishing, and deburring. Other focus areas include hybrid manufacturing using robots whereby the robot can synergistically combine two or more manufacturing processes into one operation. This includes robot deposition processes, pick-and-place operations, and robot machining processes that are all possible with one tooling fixture. For example, the applied loads on the robotic system from hybrid manufacturing processes include the weight of the tool, or object being carried, and the high contact forces of the machining process. As a result, such hybridisation requires good kinematic and elastostatic performance, which can be realised upon applying the systematic approach investigated in this study.

A discussion of the results follows next.

8.7 Discussion of Results

This section presents a summary of the stiffness results based on the posture identification approach. Included is a discussion of the accelerometers as an alternative to deflection testing, the two testing phases, joint stiffnesses, sensitivity of the stiffness results, and shortfall of the VJM approach. This research explored the stiffness identification of an SKM at multiple postures about a coordinate system of points. The unique combination of the VJM and dexterity analysis defined the optimal areas and postures within the robot's reachable workspace that possess high kinematical properties. The process of applying 1-D springs to model the joint stiffness instead of modelling the complicated actuated joints of the robot, combined with the IK approach, provided a powerful tool to advance SKMs towards tasks that have a high force requirement.

The use of accelerometers as a displacement measurement tool provided a cost-effective, easy setup, and reliable alternative to laser trackers (addressing Objective 5 of this study). Although the accuracy of accelerometers is lower compared to laser trackers for deflection measurements, they fell within the budget allocated for this research and were reliable enough for the stiffness estimation, based on the regression analyses.

Two testing phases validated the dexterous posture identification technique. The first phase involved a general joint stiffness identification of the robot at multiple equidistant points in the workspace. This phase was defined as non-dexterous testing since the end-effector was fixed in the -z-direction for all tests. Although dexterity was not considered, optimal points with high stiffnesses were located within proximity to the robot base. The second phase, the dexterous tests, involved adjusting the posture of the robot and end-effector about the same equidistant points, and demonstrating the effect that posture has on the stiffness of the Fanuc robot.

The results displayed during the dexterous manipulation showed an improvement in the joint stiffness values. The IK approach determined the dexterous range by specifying the end-effector's coordinate position as the input. The dexterous formulation provided possible $\beta \; and \; \alpha$ configurations that define the dexterous space around a specific point in the robot's workspace. The geometrical nature of the method considered the link lengths of the robot and was able to develop a dexterous zone that defines all possible configurations at a point within the robot's workspace. The validity of the dexterity analysis was confirmed as multiple postures were analysed and identified as stiffer compared to the non-dexterous tests.

For both testing phases, joint 1 of the Fanuc M10-iA robot was the strongest, whereas joint 6 was the weakest. Other works that recorded joint 1 to be the stiffest and joint 6 to be the weakest was Berntsen *et al*. [155] and, Dumas *et al.* [107], whereas Li *et al.* [145] estimated joint 1 to be the weakest and joint 8 to be the strongest. This suggests that joint stiffness values are based on the kinematics and structure of a robot. The deflection results improved by 46% during the dexterous results, and the rotations improved by 16% in the x-axis, the y-axis improved by 42%, and the z-axis improved by 28%. The stiffest areas were located at r_1 and r_3, since these areas recorded the lowest deflections and rotations. Optimal dexterous ranges with high stiffnesses were provided. Overall, the stiffness of the Fanuc M10-iA robot was improved during the dexterous test, by the application of the dexterous posture identification method proposed in the study. The end-effector (joints 4, 5 and 6) were primarily the focus of the analysis since these joints bear the high applied forces during advanced manufacturing operations.

To analyse the sensitivity of the results to measurement errors, all limitations governing each test were investigated. Although the use of accelerometers provided a cost-effective alternative to the laser tracking device, the process of converting the acceleration signals to displacement introduced errors. A least-squares polynomial fitting algorithm was applied to remove the DC bias involved in the integration of acceleration. The method was able to offset most of the bias due to integrating the raw acceleration values to displacement.

The shortfall in the VJM analysis is that the method assumes the links to be infinitely stiff and only the joints compliant. A further investigation was performed to analyse the effect of the link deflections on the overall end-effector deflection. The contributions were moderate; however, a more accurate stiffness model can be obtained with their inclusion.

The integration of an optimisation problem that combined the singularity analysis with the dexterous analysis would have promoted far more testing points, thereby improving the accuracy of the VJM approach. The contribution to environmental effects, such as ground movement, wind, and electrical interferences that could not be controlled, would have skewed the results. To further improve the accuracy of the results, especially using accelerometers, an isolated, vibration-proof room would prove beneficial, facilitate the repeatability of the stiffness measurements, and reduce the measurement errors and results.

Overall, based on the theory in Chapter 2, and as demonstrated by testing in dexterous zones, an optimal robot configuration contributes to the stiffness characteristics of a robot. The dexterity analysis also demonstrated that for dedicated tasks that are manufactured at the extremities of the robot, whether intentional or not, stiffer robot postures are still possible.

A brief summary of the main points of the chapter are provided next.

8.8 Chapter Summary

This chapter was dedicated to the experimental procedure and physical testing results, to help, partially achieve Objectives 1, 2 and 3, which were to *research, establish and develop a dexterous posture identification method that can localise multiple configurations at a user-defined point; research, develop and simulate the workspace and singularities of the Fanuc M10-iA and understand their influence on the dexterity and stiffness analyses;* and *research, establish and identify a suitable stiffness modelling approach,* respectively. Additionally, this chapter was able to fully meet Objectives 4, 5, 6 and 7 of this study, which were to: *develop a systematic approach to the stiffness identification algorithm such that any roboticist can universally adopt it research, identify and implement a cost-effective, reliable and robust displacement sensor; research, design, construct and implement a suitable testing ground to test the workspace, singularity, dexterity, and stiffness model;* and *research, plan and execute a series of tests and methods of data collection and analysis to validate the effects of the dexterous posture identification technique on the stiffness modelling of the Fanuc M10-iA*.

The testing process was divided into two parts, centred around stiffness identification both in and out of dexterous regions. Both testing procedures were analysed, and the results were documented with necessary conclusions drawn from each test. The key observations include:

- The workspace and singularity analysis significantly improved the effectiveness and efficiency in which to localise each testing point. The workspace formulation accurately modelled the end-effector reachability points, and the singularity analysis was able to locate most of the unreachable points.

- The VJM technique was able to define the joint stiffnesses through its simplified method and formulation, with errors below $\pm 32\%$ for the non-dexterous tests and $\pm 17\%$ for the dexterous tests, thereby confirming the repeatability and accuracy of the stiffness measurements. Although the sensitivity of results to measurement errors was controlled, most errors were attributed to the conversion of acceleration to displacement, the inconsistency of the applied wrench, and environmental noise.
- The benefit of the VJM technique is its simplicity and easy application to all revolute SKMs.
- The major drawback of the VJM was its inability to include link stiffnesses, and as a result, it was difficult to model the measured joint stiffnesses. Link 4, the second-longest of the links, with its cantilever effect when fully extended, contributed 11% to the end-effector displacement.
- The conversion of acceleration to displacement using accelerometers provided a reasonable and cheaper alternative to laser trackers.
- The result recorded during the non-dexterous tests demonstrated stiff points that were located close to the robot base (400 mm). As the end-effector gradually shifted away from the robot base, the joint stiffness decreased. As expected, the cantilever effect with the arm fully extended recorded the highest deflection and lowest stiffnesses.
- The dexterous tests were performed by manipulating the robot posture about user-defined points specified by the testing point setup shown in Figure 8-9. The IK solution was able to locate optimal postures defined by alpha, beta, and gamma values. Gamma was set to zero for each test since no obstacle avoidance was considered. This was confirmed in the research performed by Mondragon [106].
- During the dexterous tests, joints 1, 2 and 3 had moderate stiffness improvements, whereas the end-effector stiffness, comprising joints 4, 5 and 6, was improved.
- Postures 2 and 3 possessed the highest joint stiffnesses at r_1, r_3 and r_5. The joint stiffness results by radial distance coincided with the non-dexterous tests, in that the joint stiffnesses worsened the further the end-effector moved away from the robot base.
- The dexterous results coincided with the non-dexterous tests, confirming that stiff points and configurations lie within proximity (at r_1) from the robot's base.

The next chapter offers a synthesis and discussion of the main findings of the study.

9. DISCUSSION

9.1 CHAPTER INTRODUCTION

The primary objective of this research was to *improve the stiffness of serial robotic arms through the analysis of a dexterous posture identification technique*. This chapter presents the findings, observations, results, and insights into the research in line with the project's aims and objectives presented in Chapter 1 (section 1.4). The layout of this chapter is as follows. This chapter begins with a review of robotic markets and trends (section 9.2). Based on this review, the importance and relevance of this study are justified. Also discussed are workspace and kinematic singularity analyses (section 9.3); dexterous analysis (section 9.4); stiffness modelling and identification (section 9.5); physical testing, results, and performance (section 9.6); and implications of the research and the future of machining (section 9.7). Following the multivariable analyses preceding the stiffness improvement that is discussed, a brief conclusion (section 9.8) is provided based on the implications of the research on the robotic market.

9.2 ROBOTIC MARKET AND TRENDS

The discussion here begins with a reflection on the machine industry market and current trends. Robotics is rapidly entering new and smart industries, with the oldest and most used cases being the manufacturing markets. The uses of robots were mainly typical pick-and-place operations. However, today's markets are noticing the increased use of machine learning, vision recognition, collaborative robots, and failure prediction, all of which have enhanced robotic capabilities and revolutionised manufacturing processes [1]. Robot sales escalated rapidly between 2009 and 2017, from 60,000 to 381,000 annually (26% CAGR) [16, 17]. The main players behind this increase are the automotive industries, with the consumer-electronics industry following closely behind. These industries combined occupy two-thirds of total robot sales, with China being the largest consumer [19]. As seen in Figure 9-1, the future growth prediction of robotics will see massive growth, both in China and worldwide. Thus, we can see that not only is the robotic market experiencing massive growth and transformation, but it also has the potential to positively transform our lives and work practices. This further substantiates the necessity for this research.

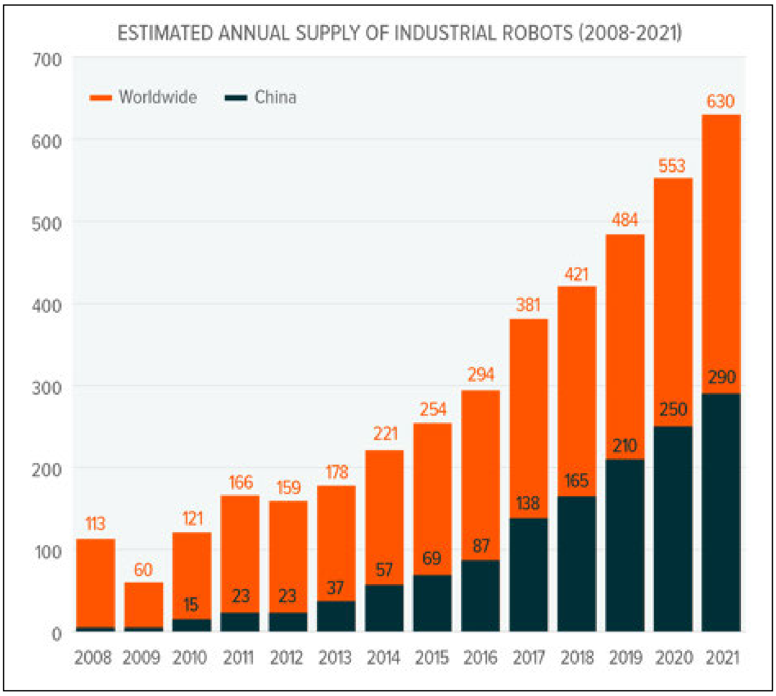

Figure 9-1: Growth of Industrial Robotics Worldwide and in China (Thousands) [17]

The industrial robot can mass manufacture goods due to its repetitive nature. The SKMs ability to autonomously manipulate parts, place the part, and perform the operation, whether it be deburring, drilling, sanding, or painting, has increased its favourability and popularity in the manufacturing environment. The only human intervention required is to close the drawer to trigger the process, which is the machine's safety requirement [10].

The design of any part is conditioned by the type of manufacturing process required and the total working envelope. Although CNCs may broadly offer the former, they lack the workspace. This is where SKMs can be used as an alternative, therefore affirming the need for the various analyses conducted in this study. Apart from providing larger working volumes, SKMs feature flexible kinematics, allowing various part sizes and complexities to be machined. In addition, their speeds and repetitiveness can deliver mass production timeously [6, 10, 48].

However, according to Pan *et al*. [61], the biggest downfall that SKMs face is the end-effector deflection due to high interaction forces on different hardness graded materials. This is partly due to the inherent low stiffness of SKMs, which is usually below 1 N/µm. On the contrary, the CNC machine exhibits stiffness well over 50 N/µm. Poor surface quality has hindered machining and precision manufacturing tasks with serial robots because of their force-induced deformations at the tooltip.

Recalling from Carbone [36] and Yoon [109], three factors define "robotic stiffness" – *joint stiffness, robot configuration*, and *applied forces*. The joint stiffnesses are usually fixed as they form part of a robot’s characteristics. Thus, to maximise any robot’s stiffness, the only variable that can be adjusted is its posture. Various studies concur with this principle, including that of Celikag *et al.* [23] and Schneider *et al.* [5]. These authors developed two methods to select optimal measurement poses for joint stiffness identification, in which valuable insight and information were extracted for this research.

Due to the serial kinematic structures of SKMs, their dynamic and static properties are mostly configuration and orientation dependent. This analysis was confirmed by several studies [5, 24, 58, 63]. Based on this evidence presented in the literature review in Chapter 2 on the low apparent stiffness of SKMs, this research provided a straightforward, low-cost dexterous posture identification method to improve the stiffness of SKMs, achieving Objectives 1, 2, 3, 5, 6 and 7 of the study. Any manufacturer or roboticist can universally adopt this method to optimise their robot postures, realising Objective 4 of this study. The research outcome was to improve the stiffness, accuracy, and repeatability during precision and high loading manufacturing tasks.

Further motivation to apply the dexterous posture method was attributed to the simple concept of - stress and deflection being linearly related. The highest stress in the robot’s structure is distributed to the higher load-bearing elements, such as the robot joints, end-effector, and tool. By locating optimal postures, this regulates the induced stresses throughout the robot’s structure, thereby improving the process accuracy and repeatability, enhancing the robot's validity and reliability for manufacturing tasks involving high applied forces. The accuracy and repeatability aspects are quantifiably pitched in terms of the magnitude differences in the end-effector deflection, which was proven based on the results obtained in both non-dexterous and dexterous tests.

Apart from the improved stiffness performance offered, the future benefit of the method advances the robot's longevity and minimises the regular robot maintenance that is often required due to excessive loading and stress and strain on the robot motors, joints, and links.

Another point of focus was on robotic workspace and singularity. Although discussed in more detail in the next section (9.3), for now, it suffices to mention that these analyses provided conclusive end-effector positions in which to test the stiffness. It was imperative to understand the nature of the workspace and the Fanuc robot's singularities, as it was only through this understanding that a well-defined point cloud was developed.

From the above analyses and use of a reliable testing methodology, both concepts – the VJM for the stiffness identification and the dexterity using the IK method – were able to prove that robotic stiffness is posture dependent and determining stiff areas and postures can improve the kinematic characteristics of a serial linkage robotic arm. This research partially addressed Objectives 1, 2 and 3 of this study.

9.3 WORKSPACE AND KINEMATIC SINGULARITY ANALYSES

The workspace formulation and analysis for the Fanuc M10-iA provided an opportunity to understand the workspace available for testing; this was crucial as all testing points had to cater to both non-dexterous and dexterous points. As indicated in the literature review in Chapter 2, many scholars, including Nawaz et al. [15] and Laseinde et al. [18] have verified that workspace and boundary identification are pivotal for end-effector placement in an environment, dexterity, and operational efficiency. Other researchers, including Laseinde *et al.* [18] and Palandrani [19], Murphy [20], Coetzee [21], Xaud [22], and Celikag *et al.* [23] have studied characteristics such as singularities, stiffness, and manipulability through workspace analysis. Additionally, these authors validated the importance of workspace, and kinematic singularity identification in any robot study. The idea of analysing the workspace was to understand to what extension of the robot can tests be performed, as it is well-known that many robotic structures exhibit unstable motion at the boundary due to their kinematical structure and joint limitations. Consequently, the developed coordinate system was developed by analysing the reachable workspace of the Fanuc robot obtained via the workspace MATLAB® results. All testing points were positioned to test the best and worst cases for the stiffness analysis.

The forward kinematic solution applied the D-H method using a point cloud technique. The mathematical model required the joint type and D-H parameters (determined in section 4.2) as input into the model. Based on the preliminary inputs, the model was able to output the 3-D workspace successfully.

The overall workspace shown in Figure 4-2 showed a spherical topology of the robot. This was confirmed as joint 1's limit ranged between -360 degrees to +360 degrees. Each point represented reachable points by the end-effector. The technique applied all joint coordinates of the robot so that an accurate representation of each reachable point was displayed. Each orthographic workspace view occupies empty voids. This was because the entire physical volume was computationally challenging to obtain. Other authors who have cited similar workspace topologies include Aggarwal *et al*. [89] and Gudla [172].

The computational requirements probed each step size of (n^{10}) joint configurations, of which each had to pass through the forward kinematic solution. For this research, step sizes ranging from (n = 4 to n = 6) were tested. The best result was obtained at n = 6, as the model was able to capture the overall workspace better; this implied that 6^{10} joint configurations were computed. Aggarwal *et al*. [89], concurred by applying the same step size to model the robot in their research. The entire reachable workspace increased closer towards the centre axis (X = 0, Y = 0) and decreased further away, which was expected as the reachable points are far higher towards the centre and decrease gradually towards the boundary. This was also confirmed during the dexterous analysis since the robot struggled to achieve some configurations at r = 400 mm (r_1) and at r = 1,200 mm (r_5). At points located between r_1 to r_3, the robot was able to attain multiple configurations, again confirmed during tests performed at r_2 to r_3. From the workspace top view (Figure 4-3), a central void located at (0,0) represented the volume of space occupied by the robot. The empty voids were due to the step size of 10 that was chosen. As the step size increases, the voids would decrease, but at the expense of computational time and effort. According to the robot's maximum reachability of 1,420 mm, the simulated reachability was -1,412 mm and +1,412 mm in the X-axis and -1,412 mm and +1,412 mm in the Y-axis (Figure 4-3). The difference between the actual and modelled reachability can be attributed to the chosen step size of n = 6. Increasing the step size would have accurately modelled the reachable workspace, however, at a much greater computational effort and expense.

The singularity model was combined with the workspace model. The Jacobian matrix was dependent on the number of DOF of the robot – of size $6 \times n$, which in this case, was 6. The model to determine the singularities was developed by identifying the determinant of the Jacobian matrix subsets. In analysing the global workspace, two singularity types were identified: *forearm* and *wrist* singularities. These singularity types are popular in serial structures that have the first three DOF as the arm (forearm) and the last three DOF as the wrist. These singularities were also cited in similar studies [22, 95, 96, 154].

The results obtained from section 5.2.1 show that forearm singularities occurred when q_3 approached -2.838 radians or when q_2 and q_3 approached $-\frac{\pi}{2}$ and -1.268 radians, respectively (see equation [5-13] to [5-16]). The wrist singularity occurred when q_5 approached $-2\pi, -\pi, 0, \pi, 2\pi$ (see equation [5-17] to [5-19]). These results were similar to those obtained by Huag *et al.* [89] and Kang *et al.* [96]. The wrist singularities (q_5) for the Fanuc robot tested in Kang *et al*. [96] was 0 and π radians, as these were located within the robot's joint limits. In the case of the Fanuc M10-iA, (q_5), joint limit ranges between -2.11π and $+2.11\pi$, and hence a complete revolution, both clockwise and anti-clockwise, needed to be considered.

Singular configurations do not only occur at specific joint values, but rather as the joint approaches near or over the singular value. As a result, it was challenging to select a point in the workspace that would maximise the number of postures. It was noticed that the wrist type singularities occurred when the joint 4-axis became collinear with the joint 6-axis. Consequently, for the configuration tested during the non-dexterous points, joints 4 and 6-axes were close to 90 degrees to each other. In rare instances when the lowest radial distance was tested (z_1 = 100 mm), such wrist singularities did occur as it was not possible to prevent the almost collinear alignment of joints 4 and 6. Since similar postures about various equidistant points were tested, and for consistency, a wrench test was not performed if a singular point was reached. For the dexterous tests, at r = 400 mm and 1,200 mm – the wrist singularities occurred more frequently.

Based on the workspace and singularity analyses, the testing points were defined using a cylindrical coordinate system, as shown in Figure 8-9. The joint stiffness values were tested and compared by 25 points at equidistant arcs – starting at r = 400 mm (r_1), and thereafter each point located 200 mm away, up until r = 1,200 mm (r_5), giving 5 radial distances of testing points. As a result, the joint stiffness values were tested at 400 mm (r_1), 600 mm (r_2), 800 mm (r_3), 1,000 mm (r_4), and 1,200 mm (r_5) distances away from the robot base.

Apart from maximising the testing points, this testing configuration was developed for three other reasons, namely: (1) to create a trend analysis of the joint stiffnesses; (2) the VJM requires multiple testing points to arrive at an accurate solution; and (3) to test the repeatability of the VJM modelling approach. The setup of points assisted in identifying optimal points. The joint stiffness consisted of 125 testing points for the non-dexterous test and 45 testing points for the dexterous tests. This section detailed the workspace and singularity analyses and the findings thereof, thereby addressed Objective 2, and partially addressing Objective 6 of this study. The findings of the dexterous analysis are presented next.

9.4 Dexterous Analysis

The dexterity analysis was aimed at locating postures that have high joint stiffnesses. The method applied an Inverse Kinematic (IK) approach. The IK method was based on the theory that a solution exists, provided that the end-effector is within the reachable workspace and with the correct orientation. Thus, affirming the preceding workspace and singularity analyses. The technique applied Euler angles (α, β, γ) to define all possible orientations at a user-defined point in space. The approach of finding all possible orientations at a point is defined as *dexterity.* Graphically, such a concept can be understood by tracing a sphere with a radius equal to half the length of the manipulator's last link at the point. The imaginary sphere that was formed was called the *service sphere*. A service region was developed when the second-to-last robot joint workspace boundary intersected with the imaginary service sphere. This region housed all dexterous end-effector configurations defined in terms of alpha (α) and beta (β) values.

The dexterity analysis was tested over 5 configurations, starting closest to the robot base at (r_1), then at (r_3), and lastly, close to the workspace boundary (r_5).

Each point comprised of 5 different postures. In total, 45 postures were tested. The method of identifying the postures involved substituting the end-effector (x, y, z) coordinates and link lengths into each α and β equation described in section 6.2. The IK solution was numerically solved and calculated in Wolfram Mathematica.

A machining operation would rarely take place with the robot fully retracted. The workpiece is usually situated at reasonable distances away from the robot's base. Most machining applications have fixed workbenches with the workpiece firmly attached, such as the research performed by Qin *et al*. [7].

The dexterity results provided the dexterous postures at each testing point and were defined in terms of joint coordinates. The radial distance with the greatest dexterous range was able to attain more postures as opposed to a narrower range.

Further, the performance of the IK solution was verified as every posture within the dexterous zone was reachable. The limitation of the method was that the zones did not cater for possible singularities of the robot. As a result, and for consistency, no wrench test was performed if the posture was not attainable.

This section clarified what is meant by *dexterity* and focused on the dexterity analysis, and thereby partially addressed Objective 1 and 2 of the study. Attention now shifts to stiffness modelling and identification (Objectives 3 and 4), highlighting important findings that emerged from the research.

9.5 Stiffness Modelling and Identification

The stiffness approach was based on the work performed by Dumas *et al.* [107]. The stiffness identification applied the VJM. The method was based on the conventional rigid body model, where joints were assumed compliant and links infinitely stiff to amass every possible flexibility in the joints only. Geometrically, the method is equivalent to replacing the joints with auxiliary virtual joints with embedded virtual springs. The VJM technique offers a much better approximation of the joint stiffness values when compared to the FEA and MSA techniques, as confirmed by Pashkevich *et al*. [58], Tian *et al.* [63], Aggarwal *et al*. [89], Gudla [172], Xaud [22], Donelan [154], Kang *et al.* [96], Jha [95], Qin *et al*. [7], and Dumas *et al.* [107].

The components that were required to solve the model included: The Jacobian matrix with its inverse and transpose counterparts, joint coordinates, wrench force/torque matrix, and Complementary stiffness matrix (K_X) - if dexterity is not considered. These equations were required for the non-dexterous test. For the dexterous tests, all but the K_X matrix was required, as dexterity identifies cases where K_X is negligible with respect to K_θ. From equation [7-7], it was noted that the K_X is dependent on both K_c

and K_θ. By analysing K_c, it was noticed that formulating K_X was much simpler in dexterous zones, since equation [7-7] was reduced to [7-8]. These hypotheses were confirmed by Dumas *et al.* [107].

Equation [7-13] governed each test. Each test was accompanied with a 6-D wrench vector, a 6-D end-effector displacement vector, and an A matrix. The A matrix constituted of subdividing the Jacobian matrix and multiplying its equivalent positional wrench vector counterparts (refer to equation [7-12]). The goal was to test 25 points per radial distance. However, not all points could be reached due to singularities. Consequently, an equivalent B_i and c_i matrix was required (refer to equation [7-14]). It was further noticed that the linear system of equations (equation [7-13]) became overdetermined when $n > 1$. As a result, the method used to solve the system of linear equations applied the Left Moore-Penrose Pseudo Inverse method, which was able to solve the non-square matrices. The stiffness formulation was numerically evaluated in Wolfram Mathematica. The software was able to easily import the deflection and force data from Microsoft Excel, which was required for the calculation of the stiffness values, and graphically display the boxplots shown in section 8.5.

The shortfall of the VJM was that it assumed the links of the robot to be infinitely stiff. Consequently, as with other stiffness modelling techniques, only an approximation of the stiffness was provided. The research that focused on stiffness modelling and identification attended to Objectives 3 and 4 of this study.

Having focused on stiffness modelling and identification above, attention now shifts to the application, the results thereof, and an evaluation of the VJM performance.

9.6 Physical Testing, Results, and Performance

This section presents a discussion of the experimental process and results of the joint stiffnesses using the dexterous posture identification technique. This research explored the stiffness identification of an SKM at multiple postures about a user-defined point. The unique combination of the VJM and dexterity analysis was able to define the optimal areas and postures within the robot's reachable workspace that possess high kinematical properties. The process of applying 1-D springs to model the joint stiffness, instead of modelling the complicated actuated joints of the robot, combined with the IK, provided a powerful tool to advance SKMs to more high-force manufacturing tasks. The use of accelerometers as a displacement measurement tool provided a cost-effective, easy setup, and reliable alternative to laser trackers. Two testing phases validated the above combination of the two techniques. The first phase involved a general joint stiffness identification of the robot at multiple equidistant points according to the point cloud developed in Figure 8-9 and Figure 8-10. This phase was defined as non-dexterous testing since the end-effector was fixed in the -z-direction for all tests. The second phase, the dexterous tests, involved manoeuvring the end-effector about the same equidistant points, and demonstrating the effect that posture has on the stiffness of a robot.

The magnitude of the end-effector deflection was a governing variable in robotic joint stiffness analysis. Thus, the reliability of the software, deflection apparatus, and the robustness of the calculated model needed to be validated. All instances were investigated and analysed in this research (which addressed Objective 5).

LabVIEW and DIAdem provided a user-friendly and straightforward platform to visualise the acceleration signals in real-time, and later, to embed the least-squares polynomial algorithm. The software easily integrated all data acquisition devices, of which unique properties and processes could be modified, monitored, and controlled. The apparatus was carefully calibrated and tested according to manufacturing specifications. The S-Type load cell was tested by repeatedly loading calibrated weights supported on a hanger, to the module, and examining the variance in output force. Each PCB accelerometer was accompanied by calibration certificates, which specified the system sensitivity, resonant frequency, and output bias values.

To analyse the sensitivity of the results to measurement errors, all limitations governing each test were investigated. The errors for each stiffness variable shared a normally distributed relationship. The process of converting the acceleration signals to displacement introduced errors. The least-squares polynomial fitting algorithm to remove the DC bias involved double integrating the acceleration signals. Many studies have validated this algorithm as a feasible solution to correct the DC offsets [165, 166]. The end-effector deflections could have been measured using a laser tracker. These are high precision sensors that can measure up to a 100th of a millimetre and would have provided much accurate results, however, this device did not fall within the research budget. Other sources of errors include the sensitivity of the PCB accelerometers (± 10 % 100 mV/G or 10.2 $mV/m/s^2$). Although the use of accelerometers provided a cost-effective and reliable alternative to the laser tracking device, the conversion to displacement approximated to a 0.1 mm difference between measured deflection and calculated deflection, the sensitivity of the S-Type load cell was ($\pm$ 0.01 kg), the error in the servo-joint of the robot was ($\pm$ 0.05°), and finally, the consistency in applying the wrench onto the stainless-steel torque tool.

As previously mentioned, the stiffness values are reliant on the deflection values; therefore, the deflection values were validated against the calculated model. The calculated model relied on the initial and deflected HTM of the end-effector pose, and the difference between them provided the overall deflection (refer to equations [7-18]-[7-21]). For the non-dexterous and dexterous tests, the R-Squared values were acceptable for the joint stiffness estimation.

The repeatability of the VJM was tested by an additional 9 tests per radial distance. The stiffness errors were evaluated as a percentage of the mean stiffnesses, across all joints. Table 8-4 shows the errors recorded during the non-dexterous tests, which ranged between 1% and 32%. The errors during the dexterous tests ranged between 4% and 23%. The results that were recorded were acceptable, considering the testing instruments that were used.

According to the measured and calculated results, the lowest deflections occurred closest to the base, and the highest deflection occurred furthest away from the base. It was noted that the during the physical recording of the joint values after r_3, the robot joint settling times increased. As previously mentioned, this was due to the robot's intelligent electro-mechanical design and the self-correction ability of the servo motors. This also posed a challenge in acquiring the exact deflected coordinate value at these distances, which would have skewed the R-Squared percentages.

The results recording by averaging the estimated joint stiffnesses across each radial distance recorded the following stiffness percentage improvements: joint 1 improved by 6%, joints 2 and 3 improved by 2% and 6%, respectively, and joints 4, 5 and 6 improved by 40%, 20% and 9%, respectively. To further explain these average estimated joint stiffness results; during the non-dexterous and dexterous tests, joint 1 was the most rigid, with an estimated overall joint stiffness value of 13.212 MN.m/rad, and 13.980 MN.m/rad, respectively. The first reason to support this is that the robot is heavily reinforced at its base; therefore, a high stiffness value was expected. Secondly, due to the maximum applied loads of 55 to 60 N and proximity to the base, there was a minimal effect on the joint. The stiffness for both joint 2 and joint 3 was similar at 6.490 MN.m/rad and 6.436 MN.m/rad for the non-dexterous tests, and 6.600 MN.m/rad and 6.827 MN.m/rad for the dexterous tests, respectively. Again, these joints are both joined by link 3 through to joint 1 and are reasonably reinforced. The weakest joints were represented by 4, 5, and 6 with joint stiffnesses of 0.0180 MN.m/rad, 0.039 MN.m/rad, and 0.0300 MN.m/rad for the non-dexterous tests, and 0.0252 MN.m/rad, 0.0468 MN.m/rad, and 0.0327 MN.m/rad for the dexterous tests, respectively. The focus was more on joints 4, 5 and 6 since these joints are mostly affected by the applied wrench in this research and the high applied forces during a manufacturing operation. Joint 4 was the least rigid, which was least expected. The probable reason was that joint 4 was mostly responsible for holding the weight of links 3 and 4 as well as joints 5 and 6. Joint 4 experienced most of the mechanical stress due to the applied wrench on the end effector – even more so since this joint acts as a support for links 3 and 4, especially when the robot was fully extended and the "cantilever effect" maximised. Other studies that have acquired similar magnitudes and stiffness trends include Dumas *et al*. [107] and Testa [110]. However, in work performed by Dumas *et al*. [107], the stiffest joint was joint 2, and the least stiff joint was joint 6. Berntsen *et al*. [155] calculated joint 1 to be the stiffest and joint 6 to be the weakest. However, in other studies, Li *et al.* [145] estimated joint 1 to be the weakest and joint 8 to be the strongest. Based on these investigations, it is evident that stiffness characteristics are unique to every robot, as each robot possesses unique kinematical and structural properties.

The stiffness results showed an increase in the stiffness performance of the robot. The comparison of the stiffness values obtained during the non-dexterous tests and dexterous tests can be seen in Table 8-4. For the three radial distances that were tested during the dexterous tests, the results were as follows: for r_1, there was a 9%, 11% and 15% stiffness percentage improvement for joints 1, 2 and 3, respectively, and the end-effector (joint 4, 5 and 6) stiffness improved by 32%, 26% and 76%, respectively; for r_3, there was a 12%, 17% and 14% stiffness percentage improvement for joints 1, 2 and 3, respectively, and the end-effector (joint 4, 5 and 6) stiffness improved by 38%, 2% and 13%, respectively; and lastly, for r_5, there was a 19%, 4% and -9% stiffness percentage improvement for joints 1, 2 and 3, respectively, and the end-effector (joint 4, 5 and 6) stiffness improved by 115%, 165% and -18%, respectively. Overall, the stiffness the dexterous tests have substantiated that the correct robot configuration can improve the stiffness of the robot. At r_5, the decrease in performance, as previously stated, was due to three possible reasons: 1) measurement inconstancies; 2) sensitivity of accelerometers to external noise; and 3) unpredictable behaviour of the joints at the workspace boundary.

In addition, the stiffness by radial distance was analysed, and a clear relationship was observed. The stiffest positions lay within proximity to the robot's base at r_1 and r_2. As the end-effector shifted further from the base, the overall stiffness of the robot gradually decreased, with the lowest joint stiffnesses being at r_5, which explains the trend of Figure 8-11, Figure 8-12, Figure 8-13, Figure 8-14, and Table 8-4.

Apart from improving the stiffness characteristics of robots, the dexterity analysis simplified the stiffness identification technique. The Complementary stiffness matrix, K_X, was excluded from the analysis. This simplification was also applied in the studies of Dumas *et al*. [107] and Berntsen *et al.* [155]. The K_X matrix is highly non-linear and increases the computational time and expense of the analysis. This was confirmed during the non-dexterous testing procedure.

Furthermore, the results from the posture analysis showed postures 2 and 3 to be the stiffest at r = 400 mm (r_1), 800 mm (r_3), and 1,200 mm (r_5). At r_1 and z_2 = 500 mm, the postures with the highest stiffnesses were between: $\beta\{min, max\} = \{-21.13, -1.66\}$ and $\alpha\{min, max\} = \{-54.99, -10.53\}$; at r_3, between $\beta\{min, max\} = \{-24.30, -3.895\}$ and $\alpha\{min, max\} = \{-79.88, -29.94\}$; and finally, between $\beta\{min, max\} = \{-14.44, 18.98\}$ and $\alpha\{min, max\} = \{-96.54, 3.02\}$ at r_5. Although, the robot was fully extended at r_5, the possibility of stiffer configurations was proven.

The overall joint stiffnesses seen in Table 8-4 follow the same trend as the non-dexterous and dexterous results. The stiffest joint was joint 1, followed by joints 2 and 3. The weaker joints were joints 4, 5 and 6.

In conclusion, the VJM was able to evaluate the joint stiffnesses effectively. The VJM simplified the stiffness evaluation by assuming joints to be linear torsional springs and assuming infinitely stiff links. The link deflections were analysed to develop a more accurate assumption of the contribution of each link to the end-effector deflection. These tests occurred while the robot was fully extended. Based on the results, link 3 displacements contributed 0.9 % towards the end-effector displacement. Link 4, the second-longest of the links, lay nearly horizontal when the robot was fully extended, and due to its cantilever effect, it contributed 11% to the end-effector displacement. Link 2, the longest of the links, lay far from the end-effector, and contributed 9% to the end-effector displacement. These results present a limitation to the VJM identification method proposed in this research.

The stiffness identification within dexterous zones proved that posture identification does improve the kinematical and stiffness properties of a robot – the analysis allowed for optimal areas and postures within the workspace to be identified. Based on the results obtained from the non-dexterous and dexterous results, the closer the end-effector was to the robot base, the better the stiffness. Contrarily, the further away from the robot, the lower the stiffness. An optimal robot configuration drastically improves the stiffness characteristics of the robot, as demonstrated by testing in dexterous zones. The dexterity analysis also demonstrated that for dedicated tasks that are manufactured at the extremities of the robot, whether intentional or not, stiffer robot postures are still possible. Ultimately, this research established that the combination of dexterity, VJM, and a cost-effective testing regime can guarantee improved accuracy and repeatability manufacturing processes that incur high forces and vibrations – this research addressed Objectives 1, 4, 5, 6 and 7 of the study. Such manufacturing operations include, but are not limited to, precision placement tasks in the electronics industry, or machining in the automotive and aerospace industries. The value thereof cannot be understated. The implications of the research are described next.

9.7 IMPLICATIONS OF THE RESEARCH AND THE FUTURE OF MACHINING

The analysis and investigation of robotic workspace, kinematic singularity, and dexterity were proposed to identify optimal postures for precision manufacturing tasks. The stiffness identification technique was developed according to the model designed by Dumas *et al.* [107]. The method successfully identified the joint stiffnesses in conjunction with the dexterous zones developed by Mondragon [106] and Abdel Malek and Yeh [81]. Furthermore, other researchers and manufacturers can easily adopt the method who are interested in locating and identifying optimal postures with high joint stiffnesses.

This research proved that through intrinsic workspace and singularity analysis, a clearer understanding of a robot's accessibility and reachability in terms of translational and rotational movement could improve a robot's functionality. The dexterity investigation demonstrated that optimal areas/zones widely exist in every workspace envelope. The study confirmed that much research is required to shift SKMs towards enhanced manufacturing operations to keep up with modern manufacturing demands. This analysis was applied to SKMs but could be extended to PKMs upon properly examining its kinematical architecture. This section addressed Objective 2 of the study.

Fortunately, considering that state-of-the-art displacement measurement devices were not used, such as laser trackers, which cost a fortune, the errors recorded were acceptable. For researchers that have access to these high precision sensors and tools, a more accurate representation of the stiffness performance would be possible. The application of this research is most effective when the SKMs end-effector is statically positioned while the tool dynamically operates.

The use of accelerometers provided a practical, easy-to-use and cost-effective alternative to laser tracking devices. Apart from the National Instrument sensors and data acquisition devices, the torque and custom-made torque wrenches were easy and cheap to fabricate. The research into sensory devices and the testing layout development attended to Objective 5 of this study.

The possible applications of this research, as previously mentioned, include machining application that exhibits high applied forces during material handling and processing. These operations include drilling, spot welding, deburring, and spray painting of small and large components. The role and advances of the current 5 and 6-axis CNC machines continue to attract manufacturers due to their supreme heritage. The idea is not to replace this convention, but instead to assist and divide these repetitive machining tasks that require larger workspaces and greater flexibility in harder to reach areas of the workpiece.

The disadvantage would be that most manufacturers would first need to isolate their SKMs and evaluate the workspace and singularity characteristics of the robot. This would be a time-consuming process, especially if more than one type or brand of the robot is applied to a manufacturing cell or process. The time, money, and resources to train and understand each variable's importance to improve the stiffness can lead to downtime and reduce operational efficiency.

Some concluding remarks follow next.

9.8 CHAPTER SUMMARY

This chapter provided a discussion of the main findings of this research which were discussed in terms of the objectives of the study. Also discussed were the observations, application, and insights of the research. The results relating to the research question were explained, reflecting that the aim of the study, as set out in Chapter 1, was achieved. Of significance, the simulative results of the workspace and singularity analyses were examined, and the importance of these analyses in robotic stiffness modelling was established. The observations and outcomes of the stiffness results in and out of dexterous zones were also considered. The effect of dexterous posture identification on robotic stiffness was highlighted and addressed. The benefits of stiffness identification were explained, and the application of the testing methodology was proven to be easy, reliable, and cost-effective. The penultimate section noted the implication of the research and the future of machining. Any manufacturer or roboticist can easily adopt the multivariable analyses methodology towards locating and improving the stiffness of SKMs. In can be stated with confidence that the study's findings fully addressed the purpose of the study and research question developed for this research.

The final chapter revisits the aim, objectives, and research question, as outlined in Chapter 1. It also summarises the study's main findings, indicates the contribution of the research, and acknowledges the limitations that were encountered. Finally, recommendations are made for further research, followed by a brief conclusion.

10. CONCLUSION

10.1 CHAPTER INTRODUCTION

Using a literature review, this thesis explores methods to shift the robotic paradigm from general pick-and-place operations to advanced manufacturing tasks subjected to high end-effector forces and vibrations. This research was motivated by the need to reduce the high forces and vibrations experienced when the end-effector contacts the workpiece.

For ease of reference, this study's aim as indicated in Chapter 1 was to evaluate *and design a multi-point static dexterous posture identification technique that can locate and improve the stiffness of Serial Kinematic Machines and promote their functionality towards precision manufacturing tasks that involve high contact forces and vibrations*.

The objectives of this study were to:

1) Research, establish and develop a dexterous posture identification method that can localise multiple configurations at a user-defined point.
2) Research, develop, and simulate the workspace and singularities of the Fanuc M10-iA and understand their influence on the dexterity and stiffness analyses.
3) Research, establish, and identify a suitable stiffness modelling approach.
4) Develop a systematic approach to the stiffness identification algorithm such that any roboticist can universally adopt it.
5) Research, identify, and implement a cost-effective, reliable, and robust displacement sensor.
6) Research, design, construct, and implement a suitable testing ground to test the workspace, singularity, dexterity, and stiffness models.
7) Research, plan, and execute a series of tests and methods of data collection and analysis to validate the effects of the dexterous posture identification technique on the stiffness modelling of the Fanuc M10-iA.

The study was guided by the following research question: "Can a multivariable approach involving a workspace, singularity and multi-point static dexterous posture identification solution locate and improve the mechanical stiffness of Serial Kinematic Machines?"

The literature suggested that the machine industry market both globally and nationally could utilise an effective, robust, and economically attractive solution to enhance advanced manufacturing tasks using robotics. The study of manipulator workspace, singularity, and dexterity were proposed as reliable solutions to plan, locate, and improve robotic stiffness. The study was effectively carried out on an industrialised branded robot – the Fanuc M10-iA.

The outline of this chapter is as follows. After a recapping the study's aim, objectives, and research question (section 10.1), the Chapter draws all the findings of this research together (section 10.2) to summarise the key contributions it makes to the study of modern machining and robotics (section 10.3), thereby addressing the aim and objectives. The Chapter then proceeds to provide an overview of the most important research limitations (section 10.4) encountered during this study, followed by recommendations (section 10.5) to transfer the findings and insights obtained herein into concrete and practical research undertakings. In addition, possible problems that could hinder the application of this research are noted. A conclusion wraps up the study (section 10.6).

10.2 Summary of Research Findings

This section revisits some of the literature to discuss the overall findings of the study. The findings stated in Chapter 8 provided sufficient evidence supporting posture identification as a solution to improve manipulator rigidity. The study focused on an IK technique governed by Euler angles to improve the robot's stiffness. These angles materialised an invisible dexterous zone that housed the alternative postures possible at a point in space. The dexterity analysis demonstrated that improved stiffness could be achieved about specific poses that are restricted by specific angles at a point. The testing procedure was split into non-dexterous and dexterous tests to prove the superiority of the dexterity analysis studied. The non-dexterous test postulated a single posture of the end-effector (-z-direction) at multiple equidistant positions, whereas the dexterous tests applied the dexterity formulation and tested 5 configurations about similar equidistant points.

The research also demonstrated the importance of workspace and singularities. Almost all literature stresses the importance of these two concepts and focuses on them before any robotic identification study. The workspace analysis guided the tests towards a structured layout and provided the basis for which a compelling comparison between non-dexterous and dexterous tests could be made. The idea of a reachable workspace displayed the hindrance in the performance of the manipulator when fully extended. This concept then led to understanding singular positions of the robot, or points where the robot loses a DOF. The analysis displayed two singularity types that are common with serial architectures comprising of revolute joints, namely, forearm and wrist singularities. Since this research solely focused on improving robotic stiffness through a posture identification case – it was imperative to also study impossible postures or unreachable points.

The trio of analyses globally contributed to the stiffness and identification study. The idea of replacing each joint with virtual joints using the VJM drastically simplified the investigation and provided reasonable joint stiffness estimations. The study was able to identify optimal postures and characterise the workspace in terms of understanding the robot's stiffness response the further the end-effector moved away from the base. It was noted that closer proximity to the robot base had lower deflections compared to the high deflections when the robot was fully extended. A strong relationship was also noticed between the deflection values and joint stiffnesses, since these parameters are inversely related. This implied that superior joint stiffnesses were witnessed closest to the robot's base and the lower stiffnesses existed during the extension of the manipulator links. These results were witnessed during both non-dexterous and dexterous tests.

10.3 Research Contributions

This section outlines the contributions of the study. The application of the explored research contributed to three manufacturing domains. The first contribution was to improve the overall performance and increase the longevity of existing SKMs on the manufacturing floor. Applying the stiffness methodology outlined in this study can reduce the effects of chatter and other unwanted vibrations that have a destructible impact on the mechanical architecture and overall system health of SKMs.

The second contribution was to promote machine with machine. The novel CNC machine is known for its high precision and reduced workspaces compared to SKM, which lacks the former and greatly possesses the latter. For instance, the idea that the SKM performs the part handling – the preliminary and hard to reach areas to be machined first before being sent to the CNC to complete the finer details.

The third contribution was that it benefits both small and manufacturing firms with urgent requirements to improve their robots' machining ability. Particularly because most smaller enterprises are dependent on their existing and old robots and fear the expense of replacing them with more modern replacements. This research can be extended to any SKM architecture comprising of revolute joints of any size and shape.

10.4 Limitations of the Research

This section provides an overview of the most important research limitations of the study. First, access to high precision tools, such as laser trackers and other advanced high-resolution measuring sensors, was beyond the budget of this research project. The result of applying reasonably accurate replacements impacted the precision of all results recorded. The alternative sensors used, although extremely capable, were not able to provide the resolution and accuracy of results compared to similar studies that incorporated laser trackers.

Second, the Fanuc M10-iA, although extremely popular and a capable machine in a manufacturing setting, was primarily designed for general top speed pick-and-place, coating, cutting and machine tending. Ideally, the robot was not perfectly suited for the study for three reasons: (1) the robot was not designed for tasks involving high end-effector forces; (2) the robot could not be easily linked to a computer to simplify the programming of jogging to a point within the workspace and adjusting the configuration at the point. This process was controlled by the robot teach pendent, which was very manual and time-consuming; and (3) the instability of the robot joint settling time close to the workspace boundary posed problems in acquiring accurate calculated deflections and rotations.

Third, there was limited access to relevant online research sources as the University did not possess the necessary licenses. This impacted the incorporation of relevant, high-quality journal articles and conference publications in this study, which could potentially influence the findings and outcome of the study.

Fourth, there was no validation of results performed due to the global Covid-19 pandemic that erupted during the latter testing phase of the research. A telescopic linear actuator was designed and fabricated to fit the robot's end-effector. The validation was to prove superior machining finishes through various drilling applications. However, due to the nationwide lockdown in South Africa, all universities were closed, and the remainder of the study could not be completed within the research time frame.

10.5 Recommendations for Future Work

This penultimate section proposes recommendations and avenues for further research. The use of 6-D springs could be used instead of the 1-D springs that were utilised in this research. This can provide a more accurate representation of the real joint stiffness value. Further analysis of workspace and singularities could improve the number of tests. Other advanced studies have combined these analyses using advanced genetic algorithms. Validation of these results by physically performing a machining activity both in and out of dexterous zones could further prove the above findings of the research.

Due to industry's growing needs and their autonomous demands on the manufacturing floor, the IK method was initially proposed for pick-and-place operations. A flexible part handling tool that could cater to both part handling and machining could drastically advance the use of SKMs.

Further investigation is suggested for combining both manipulability and dexterity as one unified product into an optimisation solution to improve robotic stiffness since both methods are applied in posture improvements. The dynamic characteristic of the above techniques should also be investigated for dynamic operations. Finally, the extension of the above method towards improving stiffnesses in PKMs requires further exploration.

10.6 CHAPTER SUMMARY

This chapter summarised the research aim and objectives and the fulfilment thereof. The contributions of the research to improving and advancing manufacturing with SKMs were presented. The limitations of the study were also acknowledged. Finally, based on this study's insights, recommendations were made to address possible knowledge gaps in the research area.

It is envisioned that this research will contribute to the betterment of society, advance the field of robotics, and enhance human progress at the same time.

I would like to close with the following thought:

> "Robotics and other combinations will make the world pretty fantastic compared with today"
> — Bill Gates [175]

REFERENCES

[1] D. Braun, M. Howard, and S. Vijayakumar, “Optimal variable stiffness control: formulation and application to explosive movement tasks,” *Autonomous Robots*, vol. 33, no. 3, pp.237-253, 2012.

[2] R. Kalyanasundaram, S. Pandiyarajan, and S.S. Kumar “Performance evaluation and design criteria of Robot Design,” *International Journal of Research Mechanical, Mechatronics and Automobile Engineering*, vol. 5, no. 2, pp. 110-115, 2012.

[3] G. Carbone, "Stiffness analysis and experimental validation of robotic systems", *Frontiers of Mechanical Engineering*, vol. 6, no. 2, pp. 182-196, 2011.

[4] Y. Bu, W. Liao, W. Tian, J. Zhang and L. Zhang, "Stiffness analysis and optimization in robotic drilling application", *Precision Engineering*, vol. 49, pp. 388-400, 2017.

[5] U. Schneider, M. Momeni, M. Ansaloni and A. Verl, “Stiffness modeling of industrial robots for deformation compensation in machining.” In *proceedings of IEEE International Conference on Intelligent Robots and Systems*, Chicago, USA, September, 14th-18th, 2014, pp. 4464-4469.

[6] B. Olofsson, "Topics in Machining with Industrial Robot Manipulators and Optimal Motion Control,” PhD dissertation, Department of Automatic Control, Lund University, 2015.

[7] H. Qin, Y. Li, and X. Xiong, "Workpiece pose optimization for milling with flexible-joint robots to improve quasi-static performance," *Applied Sciences,* vol. 9, no. 6, p. 1044, 2019.

[8] N. Simaan, R. Yasin and L. Wang, "Medical Technologies and Challenges of Robot-Assisted Minimally Invasive Intervention and Diagnostics", *Annual Review of Control, Robotics, and Autonomous Systems*, vol. 1, no. 1, pp. 465-490, 2018.

[9] McKensey & Company, "Industrial Robotics - Insights into the sector’s future growth dynamics,” New York: McKensey & Company, 2019.

[10] I. Iglesias, M. Sebastián, and J. Ares, "Overview of the state of robotic machining: Current situation and future potential,” *Procedia Engineering,* vol. 132, pp. 911-917, 2015.

[11] Z. Pandilov and V. Dukovski, "Comparison of the characteristics between serial and parallel robots,” *Acta Technica Corviniensis-Bulletin of Engineering,* vol. 7, no. 1, p. 143-160, 2014.

[12] P. M. Bhatt, R. K. Malhan, A. V. Shembekar, Y. J. Yoon, and S. K. Gupta, "Expanding capabilities of additive manufacturing through use of robotics technologies: a survey,” *Additive Manufacturing,* vol. 31, p. 100933, 2020.

[13] L. D. Evjemo, T. Gjerstad, E. I. Grøtli, and G. Sziebig, "Trends in smart manufacturing: Role of humans and industrial robots in smart factories,” *Current Robotics Reports,* vol. 1, no. 2, pp. 35-41, 2020.

[14] R. Dillmann, "Types of robots and their integration into computer-integrated manufacturing systems.” In Rembold, U. (ed.) *Robot Technology and Applications*. New York: Marcel Dekker Inc, 2020, p.1.

[15] A. Nawaz, A. Khan, S. Noor, M. I. Mazhar, and M. Khan, "A knowledge based decision support system for tool changeover in CNCs,” in *26th International Conference on CAD/CAM, Robotics and Factories of the Future 2011*, July, 26th-28th, 2011.

[16] "International Federation of Robotics," *Global industrial robot sales doubled over the past five year*. 2018. [Online]. Available: https://ifr.org/news/global-industrial-robot-sales-doubled-over-the-past-five-years/. [Accessed on Jul. 25, 2018].

[17] "Supervised Progressively Autonomous Robot Competencies," *Robotics 2020 Multi-Annual Roadmap - For Robotics in Europe*. 2015. [Online] Available: https://www.eu-robotics.net/cms/upload/downloads/ppp-documents/Multi-Annual_Roadmap2020_ICT-24_Rev_B_full.pdf. [Accessed on Apr. 04, 2018].

[18] O. T. Laseinde and G. M. Kanakana, "Interventions to skills development in the automotive manufacturing sector of South Africa,” in Skills Development for Sustainable Manufacturing, O. T. Laseinde and G. M. Kanakana, Eds. Pretoria: Tshwane University of Technology, 2017, pp. 140-172.

[19] P. Palandrani, "*Drivers of four key segments in robotics and AI*,” 2019. [Online]. [Online]. Avaliable: https://www.globalxetfs.com/research/page/20/ [Accessed on June. 28, 2019].

[20] A. Murphy, "*Robotics outlook 2025: Demand exceeding expectations*,” Minneapolis: Loup Ventures, 2019. [Online]. Avaliable: https://loupventures.com/robotics-outlook-2025-demand-exceeding-expectations/. [Accessed on May. 02, 2019].

[21] R. Coetzee, "Localised automation and robotics solutions, using a lean and agile R&D innovation process industry,” *CSIR Science Scope*, vol. 8, no. 2, pp. 90-91, 2015.

[22] M. Xaud, "Modeling, control and electromechanical design of a modular lightweight manipulator for interaction and inspection tasks,” Masters thesis, Alberto Luiz Coimbra Institute for Graduate Studies and Research in Engineering, Rio de Janeiro, 2016.

[23] H. Celikag, N. D. Sims, and E. Ozturk, "Chatter suppression in robotic milling by control of configuration dependent dynamics,” *Procedia CIRP,* vol. 82, pp. 521-526, 2019.

[24] S. Mousavi, V. Gagnol, B. C. Bouzgarrou, and P. Ray, "Dynamic modeling and stability prediction in robotic machining,” *The International Journal of Advanced Manufacturing Technology,* vol. 88, no. 9-12, pp. 3053-3065, 2017.

[25] M. Neuhol, "*Sensors as drivers of industry 4.0: A study of Germany, Switzerland and Austria*," 2019. [Online]. Avaliable: https://assets.ey.com/content/dam/ey-sites/ey-com/de_de/topics/industrial-products/ey-study-sensors-as-drivers-of-industry-4-0.pdf?download. [Accessed on Mar. 17, 2019].

[26] A. Melanson. "*Ferrari and Ford: What do they have to do with the robotics revolution?"* 2018. [Online]. Available: https://aethon.com/ferrari-ford-bugatti-buick-robotics-revolution/. [Accessed on June. 14, 2019].

[27] "Robotic Industry Association". *Robotics industry insights*. 2018. [Online]. Available: https://www.robotics.org/Robotic-Resources. [Accessed on Nov. 25, 2020].

[28] F. Tobe. "*42 companies empowering robots and humans to work side-by-side*." 2017. [Online]. Available: https://robohub.org/42-companies-empowering-robots-and-humans-to-work-side-by-side/. [Accessed on April. 12, 2019].

[29] R. Berger, "Industry 4.0: The new industrial revolution – How Europe will succeed," 2014. [Online]. Avaliable: http://www.rolandberger.ro/media/pdf/Roland_Berger_TAB_Industry_4_0_ 20140403.pdf [Accessed on Apr. 12, 2019].

[30] M. G. Z. Peter, "Industrial Robots meet Industry 4.0," *Hadmernok,* vol. 12, no. 4, pp 230-238, 2017.

[31] European Commission, "Digital transformation of european industry and enterprises. Report and recommendations of the strategic policy forum on digital entrepreneurship," 2015. [Online]. Avaliable: https://ec.europa.eu/growth/content/digital-transformation-european-industry-and-enterprises-%E2%80%93-report-strategic-policy-forum. [Accessed on Nov. 05, 2020].

[32] M. Hermann, T. Pentek, B. Otto, "Design principles for industry 4.0 scenarios: A literature review." in *49th Hawaii International Conference on Systems Sciences*. IEEE, New York, 2016.

[33] M. A. K. Bahrin, M. F. Othman, N. N. Azli, and M. F. Talib, "Industry 4.0: A review on industrial automation and robotic," *Jurnal Teknologi,* vol. 78, no. 6-13, pp. 137-143, 2016.

[34] J. Maida, "CNC Machine Tools Market - Top Trends and Forecasts by Technavio," Technavio, BusinessWire21, 2017.

[35] "The Next Manufacturing Revolution: The Future of CNC Technology," *Institute of Technical Trades*. 2006. [Online]. Available: https://www.instituteoftechnicaltrades.com/blog/future-cnc-technology/. [Accessed on Sept. 05, 2020].

[36] R. S. Gonçalves, G. Carbone, J. C. M. Carvalho, and M. Ceccarelli, "A comparison of stiffness analysis methods for robotic systems," *International Journal of Mechanics and Control,* vol. 17, no. 2, pp. 35-58, 2016.

[37] "3D Machine Company Inc." *State-of-the-art 5-axis CNC machining*. 2013. [Online]. Available: http://3dmachineco.com/news/index-html/ [Accessed on Oct. 17, 2019].

[38] "Direct Industry." *6- axis CNC machine*. 2018. [Online]. Available: https://www.directindustry.com/industrial-manufacturer/6-axis-cnc-milling-machine-213803.html [Accessed on Sept. 14, 2019].

[39] Alibaba. *6 axis CNC robot*. 2018. [Online]. Available: https://www.alibaba.com/product-detail/Competitive-price-6-axis-cnc-robot_60681057980.html. [Accessed on Feb. 03, 2019].

[40] S. Kumar, "Industrial robotics market forecast, trends to 2020: Grand View Research," *Focus on Surfactants*, vol. 2015, no. 1, p.6, 2015.

[41] "South Africa's Manufacturing Industry." *South African Market Insights*. 2020. [Online]. Available: https://www.southafricanmi.com/south-africas-manufacturing-industry.htmls. [Accessed on Nov. 23, 2020].

[42] "EE Publishers." *The importance of manufacturing for SA's economic growth*. 2018. [Online]. Available: http://www.ee.co.za/article/the-importance-of-manufacturing-for-sas-economic-growth.html. [Accessed on May. 18, 2020].

[43] J. Maynard, "South Africa's Manufacturing Industry," *South African Market Insights,* 2020. [Online]. Avaliable: https://www.southafricanmi.com/south-africas-manufacturing-industry.html. [Accessed on Aug. 14, 2020].

[44] I. Ambe and J.B. Weiss, "South African Automotive Industry: Trends and Challenges in the Supply Chain," *Journal of Contemporary Management,* vol. 8, no. 2, pp. 337-362, 2011. (https://journals.co.za/doi/pdf/10.10520/EJC51107)

[45] "Robotics Tomorrow." *Robotics vs. CNC*. 2019. [Online]. Available: https://www.roboticstomorrow.com/article/2019/09/cnc-vs-robot/14146. [Accessed on Oct. 28, 2020].

[46] G. Williams, S. Cunningham, and D. De Beer, "Advanced manufacturing and jobs in South Africa: An examination of perceptions and trends." In *proceedings of International Conference on Manufacturing-Led Growth for Employment and Equality*. Johannesburg, pp. 3-26, May, 20th-21st, 2014.

[47] R. Rodrik, "Understanding South Africa's Economic Puzzles," *Center for International Development*, Working Paper Series 130, Harvard University, Cambridge, MA, 2006.

[48] C. Burmeister, D. Lüttgens, and F. T. Piller, "Business model innovation for industry 4.0: Why the industrial internet mandates a new perspective on innovation", vol. 1, pp. 1-31, 2015.

[49] J. P. Merlet, *Parallel robots.* Norwell, MA: Kluwer, 2006.

[50] S. Shayya, "Towards Rapid and Precise Parallel Kinematic Machines", PhD dissertation, University of Montpellier, 2015.

[51] C. Reddy, "Research and Development of a Reconfigurable Robotic End-Effector for Machining and Part Handling", Masters Dissertation, University of KwaZulu-Natal, 2020.

[52] W. Dharmalingum, "The Design and Analysis of a Novel 5 Degree of Freedom Parallel Kinematic Manipulator", Masters Dissertation, University of KwaZulu-Natal, 2020.

[53] P. Sunilkumar, R. Choudhury, R. Mohan and L Rybak. “Dynamics and Motion Control of a Three Degree of Freedom 3-PRRR Parallel Manipulator." In *European Conference on Mechanism Science*, vol. 87, no. 01, pp. 103-111, 2020.

[54] L. Lee, H. Chiang and I. Li, "Development and Control of a Pneumatic-Actuator 3-DOF Translational Parallel Manipulator with Robot Vision", *Sensors*, vol. 19, no. 6, p. 1459, 2019.

[55] S. Son, T. Kim, S. E. Sarma, and A. Slocum, "A hybrid 5-axis CNC milling machine,” *Precision Engineering,* vol. 33, no. 4, pp. 430-446, 2009.

[56] Suzuki, M., Watanabe, K., Shibukawa, T., Tooyama, T. and Hattori, K., "Development of milling machine with parallel mechanism,” *Toyota Technical Review*, vol. 47, no. 1, pp. 125–130, 1997.

[57] M. Terrier, A. Dugas, and J. Y. Hascoet, "Qualification of parallel kinematics machines in high-speed milling on free form surfaces,” *International Journal of Machine Tools and Manufacture,* vol. 44, no. 7-8, pp. 865-877, 2004.

[58] A. Pashkevich, A. Klimchik, and D. Chablat, "Enhanced stiffness modeling of manipulators with passive joints,” *Mechanism and Machine Theory,* vol. 46, no. 5, pp. 662-679, 2011.

[59] J. R. Luis Basanez, "From graphical task specification to automatic programming of robotic polishing systems,” *IEEE,* pp. 3-5, 2005.

[60] J. Franks, Z. Pan, and H. Zhang, "Robotic machining from programming to process control: A complete solution by force control,” *Industrial Robot: An International Journal*, vol. 35, no. 5, pp. 400-409*,* 2008.

[61] Z. Pan, "Robotic machining from programming to process control.” In proceedings of *World Congress of Intelligent Control and Automation*, Baltimore, pp. 553-561, June 25th-27th, 2008.

[62] L. Zhu and C. Liu, “Recent progress of chatter prediction, detection and suppression in milling", *Mechanical Systems and Signal Processing*, vol. 143, no. 1, p. 106840, 2020.

[63] Y. Tian, B. Wang, J. Liu, F. Chen, S. Yang, W. Wang, and L. Li, "Research on layout and operational pose optimization of robot grinding system based on optimal stiffness performance,” *Journal of Advanced Mechanical Design Systems and Manufacturing,* vol. 11, no. 2, p. 11, 2017.

[64] J. Tao, H. Zeng, C. Qin and C. Liu, “Chatter detection in robotic drilling operations combining multi-synchrosqueezing transform and energy entropy”, *The International Journal of Advanced Manufacturing Technology*, vol. 105, no. 7-8, pp. 2879-2890, 2019.

[65] G. Castelli, E. Ottaviano, and M. Ceccarelli, "A fairly general algorithm to evaluate workspace characteristics of serial and parallel manipulators,” *Mechanics Based Design of Structures and Machines,* vol. 36, no. 1, pp. 14-33, 2008.

[66] K. Goyal and D. Sethi, "An analytical method to find workspace of a robotic manipulator,” *Journal of Mechanical Engineering,* vol. 41, no. 1, pp. 25-30, 2010.

[67] S. Dibakar and T. Mruthyunjaya, "A computational geometry approach for determination of boundary of workspaces of planar manipulators with arbitrary topology," *Mechanism and Machine Theory,* vol. 34, no. 1, pp. 149-169, 1999.

[68] E. Ottaviano, and E. Gianni, "Manipulators workspace analysis as based on a numerical approach: Theory and applications," *Robotics: State of the Art and Future Trends*, vol. 1, no. 2, pp. 42-50, 2012.

[69] I. Zaplana and L. Basanez, "A novel closed-form solution for the inverse kinematics of redundant manipulators through workspace analysis", *Mechanism and Machine Theory*, vol. 121, no.1, pp. 829-843, 2018.

[70] A. Peidró, Ó. Reinoso, A. Gil, J. Marín and L. Payá, "An improved Monte Carlo method based on Gaussian growth to calculate the workspace of robots", *Engineering Applications of Artificial Intelligence*, vol. 64, no.1, pp. 197-207, 2017.

[71] R. Jha, D. Chablat, L. Baron, F. Rouillier and G. Moroz, "Workspace, joint space and singularities of a family of delta-like robot", *Mechanism and Machine Theory*, vol. 127, no. 1, pp. 73-95, 2018.

[72] H. Dong, Z. Du and G. Chirikjian, "Workspace density and inverse kinematics for planar serial revolute manipulators", *Mechanism and Machine Theory*, vol. 70, no.1, pp. 508-522, 2013.

[73] J. Iqbal, R. U. Islam, and H. Khan, "Modeling and analysis of a 6 DOF robotic arm manipulator," *Canadian Journal on Electrical and Electronics Engineering,* vol. 3, no. 6, pp. 300-306, 2012.

[74] Y. Cao, K. Lu, X. Li, and Y. Zang, "Accurate numerical methods for computing 2D and 3D robot workspace," *International Journal of Advanced Robotic Systems,* vol. 8, no. 6, pp. 1-13, 2011.

[75] Y. Cao, S. Qi, K. Lu, Y. Zang, and G. Yang, "An integrated method for workspace computation of robot manipulator." In *proceedings of International Joint Conference on Computational Sciences and Optimization*, vol. 1, pp. 309-312, Sanya, China, April, 24th-26th, 2009.

[76] K. Abdel-Malek and H. J. Yeh, "Analytical boundary of the workspace for general 3-DOF mechanisms," *The International Journal of Robotics Research,* vol. 16, no. 2, pp. 198-213, 1997.

[77] K. Abdel-Malek and H. J. Yeh, "Geometric representation of the swept volume using Jacobian rank-deficiency conditions," *Computer-Aided Design,* vol. 29, no. 6, pp. 457-468, 1997.

[78] K. Abdel-Malek, F. Adkins, H. J. Yeh, and E. Haug, "On the determination of boundaries to manipulator workspaces," *Robotics and Computer-Integrated Manufacturing,* vol. 13, no. 1, pp. 63-72, 1997.

[79] K. Abdel-Malek, H. J. Yeh, and M. Alkam, "Control barriers of positioning manipulators." In *proceedings of the 25th Design Automation in Mechanisms and Robotics,* Las Vegas, Nevada, 1999.

[80] K. Abdel-Malek, H. J. Yeh, and N. Khairallah, "Workspace, void, and volume determination of the general 5DOF manipulator," *Journal of Structural Mechanics,* vol. 27, no. 1, pp. 89-115, 1999.

[81] K. Abdel-Malek and H. Yeh, "Local dexterity analysis for open kinematic chains," *Mechanism and Machine Theory,* vol. 35, no. 1, pp. 131-154, 2000.

[82] A. Kumar and K. Waldron, "The workspaces of a mechanical manipulator," *Journal of Mechanical Design,* vol. 103, no. 3, pp. 665-672, 1981.

[83] G. Castelli, and E. Ottaviano, "Manipulators workspace analysis as based on a numerical approach: Theory and applications." Robotics: State of the Art and Future Trends, 2012.

[84] J. Angeles, "*Fundamentals of Robotic Mechanical Systems: Theory, Methods, and Algorithms."* Springer-Verlag, Berlin, 2002.

[85] A. Sommese, and C. Wampler, "*The Numerical solution of systems of polynomials arising in engineering and science*." World Scientific Publishing, Hackensack, 2005.

[86] E. J. Haug, C. M. Luh, F. A. Adkins, and J. Y. Wang, "Numerical algorithms for mapping boundaries of manipulator workspaces," *Journal of Mechanical Design,* vol. 118, no. 8, pp. 228-234, 1996.

[87] F. Litvin, "Application of theorem of implicit function system existence for analysis and synthesis of linkages," *Mechanism and Machine Theory,* vol. 15, no. 1, pp. 115-125, 1980.

[88] Robotic Industries Association, "Industrial Robots and Robot Systems - Safety Requirements," *Safety Standard,* vol. 62, p. 12, 1999.

[89] L. Aggarwal, R. J. Urbanic and K. Aggarwal, "A reconfigurable algorithm for identifying and validating functional workspace of industrial manipulators," In SAE World Congress 2014, Detroit, 2014.

[90] M. W. Spong, S. Hutchinson, and M. Vidyasagar, *Robot modeling and control,* vol. 3, New York: Wiley, 2006.

[91] D. Follador, and D. Jose, "Singularity robust kinematic control of a NOTES robot," In *Recent Advances in Robot Kinematics*, Dordrecht: Springer, pp. 39-49, 2011.

[92] A. A. Almarkhi and A. A. Maciejewski, "Singularity Analysis for Redundant Manipulators of Arbitrary Kinematic Structure," in *ICINCO (2)*, pp. 42-49, 2019.

[93] T. Yoshikawa, "Dynamic manipulability of robot manipulators," *Transactions of the Society of Instrument and Control Engineers,* vol. 21, no. 9, pp. 970-975, 1985.

[94] D. Oetomo and M. H. Ang Jr, "Singularity robust algorithm in serial manipulators," *Robotics and Computer-Integrated Manufacturing,* vol. 25, no. 1, pp. 122-134, 2009.

[95] P. Jha, "*Inverse kinematic analysis of robot manipulators*." Ph.D thesis National Institute of Technology Rourkela India, 2015.

[96] Z. H. Kang, C. A. Cheng, and H. P. Huang, "A singularity handling algorithm based on operational space control for six-degree-of-freedom anthropomorphic manipulators," *International Journal of Advanced Robotic Systems,* vol. 16, no. 3, pp. 17-20, 2019.

[97] F. L. Hammond, R. D. Howe and R. J. Wood, "Dexterous high-precision robotic wrist for micromanipulation." In proceedings of *16th International Conference on Advanced Robotics (ICAR)*. Montevideo, Uruguay, pp. 1-8, Nov, 25th-29th, 2013.

[98] S. Zargarbashi, W. Khan, and J. Angeles, "The Jacobian condition number as a dexterity index in 6R machining robots," *Robotics and Computer-Integrated Manufacturing,* vol. 28, no. 6, pp. 694-699, 2012.

[99] I. M. Bullock, R. R. Ma, and A. M. Dollar, "A hand-centric classification of human and robot dexterous manipulation," *IEEE Transactions on Haptics,* vol. 6, no. 2, pp. 129-144, 2013.

[100] A. Bicchi, "Hands for dexterous manipulation and robust grasping: A difficult road toward simplicity," *IEEE Transactions on Robotics and Automation,* vol. 16, no. 6, pp. 652-662, 2000.

[101] Z. Li, J. F. Canny, and S. S. Sastry, "On motion planning for dexterous manipulation." In *proceedings of IEEE International Conference on Robotics and Automation.* Scottsdale, AZ, pp. 775-780, May, 15th, 1987.

[102] A. M. Okamura, N. Smaby, and M. R. Cutkosky, "An overview of dexterous manipulation." In *proceedings of IEEE International Conference on Robotics and Automation,* pp. 255-262, April, 24th-28th, 2000.

[103] C. A. Klein and B. E. Blaho, "Dexterity measures for the design and control of kinematically redundant manipulators," *The International Journal of Robotics Research,* vol. 6, no. 2, pp. 72-83, 1987.

[104] R. Sturges, "A quantification of machine dexterity applied to an assembly task," *The International Journal of Robotics Research,* vol. 9, no. 3, pp. 49-62, 1990.

[105] Y. Guo, H. Dong, and Y. Ke, "Stiffness-oriented posture optimization in robotic machining applications," *Robotics and Computer-Integrated Manufacturing,* vol. 35, no. C, pp. 69-76, 2015.

[106] C. Mondragon, "Dynamics and Motion of a Six Degree of Freedom Robot Manipulator," PhD dissertation, University of Saskatchewan, 2012.

[107] C. Dumas, S. Caro, M. Cherif, S. Garnier, and B. Furet, "Joint stiffness identification of industrial serial robots," *Robotica,* Cambridge University Press, 2012, pp. 649-659.

[108] A. Taghvaeipour, "Online computation of the stiffness matrix in robotic structures using Finite Element Analysis," Department of Mechanical Engineering and Centre for Intelligent Machines, McGill University, Montreal, 2010.

[109] W. K. Yoon, T. Suehiro, Y. Tsumaki, and M. Uchiyama, "Stiffness analysis and design of a compact modified delta parallel mechanism," *Robotica,* Cambridge University Press, 2004, pp. 463-475.

[110] G. Testa, "Experimental stiffness identification in the joints of a lightweight robot," Master's thesis, Universitat Politècnica de Catalunya, 2017.

[111] Z. Pan, H. Zhang, Z. Zhu, and J. Wang, "Chatter analysis of robotic machining process," *Journal of Materials Processing Technology,* vol. 173, no. 3, pp. 301-309, 2006.

[112] L. Sun and L. Fang, "Research on a novel robotic arm with non-backlash driving for industrial applications." In *2017 IEEE International Conference on Cybernetics and Intelligent Systems and IEEE Conference on Robotics, Automation and Mechatronics*, 2017, pp. 70-75, November, 19th-21st, 2017.

[113] U. Schneider, M. Drust, M. Ansaloni, C. Lehmann, M. Pellicciari, F. Leali, J. W. Gunnink, and A. Verl, "Improving robotic machining accuracy through experimental error investigation and modular compensation," *The International Journal of Advanced Manufacturing Technology,* vol. 85, no. 1-4, pp. 3-15, 2016.

[114] M. Slamani, A. Nubiola, and I. A. Bonev, "Effect of servo systems on the contouring errors in industrial robots," *Transactions of the Canadian Society for Mechanical Engineering,* vol. 36, no. 1, pp. 83-96, 2012.

[115] H. Xie, W. Li, and Z. Yin, "Posture optimization based on both joint parameter error and stiffness for robotic milling." In *International Conference on Intelligent Robotics and Applications*, pp. 277-286, August, 9th-10th, 2018

[116] J. Zhang, J. Yang, Y. Yue, K. Wen, and Y. Zhou, "Optimization of comprehensive stiffness performance index for industrial robot in milling process." In *2019 IEEE 10th International Conference on Mechanical and Aerospace Engineering*, pp. 544-549, July, 22nd-25th, 2019.

[117] A. Klimchik, A. Pashkevich, and D. Chablat, "CAD-based approach for identification of elasto-static parameters of robotic manipulators," *Finite Elements in Analysis and Design,* vol. 75, no. C, pp. 19-30, 2013.

[118] A. Klimchik, "Enhanced stiffness modeling of serial and parallel manipulators for robotic-based processing of high performance materials," PhD thesis, Ecole Centrale de Nantes: Ecole des Mines de Nantes, 2011.

[119] C. Corradini, J. C. Fauroux, and S. Krut, "Evaluation of a 4-degree of freedom parallel manipulator stiffness." In *proceedings of the 11th World Congress in Mechanisms and Machine Science, Tianjin (China)*, April, 1st-4th, 2003.

[120] B. Bouzgarrou, J. Fauroux, G. Gogu, and Y. Heerah, "Rigidity analysis of T3R1 parallel robot with uncoupled kinematics." In *proceedings of the 35th International Symposium on Robotics (ISR), Paris, France*, March, 23rd-26th, 2004.

[121] B. S. El-Khasawneh and P. M. Ferreira, "Computation of stiffness and stiffness bounds for parallel link manipulators," *International Journal of Machine Tools and Manufacture,* vol. 39, no. 2, pp. 321-342, 1999.

[122] K. Nagai and Z. Liu, "A systematic approach to stiffness analysis of parallel mechanisms," In: *IEEE International Conference on Robotics and Automation(ICRA)*, Pasadena, CA, USA, pp. 1543-1548, May, 19th-23rd, 2008.

[123] J. K. Salisbury, "Active stiffness control of a manipulator in cartesian coordinates." In: *1980 19th IEEE Conference on Decision and Control including the Symposium on Adaptive Processes*, pp. 95-100, December, 10th-12th, 1980.

[124] T. Pigoski, M. Griffis, and J. Duffy, "Stiffness mappings employing different frames of reference," *Mechanism and Machine Theory,* vol. 33, no. 6, pp. 825-838, 1998.

[125] F. Majou, C. Gosselin, P. Wenger, and D. Chablat, "Parametric stiffness analysis of the Orthoglide," *Mechanism and Machine Theory,* vol. 42, no. 3, pp. 296-311, 2007.

[126] A. Pashkevich, D. Chablat, and P. Wenger, "Stiffness analysis of overconstrained parallel manipulators," *Mechanism and Machine Theory,* vol. 44, no. 5, pp. 966-982, 2009.

[127] Y. Li and Q. Xu, "Stiffness analysis for a 3-PUU parallel kinematic machine," *Mechanism and Machine Theory,* vol. 43, no. 2, pp. 186-200, 2008.

[128] J. Knapczyk and M. Ryska, "Stiffness matrix analysis of six-revolute serial manipulator," *Acta Mechanica et Automatica,* vol. 6, no. 2, pp. 62-65, 2012.

[129] O. Bohigas, "Numerical computation and avoidance of manipulator singularities," Ph.D. dissertation, Polytechnic University of Catalonia, 2013.

[130] O. Porges, R. Lampariello, J. Artigas, A. Wedler, C. Borst, and M. A. Roa, "Reachability and dexterity: Analysis and applications for space robotics." In *proceedings of the Workshop on Advanced Space Technologies for Robotics and Automation (ASTRA)*, 2015.

[131] R. G. Roberts, "The dexterity and singularities of an underactuated robot," *Journal of Robotic Systems,* vol. 18, no. 4, pp. 159-169, 2001.

[132] M. Mohammed, A. Elkady, and T. Sobh, "A New algorithm for measuring and optimizing the manipulability index," *International Journal of Advanced Robotic Systems,* vol. 6, no. 3, pp. 9-15, 2009.

[133] M. Engardt, A. Heimburger, and P. Sydhoff, "Manipulability index optimization for a planar robotic arm," Bachelor thesis, KTH Royal Institute of Technology, 2012.

[134] A. Klimchik, Y. Wu, C. Dumas, S. Caro, B. Furet, and A. Pashkevich, "Identification of geometrical and elastostatic parameters of heavy industrial robots." In: R*obotics and Automation (ICRA), 2013 IEEE International Conference*, pp. 3707-3714, May, 10, 2013.

[135] M. T. Pham, M. Gautier, and P. Poignet, "Identification of joint stiffness with bandpass filtering." In: *ICRA*, pp. 2867-2872, 2001.

[136] W. Owen, E. Croft, and B. Benhabib, "Stiffness optimization for two-armed robotic sculpting," *Industrial Robot: An International Journal,* vol. 35, no. 1, pp. 46-57, 2008.

[137] C. Dumas, S. Caro, S. Garnier, and B. Furet, "Workpiece placement optimization of six-revolute industrial serial robots for machining operations.” In *proceedings of ASME 2012 11th Biennial Conference on Engineering Systems Design and Analysis*, pp. 419-428, July, 2nd-4th, 2012.

[138] D. Spensieri, J. S. Carlson, R. Bohlin, J. Kressin, and J. Shi, "Optimal robot placement for tasks execution.” *Procedia CIRP,* vol. 44, no. 1, pp. 395-400, 2016.

[139] R. K. Malhan, A. M. Kabir, B. Shah, and S. K. Gupta, "Identifying feasible workpiece placement with respect to redundant manipulator for complex manufacturing tasks.” In *proceedings of 2019 International Conference on Robotics and Automation (ICRA)*, pp. 5585-5591, May, 20th-24th, 2019.

[140] A. M. Lopes and E. S. Pires, "Optimization of the workpiece location in a machining robotic cell.” *International Journal of Advanced Robotic Systems,* vol. 8, no. 6, pp. 73-80, 2011.

[141] R. Pérez, S. C. Gutiérrez, and R. Zotovic, "A study on robot arm machining: advance and future challenges.” *Annals of DAAAM & Proceedings,* vol. 29, no. 1, pp. 5-10, 2018.

[142] S. Abdolshah, D. Zanotto, G. Rosati, and S. K. Agrawal, "Optimizing stiffness and dexterity of planar adaptive cable-driven parallel robots,” *Journal of Mechanisms and Robotics,* vol. 9, no. 3, pp. 4-15, 2017.

[143] M. Arsenault and R. Boudreau, "Synthesis of planar parallel mechanisms while considering workspace, dexterity, stiffness and singularity avoidance.” In *proceedings of ASME Journal of Mechanical Design*, vol. 128, no. 1, pp. 69–78, 2016.

[144] M. Z. Huang, "Design of a planar parallel robot for optimal workspace and dexterity,” *International Journal of Advanced Robotic Systems,* vol. 8, no. 4, p. 49-55, 2011.

[145] G. Li, F. Zhang, Y. Fu, and S. Wang, "Joint stiffness identification and deformation compensation of serial robots based on dual quaternion algebra,” *Applied Sciences,* vol. 9, no. 1, pp. 65-75, 2019.

[146] G. Xiong, Y. Ding, and L. Zhu, "Stiffness-based pose optimization of an industrial robot for five-axis milling,” *Robotics and Computer-Integrated Manufacturing,* vol. 55, pp. 19-28, 2019.

[147] X. Zhang, B. Chen, J. Qi, and Z. Niu, "Robot Workspace Optimization and Deformation Compensation in Grinding,” In: *International Conference on Intelligent Robotics and Applications*, pp. 97-109, July, 23rd-25th, 2019.

[148] C. Chen, F. Peng, R. Yan, Y. Li, D. Wei, Z. Fan, X. Tang, Z. Zhu, "Stiffness performance index based posture and feed orientation optimization in robotic milling process,” *Robotics and Computer-Integrated Manufacturing,* vol. 55, no. 1, pp. 29-40, 2019.

[149] A. Klimchik, S. Caro, B. Furet, and A. Pashkevich, "Complete stiffness model for a serial robot,” in *Informatics in Control, Automation and Robotics (ICINCO), 2014 11th International Conference on*, pp. 192-202, 2014

[150] H. Dong, Z. Du, and G. S. Chirikjian, "Workspace density and inverse kinematics for planar serial revolute manipulators," *Mechanism and Machine Theory,* vol. 70, pp. 508-522, 2013.

[151] M. Esquerrà Corominas, "Workspace and singularity determination of a 7-DoF wrist-partitioned serial manipulator towards graffiti painting," Bachelor's thesis, Polytechnic University of Catalonia, 2020.

[152] O. Bohigas, M. Manubens, and L. Ros, "A complete method for workspace boundary determination on general structure manipulators," *IEEE Transactions on Robotics,* vol. 28, no. 5, pp. 993-1006, 2012.

[153] K. Goyal and R. L. Virdi, "Finding Reachable Workspace of a Robotic Manipulator by Edge Detection Algorithm," *International Journal of Advanced Mechatronics and Robotics,* vol. 3, pp. 43-51, 2011.

[154] P. Donelan, "Kinematic singularities of robot manipulators," In *Advances in Robot Manipulators*, Ernest Hall (Ed.), 2010.

[155] K. E. Berntsen, A. B. Bertheussen, and I. Tyapin, "Combined Stiffness Identification of 6-DoF Industrial Robot". In *2018 18th International Conference on Control, Automation and Systems (ICCAS)*, pp. 1681-1686, October 17th-20th, 2018.

[156] "FANUC Robot M-10iA," *Small Payload Handling Intelligent Robot*, 2015. [Online]. Available: https://www.fanuc.co.jp/en/product/catalog/pdf/robot/RM-10iAN(E)-02.pdf. [Accessed on Dec. 02, 2019].

[157] S. M. S. Rocha, J. F. S. Feiteira, P. S. N. Mendes, U. P. B. Da Silva, and R. F. Pereira. "Method to Measure Displacement and Velocity from Acceleration Signals." *International Journal of Engineering Research and Application,* vol. 6, no. 6, pp. 52-59, 2016.

[158] T. M. Do and T. C. Le, "Performance analysis of FFT filter to measure displacement signal in road roughness profiler," *International Journal of Computer and Electrical Engineering,* vol. 5, no. 4, p. 356, 2013.

[159] M. Arraigada and M. Partl, "Calculation of displacements of measured accelerations, analysis of two accelerometers and application in road engineering," in *Conference paper STRC*, 2006.

[160] H. Han, J. Wang, X. Meng and H. Liu, "Analysis of the dynamic response of a long span bridge using GPS/accelerometer/anemometer under typhoon loading", *Engineering Structures*, vol. 122, pp. 238-250, 2016.

[161] M. Alam and J. Rohac, "Adaptive data filtering of inertial sensors with variable bandwidth," *Sensors,* vol. 15, no. 2, pp. 3282-3298, 2015.

[162] N. Liu and T. Schumacher, "Improved Denoising of structural vibration data employing bilateral filtering," *Sensors,* vol. 20, no. 5, p. 1423, 2020.

[163] J. G. Ribeiro, J. T. De Castro, and J. L. Freire, "Using the FFT-DDI method to measure displacements with piezoelectric, resistive and ICP accelerometers." In *proceedings of 9th International Modal Analysis Conference*, vol. 3727, Orlando, Florida, 2003, pp. 538-542.

[164] C. Pan, R. Zhang, H. Luo, and H. Shen, "Baseline correction of vibration acceleration signals with inconsistent initial velocity and displacement." *Advances in Mechanical Engineering,* vol. 8, no. 10, p. 168-181, 2016.

[165] R. Wu, R. Qiongqiong, H. Lin, and L. Ying, "Piecewise polynomial fitting with trend item removal and its application in a cab vibration test". *Journal of Sensors*, vol. 2018, pp. 1–8, 2018.

[166] W. Niu, F. Li-qing, Z. Qi, and D. Guo, "Small displacement measuring system based on mems accelerometer," *Mathematical Problems in Engineering,* vol. 2019, pp. 54-70, 2019.

[167] M. Serridge and T. R. Licht, "Piezoelectric accelerometers and vibration preamplifiers," Theory & Application Handbook, Bruel & Kjaer Instruments, Denmark, November 1987.

[168] F. Cheraghpour, M. Vaezi, H. E. Shoori Jazeh and S. A. A. Moosavian, "Dynamic modeling and kinematic simulation of Stäubli© TX40 robot using MATLAB/ADAMS co-simulation." In *proceedings of IEEE International Conference on Mechatronics*, Istanbul, Turkey, April, 13th-15th, 2011, pp. 386-391.

[169] M. Galli, R. Barber, S. Garrido and L. Moreno, "Path planning using Matlab-ROS integration applied to mobile robots." In *proceedings of IEEE International Conference on Autonomous Robot Systems and Competitions (ICARSC)*, Coimbra, Portugal, April, 26th-28th, 2017, pp. 98-103.

[170] M. Whitty, "Robotics, Vision and Control. Fundamental Algorithms in MATLAB", *Industrial Robot: An International Journal*, vol. 39, no. 6, 2012.

[171] K. J. Waldron and J. Schmiedeler, "*Kinematics*." In: Siciliano B., Khatib O. (eds) Springer Handbook of Robotics. Springer Handbooks. Springer, Cham, 2016, pp. 11-36.

[172] A. G. Gudla, "*A methodology to determine the functional workspace of a 6R robot using forward kinematics and geometrical methods*." Windsor: University of Windsor, 2012.

[173] H. Bruyninckx, "Serial robots," *The Robotics Webook,* vol. 117, pp. 13-20, 2005.

[174] C. Dumas, S. Caro, S. Garnier, and B. Furet, "Workpiece placement optimization of six-revolute industrial serial robots for machining operations." In *proceedings of ASME 2012 11th Biennial Conference on Engineering Systems Design and Analysis*, pp. 419-428, July, 2nd-4th, 2012.

[175] "AZ Quotes" *Robotics quotes*. 2020. [Online]. Available: https://www.azquotes.com/policy.html [Accessed on Nov. 20, 2020].

APPENDICES

APPENDIX A

A.1 ROBOT SPECIFICATIONS

The technical specifications of the Fanuc M10-iA robot are listed in Table A-1. The dimensioning and isometric views of the robot are also shown in Figure A-1.

Table A-1: Technical Specifications of Fanuc M-10iA

Items		**M-10iA**
Axes		6
Payload (kg)		10
Payload (kg) on J3 casting		12
Reach (mm)		1,420
Repeatability (mm)		± 0.08
Interference radius (mm)		262
Motion range (degrees)	J1	340/360
	J2	250
	J3	290 (445)
	J4	380
	J5	380
	J6	720
Motion speed (degrees/s)	J1	210
	J2	190
	J3	210
	J4	400
	J5	400
	J6	600
Wrist moments N.m / (kgf.m)	J4	22/ (2.2)
	J5	22 /(2.2)
	J6	9.8 /(1.0)
Wrist load inertia ($kg.m^2$)	J4	0.63
	J5	0.63
	J6	0.15
Mechanical brakes		All axes
Mechanical weight (kg)		130

Items	**M-10iA**
Mounting method	Floor, ceiling, angle or wall
Installation environment	
Temperature (˚C)	0 to 45
Humidity	Normally: 75% or less Short term (within a month): 95% or less. No condensation
Vibration (m/s^2)	4.9 or less (0.5 G or less)
IP rating(s)	IP 67 forearm and wrist/ IP 54 lower body

A.2. Robot Isometric Views and Dimensions

This section presents the isometric views and dimensions of the Fanuc M10-iA robot

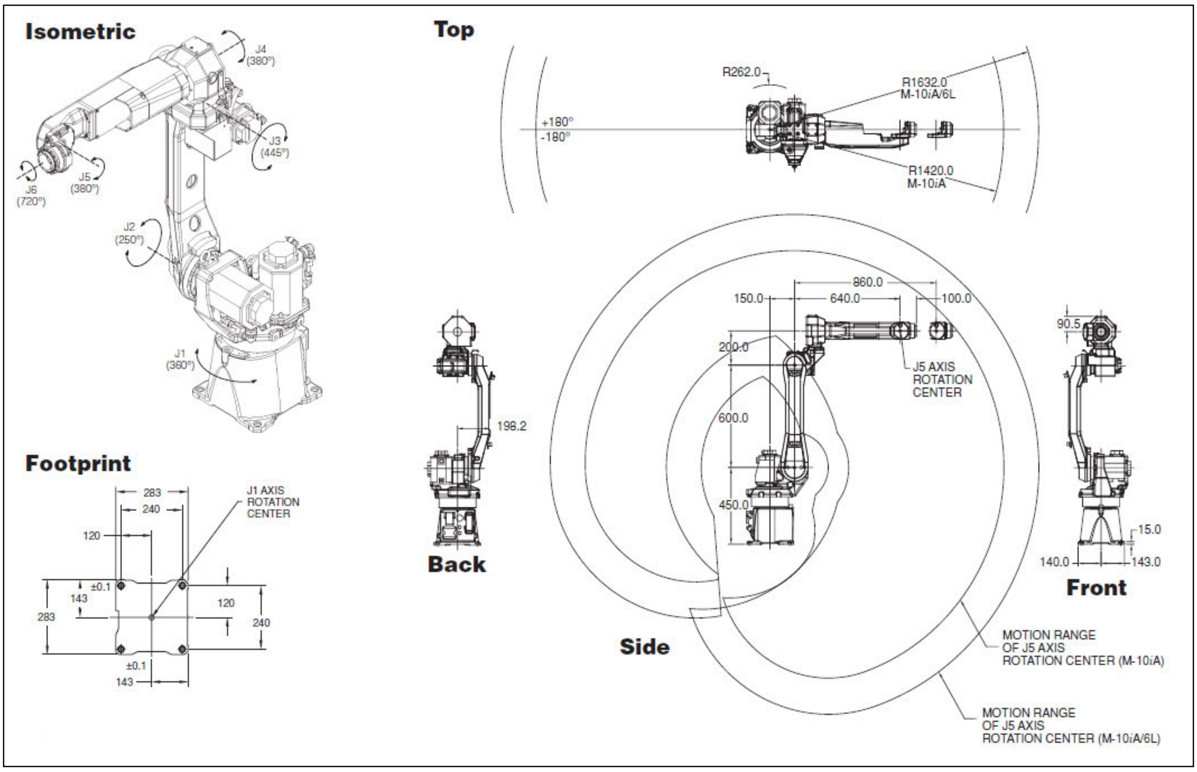

Figure A.2-1:Isometric View and Dimensioning of Fanuc M10-iA [156]

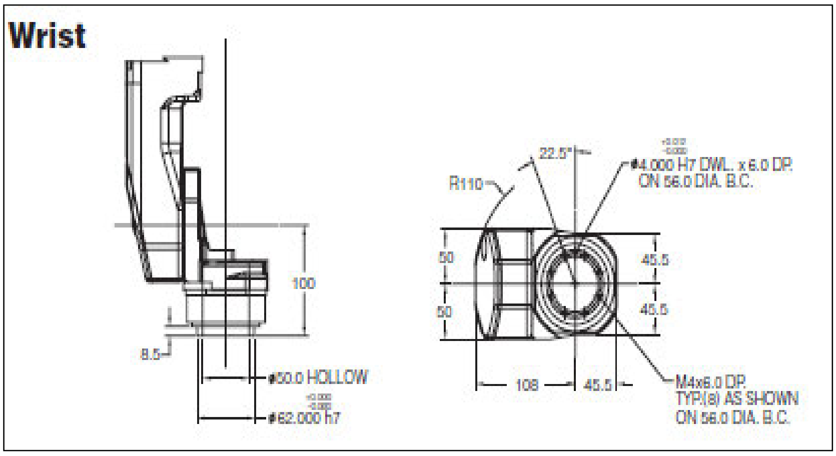

Figure A.2-2: Fanuc M-10iA End effector with Dimensions [156]

APPENDIX B – FANUC M10-IA KINEMATICS

B.1 FORWARD KINEMATICS

The Fanuc M-10iA robot is a 6-DOF serial manipulator (n = 6) and therefore to determine the position of the end effector with respect to the robot base frame, equation [B.1] becomes:

$$^{0}T_6 = {}^{0}T_1 \times {}^{1}T_2 \times {}^{2}T_3 \times {}^{3}T_4 \times {}^{4}A_5 \times {}^{5}T_6 = \begin{bmatrix} ^{0}R_6 & ^{0}\mathrm{p}_6 \\ 0 & 1 \end{bmatrix} \quad [B.1]$$

The transformation matrices are developed substituting the D-H parameters from Table 4-1, as follows: for $(\mathbf{i} = \mathbf{1})$ and $(\boldsymbol{\theta_1} = \boldsymbol{\pi} + \mathbf{q_1})$:

$$^{0}T_1 = \begin{bmatrix} \cos(\pi + q_1) & -\cos(\frac{\pi}{2})sin(\pi + q_1) & \cos(\frac{\pi}{2})sin(\pi + q_1) & -150\cos(\pi + q_1) \\ sin\,(\pi + q_1) & cos(\frac{\pi}{2})cos(\pi + q_1) & -sin(\frac{\pi}{2})cos(\pi + q_1) & -150sin(\pi + q_1) \\ 0 & sin(\frac{\pi}{2}) & cos(\frac{\pi}{2}) & 450 \\ 0 & 0 & 0 & 1 \end{bmatrix}$$

$$^{0}T_1 = \begin{bmatrix} -\cos(q_1) & 0 & 0 & (150)\cos(q_1) \\ -sin\,(q_1) & 0 & cos(q_1) & (150)sin(q_1) \\ 0 & 1 & 0 & 450 \\ 0 & 0 & 0 & 1 \end{bmatrix}$$

$$^{0}R_1 = \begin{bmatrix} -\cos(q_1) & 0 & 0 \\ -sin\,(q_1) & 0 & -cos(q_1) \\ 0 & 1 & 0 \end{bmatrix}$$

$$^{0}\mathrm{p}_1 = \begin{bmatrix} -0.150\cos(q_1) \\ -0.150sin(q_1) \\ 0.450 \end{bmatrix}$$

for $(\mathbf{i} = \mathbf{2})$ and $(\boldsymbol{\theta_2} = \frac{\boldsymbol{\pi}}{\mathbf{2}} + \mathbf{q_2})$:

$$^{1}T_2 = \begin{bmatrix} \cos(\frac{\pi}{2} + q_2) & -\cos(0)sin(\frac{\pi}{2} + q_2) & \cos(0)sin(\frac{\pi}{2} + q_2) & 600\cos(\frac{\pi}{2} + q_2) \\ sin\,(\frac{\pi}{2} + q_2) & cos(0)cos(\frac{\pi}{2} + q_2) & -sin(0)cos(\frac{\pi}{2} + q_2) & 600sin(\frac{\pi}{2} + q_2) \\ 0 & sin(0) & cos(0) & 0 \\ 0 & 0 & 0 & 1 \end{bmatrix}$$

$$^{1}T_2 = \begin{bmatrix} -\sin(q_2) & -cos(q_2) & cos(q_2) & -(600)\sin(q_2) \\ cos\,(q_2) & -sin(q_2) & 0 & (600)cos(q_2) \\ 0 & 0 & 1 & 0 \\ 0 & 0 & 0 & 1 \end{bmatrix}$$

$$^{1}R_2 = \begin{bmatrix} -\sin(q_2) & -cos(q_2) & sin(q_2) \\ cos(q_2) & -sin(q_2) & -cos(q_2) \\ 0 & 0 & 0 \end{bmatrix}$$

$$^{1}p_2 = \begin{bmatrix} (600)\cos(q_2) \\ (600)sin(q_2) \\ 0 \end{bmatrix}$$

for ($\mathbf{i = 3}$) and ($\boldsymbol{\theta_3 = \pi + q_3}$):

$$^{2}T_3 = \begin{bmatrix} \cos(\pi + q_3) & -\cos(\frac{\pi}{2})sin(\pi + q_3) & \cos(\frac{\pi}{2})sin(\pi + q_3) & -(200)\cos(\pi + q_3) \\ sin\ (\pi + q_3) & cos(\frac{\pi}{2})cos(\pi + q_3) & -sin(\frac{\pi}{2})cos(\pi + q_3) & -(200)sin(\pi + q_3) \\ 0 & sin(\frac{\pi}{2}) & cos(\frac{\pi}{2}) & 0 \\ 0 & 0 & 0 & 1 \end{bmatrix}$$

$$^{2}T_3 = \begin{bmatrix} -\cos(q_3) & 0 & 0 & (200)\cos(q_3) \\ -sin\ (q_3) & 0 & cos(q_3) & (200)sin(q_3) \\ 0 & 1 & 0 & 0 \\ 0 & 0 & 0 & 1 \end{bmatrix}$$

$$^{2}R_3 = \begin{bmatrix} -\cos(q_3) & 0 & 0 \\ -sin\ (q_3) & 0 & cos(q_3) \\ 0 & 1 & 0 \end{bmatrix}$$

$$^{2}p_3 = \begin{bmatrix} (200)\cos(q_3) \\ (200)sin(q_3) \\ 0 \end{bmatrix}$$

for ($\mathbf{i = 4}$) and ($\boldsymbol{\theta_4 = \pi + q_4}$):

$$^{3}T_4 = \begin{bmatrix} \cos(\pi + q_4) & -\cos(\frac{\pi}{2})sin(\pi + q_4) & \cos(\frac{\pi}{2})sin(\pi + q_4) & (0)\cos(\pi + q_4) \\ sin\ (\pi + q_4) & cos(\frac{\pi}{2})cos(\pi + q_4) & -sin(\frac{\pi}{2})cos(\pi + q_4) & (0)sin(\pi + q_4) \\ 0 & sin(\frac{\pi}{2}) & cos(\frac{\pi}{2}) & 640 \\ 0 & 0 & 0 & 1 \end{bmatrix}$$

$$^{3}T_4 = \begin{bmatrix} -\cos(q_4) & 0 & 0 & 0 \\ -sin\ (q_4) & 0 & cos(q_4) & 0 \\ 0 & 1 & 0 & 640 \\ 0 & 0 & 0 & 1 \end{bmatrix}$$

$$^{3}R_4 = \begin{bmatrix} -\cos(\theta_4) & 0 & 0 \\ -sin\ (\theta_4) & 0 & cos(\theta_4) \\ 0 & 1 & 0 \end{bmatrix}$$

$$ {}^{3}p_4 = \begin{bmatrix} 0 \\ 0 \\ 640 \end{bmatrix} $$

for ($\mathbf{i} = \mathbf{5}$) and ($\boldsymbol{\theta_5} = \boldsymbol{\pi} + \mathbf{q_5}$):

$$ {}^{4}T_5 = \begin{bmatrix} \cos(\pi + q_5) & -\cos(\frac{\pi}{2})sin(\pi + q_5) & \cos(\frac{\pi}{2})sin(\pi + q_5) & (0)\cos(\pi + q_5) \\ sin\ (\pi + q_5) & cos(\frac{\pi}{2})cos(\pi + q_5) & -sin(\frac{\pi}{2})cos(\pi + q_5) & (0)sin(\pi + q_5) \\ 0 & sin(\frac{\pi}{2}) & cos(\frac{\pi}{2}) & 0 \\ 0 & 0 & 0 & 1 \end{bmatrix} $$

$$ {}^{4}T_5 = \begin{bmatrix} -\cos(\theta_5) & 0 & 0 & 0 \\ -sin\ (\theta_5) & 0 & cos(\theta_5) & 0 \\ 0 & 1 & 0 & 0 \\ 0 & 0 & 0 & 1 \end{bmatrix} $$

$$ {}^{4}T_5 = \begin{bmatrix} -\cos(\theta_5) & 0 & 0 \\ -sin\ (\theta_5) & 0 & cos(\theta_5) \\ 0 & 1 & 0 \end{bmatrix} $$

$$ {}^{4}T_5 = \begin{bmatrix} 0 \\ 0 \\ 0 \end{bmatrix} $$

for ($\mathbf{i} = \mathbf{6}$) and ($\boldsymbol{\theta_6} = \mathbf{q_6}$):

$$ {}^{5}T_6 = \begin{bmatrix} \cos(q_6) & -\cos(0)sin(q_6) & \cos(0)sin(q_6) & 0\cos(q_6) \\ sin\ (q_6) & cos(0)cos(q_6) & -sin(0)cos(q_6) & 0sin(q_6) \\ 0 & sin(0) & cos(0) & 0 \\ 0 & 0 & 0 & 1 \end{bmatrix} $$

$$ {}^{5}T_6 = \begin{bmatrix} \cos(q_6) & -sin(q_6) & sin(q_6) & 0 \\ sin\ (q_6) & cos(q_6) & 0 & 0 \\ 0 & 0 & 1 & 0 \\ 0 & 0 & 0 & 1 \end{bmatrix} $$

$$ {}^{5}T_6 = \begin{bmatrix} \cos(q_6) & -sin(q_6) & sin\ (q_6) \\ sin\ (q_6) & cos(q_6) & 0 \\ 0 & 0 & 1 \end{bmatrix} $$

$$ {}^{5}T_6 = \begin{bmatrix} 0 \\ 0 \\ 0 \end{bmatrix} $$

To confirm the accuracy of the above Homogenous-Transformation Matrices and assuming that the robot is in its initial configuration (i.e., zeroed joints) (shown in Figure B1) such that:

$$q_1 = q_2 = q_3 = q_4 = q_5 = q_6 = 0 \qquad \text{[B-2]}$$

The Homogenous-Transformation Matrices for the position of the end effector with respect to the robot base becomes:

$$0T_6 = \begin{bmatrix} 0 & 0 & 1 & 790 \\ 0 & 1 & 0 & 0 \\ -1 & 0 & 0 & 1250 \\ 0 & 0 & 0 & 1 \end{bmatrix} \qquad \text{[B.3]}$$

Equation [B.3] can be confirmed graphically by Figure 4-2:

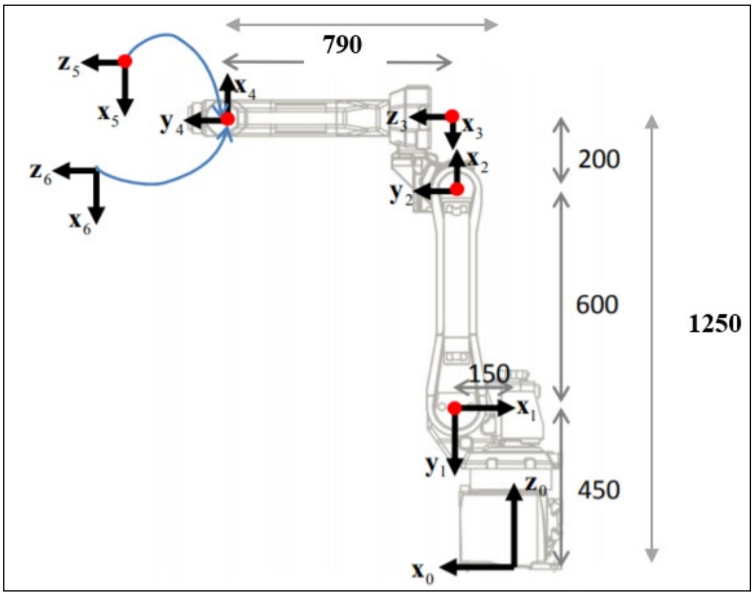

Figure B-1: End effector position with Respect to Robot Base

Appendix C – Jacobian Matrix Results

C.1 Jacobian Matrix Elements

The Jacobian matrix was evaluated in MATLAB using Peter Corkes Toolbox [170].

$J_{11} = -10\sin(\theta_1)(64\cos(\theta_2 + \theta_3) + 20\sin(\theta_2 + \theta_3) + 60\sin(\theta_2) + 15)$

$J_{12} = 40\cos(\theta_1)(5\cos(\theta_2 + \theta_3) - 16\sin(\theta_2 + \theta_3) + 15\cos(\theta_2))$

$J_{13} = 40\cos(\theta_1)(5\cos(\theta_2 + \theta_3) - 16\sin(\theta_2 + \theta_3))$

$J_{14} = 0$

$J_{15} = 0$

$J_{16} = 0$

$J_{21} = 10\cos(\theta_1)(64\cos(\theta_2 + \theta_3) + 20\sin(\theta_2 + \theta_3) + 60\sin(\theta_2) + 15)$

$J_{22} = 40\sin(\theta_1)(5\cos(\theta_2 + \theta_3) - 16\sin(\theta_2 + \theta_3) + 15\cos(\theta_2))$

$J_{23} = 40\sin(\theta_1)(5\cos(\theta_2 + \theta_3) - 16\sin(\theta_2 + \theta_3))$

$J_{24} = 0$

$J_{25} = 0$

$J_{26} = 0$

$J_{31} = 0$

$J_{32} = -600\sin(\theta_2) - (40)(281^{\frac{1}{2}})\cos(\theta_2 + \theta_3 - \operatorname{atan}(\frac{5}{16}))$

$J_{33} = (640\cos(\theta_6)\sin(\theta_4) - \sin(\theta_6)(200\sin(\theta_5) - 640\cos(\theta_4)\cos(\theta_5)))(\sin(\theta_6)(\sin(\theta_2 + \theta_3)\sin(\theta_5) - \cos(\theta_2 + \theta_3)\cos(\theta_4)\cos(\theta_5)) - \cos(\theta_2 + \theta_3)\cos(\theta_6)\sin(\theta_4)) - (640\sin(\theta_4)\sin(\theta_6) + \cos(\theta_6)(200\sin(\theta_5) - 640\cos(\theta_4)\cos(\theta_5)))(\cos(\theta_6)(\sin(\theta_2 + \theta_3)\sin(\theta_5) - \cos(\theta_2 + \theta_3)\cos(\theta_4)\cos(\theta_5)) + \cos(\theta_2 + \theta_3)\sin(\theta_4)\sin(\theta_6)) - (\sin(\theta_2 + \theta_3)\cos(\theta_5) + \cos(\theta_2 + \theta_3)\cos(\theta_4)\sin(\theta_5))(200 * \cos(\theta_5) + 640\cos(\theta_4)\sin(\theta_5))$

$J_{34} = 0$

$J_{35} = 0$

$J_{36} = 0$

$J_{41} = 0$

$J_{42} = -\sin(\theta_1)$

$J_{43} = -\sin(\theta_1)$

$J_{44} = \cos(\theta_2 + \theta_3)\cos(\theta_1),$

$J_{45} = \cos(\theta_1)\cos(\theta_2)\sin(\theta_3) * \sin(\theta_4) - \cos(\theta_4)\sin(\theta_1) + \cos(\theta_1)\cos(\theta_3) * \sin(\theta_2)\sin(\theta_4)$

$J_{46} = -\sin(\theta_5)(\sin(\theta_1) * \sin(\theta_4) + \cos(\theta_4) * (\cos(\theta_1)\cos(\theta_2)\sin(\theta_3) + \cos(\theta_1)\cos(\theta_3)\sin(\theta_2))) - \cos(\theta_5)(\cos(\theta_1)\sin(\theta_2)\sin(\theta_3) - \cos(\theta_1)\cos(\theta_2)\cos(\theta_3))$

$J_{51} = 0$

$J_{52} = \cos(\theta_1)$

$J_{53} = \cos(\theta_1),$

$J_{54} = \cos(\theta_2 + \theta_3)\sin(\theta_1)$

$J_{55} = \cos(\theta_1)\cos(\theta_4) + \cos(\theta_2)\sin(\theta_1)\sin(\theta_3)\sin(\theta_4) + \cos(\theta_3)\sin(\theta_1)\sin(\theta_2)\sin(\theta_4)$

$J_{56} = \sin(\theta_5)(\cos(\theta_1)\sin(\theta_4) - \cos(\theta_4)(\cos(\theta_2)\sin(\theta_1)\sin(\theta_3) + \cos(\theta_3)\sin(\theta_1)\sin(\theta_2))) - \cos(\theta_5) * (\sin(\theta_1)\sin(\theta_2) * \sin(\theta_3) - \cos(\theta_2)\cos(\theta_3)\sin(\theta_1))$

$J_{61} = (\sin(\theta_2 + \theta_3) * \cos(\theta_5) + \cos(\theta_2 + \theta_3)\cos(\theta_4)\sin(\theta_5))^2 + (\cos(\theta_6)(\sin(\theta_2 + \theta_3)\sin(\theta_5) - \cos(\theta_2 + \theta_3)\cos(\theta_4)\cos(\theta_5)) + \cos(\theta_2 + \theta_3)\sin(\theta_4)\sin(\theta_6))\hat{}2 + (\sin(\theta_6)(\sin(\theta_2 + \theta_3)\sin(\theta_5) - \cos(\theta_2 + \theta_3)\cos(\theta_4)\cos(\theta_5 5)) - \cos(\theta_2 + \theta_3)\cos(\theta_6)\sin(\theta_4))^2$

$J_{62} = 0$

$J_{63} = 0$

$J_{64} = -\sin(\theta_2 + \theta_3)$

$J_{65} = \cos(\theta_2 + \theta_3)\sin(\theta_4)$

$J_{66} = -\sin(\theta_2 + \theta_3)\cos(\theta_5) - \cos(\theta_2 + \theta_3)\cos(\theta_4)\sin(\theta_5)$

Appendix D – Joint Stiffness Trends

Appendix D presents the joint stiffness trends for r_1 and r_5 for the non-dexterous and dexterous tests. The joint stiffness trend for r_3 is presented in Chapter 8.

D.1. Non-Dexterous Tests

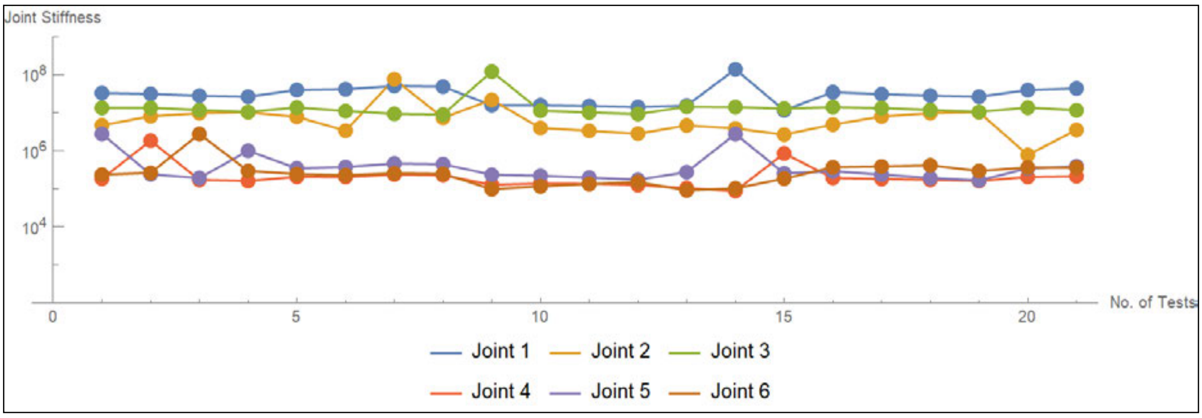

Figure D.1-1: Non-Dexterous: Estimated Joint Stiffness Values [MN m/rad] – r_1

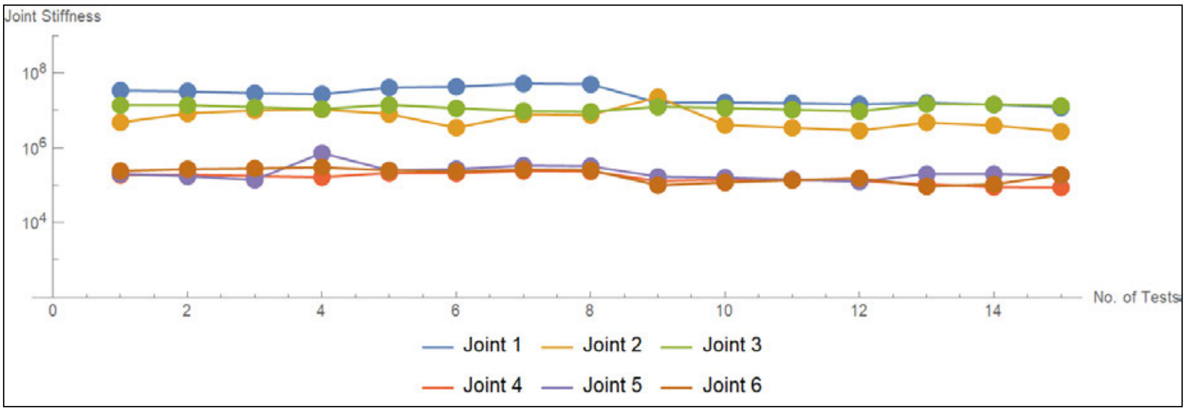

Figure D.1-2: Dexterous: Estimated Joint Stiffness Values [MN m/rad] – r_1

D.2. Dexterous Tests

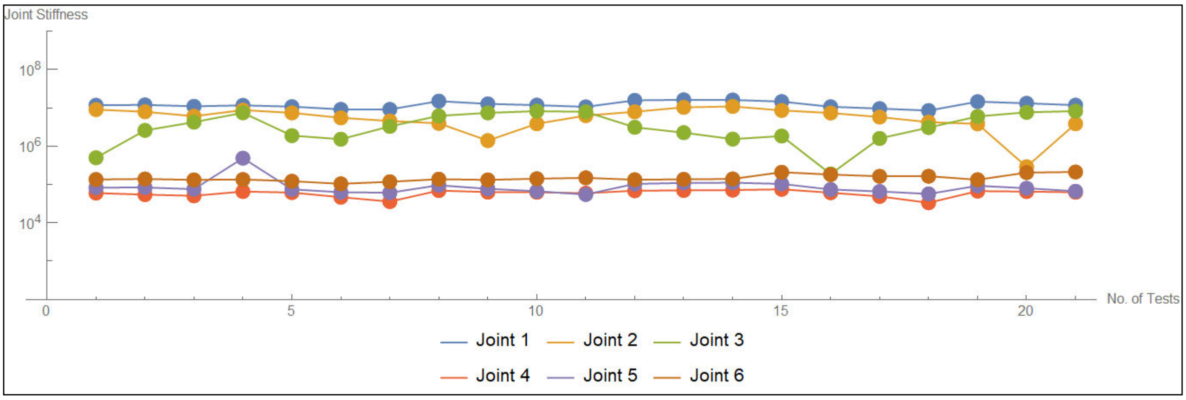

Figure D-4: Non-Dexterous: Estimated Joint Stiffness Values [MN.m/rad] – r_5

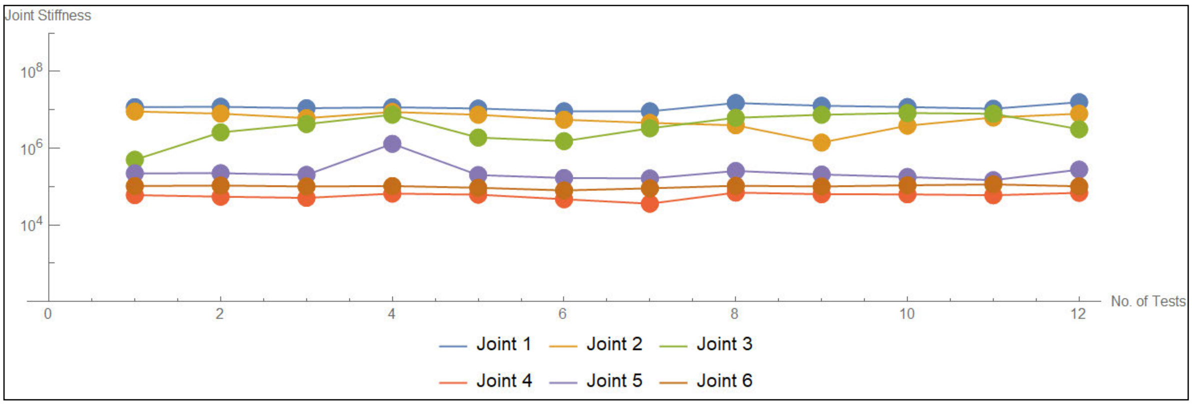

Figure D-5: Dexterous: Estimated Joint Stiffness Values [MN m/rad] – r_5